Master Thesis

Research on Long-term Operation and Analysis Method of Positron Timing Counter in MEG II Experiment

(MEG II実験陽電子タイミングカウンターの長期運用・解析手法に関する研究)

Kosuke Yanai

Supervisor: Prof. Wataru Ootani

Department of Physics, School of Science
The University of Tokyo

THE UNIVERSITY OF TOKYO

Abstract

The MEG II experiment plans to search for new physics beyond the Standard Model via the charged-lepton-flavor-violating $\mu \to e\gamma$ decay. In order to achieve the target sensitivity of 6×10^{-14}, all the detectors have been renewed from the preceding MEG experiment to enhance each resolution by a factor of two. All the detector constructions have now been completed, and the physics data will be taken as soon as the full electronics are available.

The pixelated Timing Counter (pTC) in the MEG II experiment reduces the dominant accidental background by detecting the emitted positrons with a high time resolution. It consists of 512 pixels, each of which is composed of a 120 mm × (40 / 50) mm × 5 mm plastic scintillator with six series-connected SiPMs at both ends. Each pixel has a time resolution of 80–100 ps, and an overall resolution below 40 ps is expected to be achieved by a multiple-pixel-hit scheme. This thesis focuses on the long-term stable operation of the pTC and its capability to achieve the expected performance in the long run.

The effect of radiation damage to SiPMs on the pTC performance was studied in detail. It was newly found that intrinsic time offsets exist between the series-connected SiPMs, which can cause time fluctuations depending on the hit position of the particle, and consequently worsen the pTC resolution from the originally-expected value. It was further found that this position dependence can be enhanced by a gradient radiation damage to series-connected SiPMs as in the case of the MEG II pTC, which results in a further $\sim 13\,\%$ degradation of the pTC resolution.

In order to compensate this effect, two attempts were made. One was to develop optimization schemes of the bias voltage to SiPMs and the constant fraction parameter in the waveform analysis. The optimal values of these parameters shift with the increasing dark noise level caused by radiation damage to SiPMs, and therefore, the maximum pTC performance can be brought out by optimizing these parameters at each time point. The latter optimization was verified to improve the pTC resolution by $\sim 3\,\%$.

The other attempt was to improve the pTC resolution in the offline analysis. A method to directly correct for the position-dependent time fluctuations was developed. In addition, a completely new algorithm is introduced, which combines each channel or hit time information with appropriate weights. The effect of these analyses were evaluated using MC simulation.

Finally, an evaluation of the pTC resolution was performed to yield the value of $\sim$ 38.4 ps, taking into account the newly-found position-dependent time fluctuations. Furthermore, an estimation of the deterioration of the pTC resolution was made, considering the effect from radiation damage to SiPMs. The obtained value of $\sim$ 45.9 ps is expected to be improved to $\sim$ 41.1 ps by the various attempts introduced in this thesis. Thus, the required resolution of $\leq$ 46 ps is expected to be achieved even in the long term.

Contents

Chapter 1

Introduction

Here I introduce the overall picture of this thesis.

1.1 Particle physics today

Particle physics is a branch of physics that studies the nature and the interactions of elementary particles which constitute the universe. The ultimate goal of this particular branch of physics is to understand *everything* (that is to say all the elementary particles and the fundamental forces) in the universe, in the simplest form. The Standard Model (SM) is probably the most beautiful and successful theory particle physicists have come up with so far. It is a theory, developed in the latter half of the 20th century, describing the three fundamental forces; the electromagnetic, the weak and the strong, as well as classifying all known elementary particles. Furthermore, it has demonstrated great successes in predicting experimental results such as the existence of the Higgs boson, which had been the last piece of the puzzle to complete the SM and was discovered at the Large Hadron Collider (LHC) in 2012.

Although the SM is believed to be a self-consistent theory and has been successful in many aspects, it is a common belief amongst particle physicists that the SM is not the ultimate *theory of everything* they believe to exist. For one reason, it fails to incorporate any viable dark matter particle nor the fourth fundamental force, the gravitational force. For another, it does not give any answers to the important questions the ultimate theory ought to, such as the origin of the matter-antimatter asymmetry and the multiple generations of fermions. Nowadays, the SM is commonly regarded as a low-energy approximation of a more general theory. That is why particle physicists, theorists and experimentalists alike, are now searching for new physics beyond the Standard Model in the high energy region as a hint for the desired ultimate theory.

1.2 Charged lepton flavor violation

There are various ways in which one can search for new physics in the high energy region. One way is to directly produce new particles using colliders, thus exploring physics in $\mathcal{O}(1)\,\mathrm{TeV}$ energy scales ("energy frontier"). On the other hand, "intensity frontier" experiments attempt to observe interactions of BSM physics on SM particles via very

precise measurements, thus enabling new physics search in $\mathcal{O}(\gg 10)$ TeV energy scales. Indirect searches in intensity frontier experiments can be a powerful probe into high-energy physics because they do not require the new particle to be present in the final state. One potential observation target for such experiments is the charged lepton flavor violation (cLFV).

Conservation of lepton flavor is incorporated in the SM, but it is not theoretically required. In fact, the historical non-observation of lepton-flavor-violating processes led to the notion of distinct lepton flavors and their conservation. However, neutrino oscillation, which is forbidden in the SM due to the assumption of massless neutrinos, was discovered in 1998, meaning that lepton flavor is violated in the neutral lepton sector. This gives rise to the possibility of lepton flavor violation in the charged lepton sector too, making cLFV search more important than ever before. Various experiments in search for rare decays of charged leptons are now ongoing.

1.3 MEG II experiment

The MEG II experiment is one such experiment which searches for the charged-lepton-flavor-violating decay of muons, $\mu \to e\gamma$. The current most stringent upper limit on the branching ratio of this particular decay is set by the MEG experiment, the forerunner of the MEG II experiment, to be 4.2×10^{-13} (at 90% confidence level). The MEG II experiment aims to further enhance the sensitivity by one order of magnitude by making full use of the high-intensity muon beam available at Paul Scherrer Institut. Sophisticated detectors with high resolutions are necessary to cope with the high background rate in such an extreme beam-rate condition.

1.4 Pixelated timing counter

The pixelated timing counter (pTC) is the positron timing detector for the $\mu^+ \to e^+\gamma$ decay in the MEG II experiment. It consists of 512 small pixels and each pixel consists of a 120 mm $\times$ (40 / 50) mm $\times$ 5 mm fast plastic scintillator with 6 series-connected SiPMs at both ends. The pixelated design of the detector reduces pileup of positrons significantly and is expected to realize a time resolution below 40 ps by a multiple-pixel-hit scheme. Furthermore, the fast time response of these pixels allow the pTC to be used as an online timing trigger and enables an effective reduction of the trigger rate and the data size.

1.5 Structure of this thesis

This thesis is composed of four parts. The first part is an introduction. The physics motivation for the $\mu \to e\gamma$ search is stated in chapter 2, and the overview of the MEG II experiment, concentrating on the upgrade concepts from the MEG experiment, is described in chapter 3. In chapter 4, the pTC is introduced, which is the theme of this thesis, along with all that has been achieved by the pTC group in the past years.

The second part concerns the long-term operation of the pTC. In chapter 5 are described the assembly procedure of spare pixels and their single-pixel performance. In

chapter 6, we discuss the effect of radiation damage to SiPMs, especially a gradient damage to series-connected SiPMs, on the pTC performance. To put it simply, a newly-found effect was discovered to significantly worsen the pTC resolution, and therefore, the rest of this thesis focuses on various ways to recover the pTC resolution. In chapter 7 is introduced the first attempt to suppress the resolution deterioration; by optimizing the operation and the analysis parameters.

The third part mainly involves the analysis method of the pTC. In chapter 8 and 9, we discuss possible ways to improve the pTC resolution in the offline analysis. Their effects are evaluated using MC simulation. In chapter 10, an evaluation of the pTC resolution is performed. In addition, the extent to which the resolution is expected to deteriorate in the three-year physics data taking is discussed, together with the impact of the newly-developed algorithms and optimization schemes on the pTC resolution.

In the fourth and last part, I summarize the contents of this thesis. I conclude by stating some future tasks and prospects concerning the pTC towards the physics run.

Part I

MEG II Experiment

Chapter 2

Physics Motivation

In this chapter is described the physics motivation for the $\mu \to e\gamma$ search. This muon decay is strictly forbidden in the SM, but predicted at observable branching ratios of $\mathcal{O}(10^{-13})$–$\mathcal{O}(10^{-14})$ in many promising new physics models.

2.1 The Standard Model and its limitations

2.1.1 Standard Model

In modern particle physics, the Standard Model (SM) has been the most successful theory to describe the elementary particles and their interactions. Fig. 2.1 shows all the elementary particles and their classification in the SM.

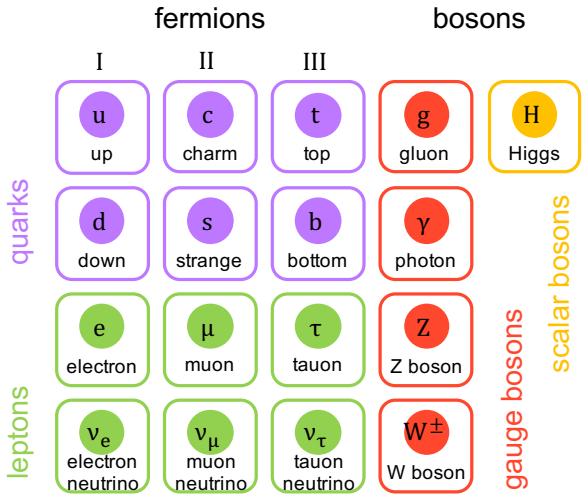

Figure 2.1: Elementary particles in the SM.

The SM postulates a local $\mathrm{SU(3)_C} \times \mathrm{SU(2)_L} \times \mathrm{U(1)_Y}$ gauge symmetry and this gauge symmetry gives rise to the three fundamental interactions. The $\mathrm{SU(3)_C}$ corresponds to the symmetry group of quantum chromodynamics (QCD) which describes the strong interaction. The unified interaction of the electromagnetic and the weak, is incorporated

in the SM by interpreting the $SU(2)_L \times U(1)_Y$ as a group of gauge transformations under which the Lagrangian is invariant.

In a quantized gauge theory, gauge bosons are quanta of the gauge fields, which means that the SM has the same number of gauge bosons as the number of generators of the gauge field. The $SU(3)_C$ symmetry group yields 8 generators, corresponding to gluons, the $SU(2)_L$ symmetry group yields 3 generators which in essence corresponds to W and Z bosons, and the $U(1)_Y$ symmetry group yields one generator, corresponding to photons. Apart from these, the SM incorporates another scalar boson called the Higgs boson, which is responsible for providing the mass for each particle via the Higgs mechanism.

The SM also incorporates 12 particles with 1/2 spin called fermions, and successfully classifies them depending on how they interact. Quarks can interact via all three interactions whereas leptons only interact weakly or electromagnetically. Tab. 2.1 and Tab. 2.2 show the basic characteristics of the SM particles.

Table 2.1: Fermions in the SM [1].

Fermions (spin1/2)					
Quarks			Leptons		
Flavor	Charge	Mass [MeV/c^2]	Flavor	Charge	Mass [MeV/c^2]
up	$+2/3$	$2.2^{+0.5}_{-0.4}$	e	-1	$0.5109989461 \pm 0.0000000031$
down	$-2/3$	$4.7^{+0.5}_{-0.3}$	ν_e	0	0
charm	$+2/3$	$(1.275^{+0.025}_{-0.035}) \times 10^3$	μ	-1	$105.6583745 \pm 0.0000024$
strange	$-2/3$	95^{+9}_{-3}	ν_μ	0	0
top	$+2/3$	$(173.0 \pm 0.4) \times 10^3$	τ	-1	1776.86 ± 0.12
bottom	$-2/3$	$4.18^{+0.04}_{-0.03}$	ν_τ	0	0

Table 2.2: Bosons in the SM [1].

Gauge bosons (spin 1)			Scalar bosons (spin 0)	
Boson	Force	Mass [GeV/c^2]	Boson	Mass [GeV/c^2]
photon	electromagnetic	0	Higgs	125.18 ± 0.16
W boson	charged weak	80.379 ± 0.012		
Z boson	neutral weak	91.1876 ± 0.0021		
gluon	strong	0		

2.1.2 Limitations of the SM

Although the SM has successfully provided astonishingly accurate descriptions of phenomena in a wide range of energy scales, we also know that the SM is not the ultimate *theory of everything* we believe to exist. For one thing, it contradicts with some of the latest experimental results. One such example is the neutrino mass. Although the mass of most elementary particles are free parameters in the SM, the neutrinos are assumed to be massless as shown in Tab. 2.1. However, neutrino oscillation has been observed in various experiments, indicating that neutrinos are indeed massive. This experimental fact

obviously contradicts with the SM and proves that the SM does not correctly depict the universe.

For another, the SM has some gaping holes where it fails to give any explanation on the observed phenomena. For instance, the SM does not contain any viable dark matter particle, which means that the SM is only capable of explaining a small proportion of the matter in the universe. Nor does it state anything concerning the gravitational force.

Finally, the SM does not give any answers to the important questions we believe the ultimate theory ought to; the origin of the matter-antimatter asymmetry and the multiple generations of fermions, why the electric charge is quantized, and so on.

However, the fact that the SM accurately describes various phenomena at relatively low energy regions suggests that it is a low-energy approximation of a more general theory. Many promising models beyond the SM (BSM) have already been proposed and are under verification by various experiments.

2.2 BSM models

Many theoretical models have already been proposed to incorporate experimental results the SM cannot explain, and also to naturally account for the questions the SM does not give answers to. Here I will introduce some of them which seem promising steps towards the *theory of everything*.

2.2.1 Grand Unified Theory

The SM covers three of the four fundamental forces, two of which are unified as the electroweak force based on the $\mathrm{SU(2)_L} \times \mathrm{U(1)_Y}$ symmetry group. Although this was an obvious success to understand the universe more simply, it still does not explain, for instance, the reason for electric charge quantization, as the electromagnetic force is characterized by an abelian symmetry which allows arbitrary charge assignments.

However, the quantization of electric charge can be explained by postulating that the strong interaction and the electroweak interaction are actually embedded in a unified interaction described by a single, larger simple symmetry group. The Grand Unified Theory (GUT) assumes just that. It states that the three fundamental interactions unify into a single electronuclear interaction at a high energy scale (GUT scale) and is characterized by one larger gauge symmetry having several force carriers but one unified coupling constant. This is depicted in Fig. 2.2. It shows how the three forces are unified in the GUT energy scale of $\mathcal{O}(10^{16})$ GeV by assuming SUSY (c.f. 2.2.2) particles in $\mathcal{O}(1)$ TeV energy scale.

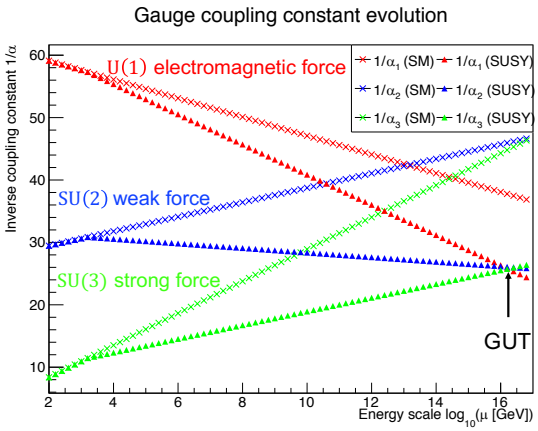

Figure 2.2: Evolution of the coupling constants in the SM and in the SUSY-GUT model.

2.2.2 Supersymmetry

Another promising theory is the supersymmetry (SUSY) [2]. The SM succeeded in explaining the non-zero masses of particles by the Higgs mechanism, which was proven to be correct by the discovery of the Higgs boson, but it fails to explain the mass scale. The SM is an effective field theory that is expected work below a certain energy scale that lies around $\mathcal{O}(10^{16})$ GeV (GUT scale) or $\mathcal{O}(10^{19})$ GeV (Planck scale). This means that unlike the other SM particles whose masses are protected by gauge or chiral symmetries, we would need some extremely unnatural fine tuning between the bare Higgs mass and the quadratic radiative corrections to achieve the observed Higgs mass which is 17 orders of magnitude below the Planck scale.

The SUSY provides an elegant solution to this hierarchy problem. SUSY is a symmetry which connects fermions and bosons, that is particles with half-integer spins and integer spins. Their transformations are given by

$$\mathcal{Q}|Fermion\rangle = |Boson\rangle \tag{2.1}$$
$$\mathcal{Q}^{\dagger}|Boson\rangle = |Fermion\rangle \tag{2.2}$$

where $\mathcal{Q}$ is the SUSY generator. Applying these to the SM inevitably produces a supersymmetric partner for each SM particle as shown in Tab. 2.3. This seems to complicate matters at first glance, but these extra particles actually have the effect of cancelling out the contributions to the Higgs mass from the SM partners as shown in Fig. 2.3. Thus, the supersymmetric SM is capable of naturally explaining the low mass of the Higgs boson.

Table 2.3: Supersymmetric partners of SM particles.

	SM particles		SUSY particles	
SM particle type	Particle	Spin	Particle	Spin
Fermion	quark	1/2	squark	0
	lepton	1/2	slepton	0
Gauge boson	photon	1	photino	1/2
	W boson	1	wino	1/2
	Z boson	1	bino	1/2
	gluon	1	gluino	1/2
Scalar boson	Higgs	0	Higgsino	1/2

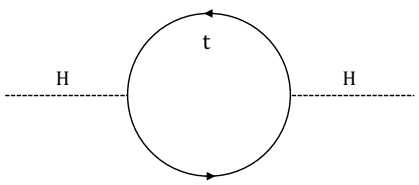

(a) Radiative corrections to the Higgs mass from top quark loop.

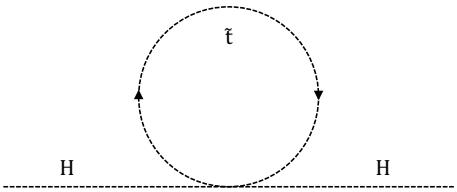

(b) Radiative corrections to the Higgs mass from stop quark loop.

Figure 2.3: One-loop corrections to the Higgs mass.

There are also other benefits of assuming SUSY particles. For one, as already shown in Fig. 2.2, a precise unification of the gauge coupling constants can be achieved by assuming the existence of SUSY particles in $\mathcal{O}(1)$ TeV energy scale. For another, it provides viable candidates for dark matter as many supersymmetric models predict the lightest SUSY particle to be stable, electrically neutral and to weakly interact with the SM particles.

2.2.3 Seesaw mechanism

Although the neutrino mass is strictly zero in the SM, neutrinos were found to be massive by the discovery of neutrino oscillation. However, why neutrinos have a very different mass scale to the other fermions still remains an open question. The seesaw mechanism can naturally account for the low mass of neutrinos by assuming two or more additional right-handed neutrino fields inert under the electroweak interactions and the existence of a large mass scale.

The neutrino Lagrangian in the most general form can be expressed as

$$\mathcal{L}_\nu = -\overline{\Psi}\mathrm{i}\gamma^\mu\partial_\mu\Psi - m_D(\overline{\Psi}_L\Psi_R + h.c.) - \frac{m_L}{2}(\overline{\Psi}^c_R\Psi_L + h.c.) - \frac{m_R}{2}(\overline{\Psi}^c_L\Psi_R + h.c.) \quad (2.3)$$

where m_D is the Dirac mass, m_L, m_R are the Majorana masses of left- and right-handed neutrinos respectively, Ψ_L, Ψ_R are the Weyl spinors of left- and right-handed neutrinos respectively, and $\Psi = \Psi_L + \Psi_R$. This equation can be simplified using two Majorana fields

$$N_1 = \frac{\Psi_L + \Psi^c_L}{\sqrt{2}}, \quad N_2 = \frac{\Psi_R + \Psi^c_R}{\sqrt{2}} \quad (2.4)$$

to be

$$\begin{aligned}\mathcal{L}_\nu &= -\overline{N}_1 \mathrm{i}\gamma^\mu \partial_\mu N_1 - \overline{N}_2 \mathrm{i}\gamma^\mu \partial_\mu N_2 - m_D(\overline{N}_1 N_2 + \overline{N}_2 N_1) - m_L \overline{N}_1 N_1 - m_R \overline{N}_2 N_2 \\ &= \begin{pmatrix}\overline{N}_1, & \overline{N}_2\end{pmatrix} (\mathrm{i}\gamma^\mu \partial_\mu + \boldsymbol{M}_\nu) \begin{pmatrix} N_1 \\ N_2 \end{pmatrix}, \end{aligned} \tag{2.5}$$

where

$$\boldsymbol{M}_\nu = \begin{pmatrix} m_L & m_D \\ m_D & m_R \end{pmatrix} \tag{2.6}$$

is the mass matrix of neutrinos. The two fields obtained by the diagonalization of Eq. (2.6) contain both L and R components and do not have fixed chiralities. If we think within the SM except for assuming the existence of right-handed neutrinos with a huge mass, $m_L = 0$, m_D can roughly be the same as the masses of other fermions, and $m_R \gg m_D$. In this case the eigen solutions can be obtained as

$$|\nu'\rangle \simeq |N_1\rangle - \frac{m_D}{m_R}|N_2\rangle, \quad |N\rangle \simeq |N_2\rangle + \frac{m_D}{m_R}|N_1\rangle \tag{2.7}$$

$$m_{\nu'} \simeq -\frac{m_D^2}{m_R}, \quad m_N \simeq m_R \tag{2.8}$$

where $|\nu'\rangle$ and $|N\rangle$ are the eigenvectors, and $m_{\nu'}$ and m_N are their mass eigenvalues respectively. The apparently negative mass, $m_{\nu'}$, can be turned positive by setting $|\nu\rangle = \gamma^5|\nu'\rangle$, in which case

$$m_\nu \cdot m_R = m_D^2 \tag{2.9}$$

holds. Eq. (2.9) effectively depicts the seesaw mechanism, which explains the small observed neutrino mass, m_ν, by assuming the existence of right-handed neutrinos with a large mass m_R, which still remains to be discovered.

2.3 Charged lepton flavor violation

2.3.1 Possibility of charged lepton flavor violation

Not much is yet understood about the flavors of fermionic elementary particles. We know from observation that at least three generations of fermions exist, and that further generations are disfavored by measurements. However, we are none the wiser about the origin of multiple generations or why different generations have such a large difference in the mass scale.

Furthermore, flavor mixing amongst generations is not well-understood. While the SM accounts for the flavor mixing in the quark sector via the CKM matrix, it strictly forbids flavor mixing in the lepton sector. However, the flavor conservation of leptons is not theoretically required. In fact, the flavor conservation in the charged lepton sector derives from a non-observation of charged lepton flavor violation (cLFV), and the flavor conservation in the neutral lepton sector simply derives from the assumption of massless neutrinos.

In any case, neutrino oscillation was discovered proving that neutrinos can indeed change their flavor. This strongly hints the possibility of lepton flavor violation (LFV)

in the charged lepton sector too, as lepton flavor conservation was not required in the first place. In fact, many BSM models, including those introduced in 2.2, incorporate cLFV processes at reasonably observable rates, and many experiments are now ongoing in search for these rare processes.

2.3.2 History of cLFV search

Since the discovery of muons in 1937, various searches for cLFV muon decays have been conducted. The first result came in 1947 when Pontecorvo first searched for the $\mu \to e\gamma$ process using cosmic rays [3]. In the 1950s, the upper limits of cLFV branching ratios improved drastically through experiments using accelerators, and they have been improving ever since. Fig. 2.4 shows the upper limits of the branching ratios for cLFV processes set by experiments over the past century.

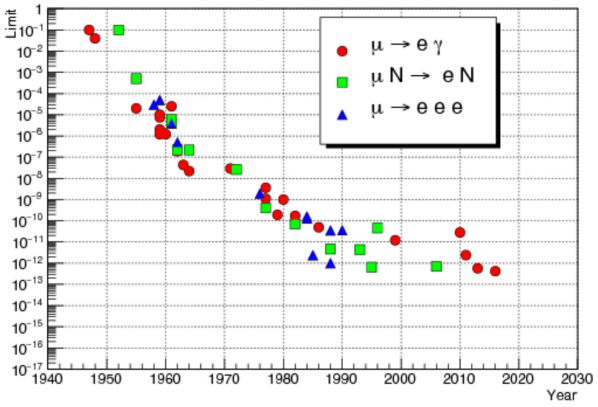

Figure 2.4: Experimental upper limits on cLFV muon decay channels [4].

In principle, the tau lepton would be the best object for the cLFV search, as it has a stronger coupling to the new physics and possesses more cLFV channels (e.g. $\tau \to e\gamma$, $\tau \to \mu\gamma$, $\tau \to eee$, etc). However, the current availability of muons in large quantities at accelerators renders the muon cLFV searches more powerful. Thus, the following cLFV channels, more often known as the golden channels, are being searched all around the world:

- $\mu \to e\gamma$
- $\mu N \to eN$ (muon conversion)
- $\mu \to eee$

where N denotes an atomic nucleus. The current upper limits of these processes are set by the MEG, the SINDRUM II, and the SINDRUM experiments to be 4.2×10^{-13} [5], 7×10^{-13} [6], and 1×10^{-12} [7] respectively. The branching ratios of these three decays depend sensitively on the new physics model. Therefore, it is very important to measure the decay rate for each of these channels, even after the cLFV has been discovered in one channel, to put further constraints on the possible models behind the process.

2.4 $\mu \to e\gamma$ decay

2.4.1 Muon decay in the SM

Muon belongs to the second generation of charged leptons in the SM. Its physical properties are summarized in Tab. 2.4. It has a relatively long lifetime, which makes rare muon decay searches possible.

Table 2.4: Basic physical parameters of muon [1].

Parameter	Value
Mass	$105.6583745 \pm 0.0000024\,\mathrm{MeV}$
Mean lifetime	$(2.1969811 \pm 0.0000022) \times 10^{-6}\,\mathrm{s}$
Magnetic moment anomaly	$(11659209 \pm 6) \times 10^{-10}$
Electric dipole moment	$(-0.1 \pm 0.9) \times 10^{-19} e\,\mathrm{cm}$

After its lifetime, a muon decays into other particles, which is summarized in Tab. 2.5. These are the decay modes that can be the background in searching for cLFV muon decays.

Table 2.5: Muon decay modes [1]. E_e and E_γ denote the energies of electron and photon respectively. The decays from μ^+ will be the charge conjugate of these modes.

Decay mode	Branching ratio	Conditions
$\mu^- \to e^- \overline{\nu}_e \nu_\mu$	~ 1	
$\mu^- \to e^- \overline{\nu}_e \nu_\mu \gamma$	$(6.0 \pm 0.5) \times 10^{-8}$	$E_e > 45\,\mathrm{MeV}$, $E_\gamma > 40\,\mathrm{MeV}$
$\mu^- \to e^- \overline{\nu}_e \nu_\mu e^+ e^-$	$(3.4 \pm 0.4) \times 10^{-5}$	$E_\gamma > 14.5\,\mathrm{MeV}$

2.4.2 $\mu \to e\gamma$ in the SM

The SM strictly prohibits LFV, and therefore the $\mu \to e\gamma$ decay. However, by considering the already-discovered neutrino oscillation, we actually obtain a non-zero $\mu \to e\gamma$ branching ratio. A possible Feynman diagram is shown in Fig. 2.5. Here we follow the calculations in [8].

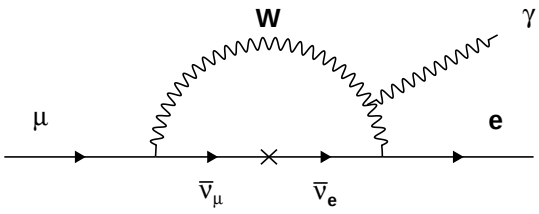

Figure 2.5: Possible $\mu \to e\gamma$ decay considering neutrino oscillation in addition to the SM.

Radiative decays of the generic lepton decay $l_1 \to l_2 + \gamma$ proceed through electromagnetic gauge-invariant transition amplitudes of the form

$$\mathcal{M} = \frac{eG_F m_{l_1}}{16\sqrt{2}\pi^2}\epsilon^\mu q^\nu \bar{l}_2(p_2)\sigma_{\mu\nu}\big(D_R\frac{1+\gamma_5}{2} + D_L\frac{1-\gamma_5}{2}\big)l_1(p_1) \tag{2.10}$$

where $q = p_1 - p_2$, $\sigma_{\mu\nu} = \frac{i}{2}[\gamma_\mu, \gamma_\nu]$, and D_R and D_L are model-dependent transition dipole moments. In the case of $\mu \to e\gamma$, $m_\mu \gg m_e$ holds, in which case the amplitude leads to the decay rate

$$\Gamma(\mu \to e\gamma) = \frac{\alpha G_F^2 m_\mu^5}{2048\pi^2}(|D_R|^2 + |D_L|^2) \tag{2.11}$$

and the branching ratio

$$\begin{aligned}\mathcal{B}(\mu \to e\gamma) &= \frac{3\alpha}{32\pi}(|D_R|^2 + |D_L|^2)\mathcal{B}(\mu \to e\nu_\mu\overline{\nu}_e) \\ &\simeq \frac{3\alpha}{32\pi}(|D_R|^2 + |D_L|^2)\end{aligned} \tag{2.12}$$

as $\mathcal{B}(\mu \to e\nu_\mu\overline{\nu_e}) \simeq 1$. Considering neutrino oscillation in addition to the SM, D_R and D_L can be expressed as

$$D_L \simeq \frac{1}{3}\sin 2\theta_{13}\sin\theta_{23}e^{-i\delta}\frac{\Delta m_{32}^2}{m_W^2} \tag{2.13}$$

$$D_R = 0 \tag{2.14}$$

which leads to the final branching ratio

$$\mathcal{B}(\mu \to e\gamma) \simeq 10^{-54} \times \frac{\sin^2 2\theta_{13}}{0.15} \tag{2.15}$$

$$\sim \mathcal{O}(10^{-54}) \tag{2.16}$$

by applying $\theta_{13} \sim 9^\circ$ [9].

Thus, neutrino oscillation gives us a non-zero branching ratio of $\mu \to e\gamma$, but its value is extremely suppressed by the fourth power of the mass ratio between the W boson and and neutrinos (see Eq. (2.13)). This means that we have almost no $\mu \to e\gamma$ background from the SM with neutrino oscillation, and that the observation of this process would be a clear proof of new physics beyond the SM.

2.4.3 $\mu \to e\gamma$ in BSM models

2.4.3.1 Model-independent approach

A model-independent Lagrangian for $\mu \to e\gamma$ decay can be written as

$$\mathcal{L}_{\mu\to e\gamma} = -\frac{4G_F}{\sqrt{2}}\left[m_\mu A_R \overline{\mu}_R \sigma^{\mu\nu} e_L F_{\mu\nu} + m_\mu A_L \overline{\mu}_L \sigma^{\mu\nu} e_R F_{\mu\nu} + h.c.\right] \tag{2.17}$$

where A_R and A_L are the coupling constants corresponding to the right-handed process, $\mu \to e_R\gamma$, and the left-handed process, $\mu \to e_L\gamma$, respectively. The differential angular distribution of $\mu \to e\gamma$ can then be obtained from Eq. (2.17) as

$$\frac{dB(\mu \to e\gamma)}{d\cos\theta_e} = 192\pi^2\big(|A_R|^2(a - P_\mu\cos\theta_e) + |A_L|^2(a + P_\mu\cos\theta_e)\big) \tag{2.18}$$

where P_μ is the magnitude of the muon polarization, and θ_e is the angle between the muon polarization and the positron momentum in the muon rest frame. A_R and A_L depend on the new physics model, so once the $\mu \to e\gamma$ decay is discovered, additional measurements of the positron emission angle with respect to the polarized muon would further restrict the BSM models.

2.4.3.2 SUSY

As explained in 2.2.2, the introduction of SUSY is one of the most prevailing extensions of the SM. It naturally suppresses the divergence of the Higgs mass, and also provides candidate particles for dark matter. Even the minimum SUSY extension of the SM (MSSM) incorporates huge degrees of freedom in the parameter space, and therefore it is widely considered within the constraints to meet the phenomenological observations.

Within the MSSM, a muon is allowed to decay into a positron and a photon via a loop of neutralino and sleptons as shown in Fig. 2.6. These decays are made possible if the slepton mass matrix in the new physics model has off-diagonal elements. In these cases, the decay rate is expected to be well within the experimentally observational level.

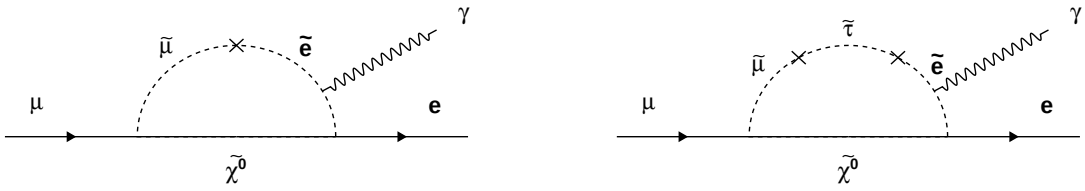

Figure 2.6: Examples of $\mu \to e\gamma$ decay in the SUSY model.

2.4.3.3 SUSY seesaw

The seesaw mechanism is well-motivated as it naturally explains the small mass of neutrinos with the assumption of right-handed Majorana neutrinos as explained in 2.2.3. In the SUSY seesaw model, the right-handed neutrino supermultiplets, the Majorana neutrino mass matrix and a new Yukawa coupling matrix are additionally included in the lepton sector Lagrangian. As the Yukawa coupling matrix for electrons and neutrinos are independent, off-diagonal elements arise in the left-handed slepton mass matrix as

$$(m^2_{\tilde{l}_L})_{ij} \simeq -\frac{1}{8\pi^2}(y_\nu)^*_{ki}(y_\nu)_{kj}m_0^2(3+|A_0|^2)\ln(\frac{M_P}{M_R}) \tag{2.19}$$

where y_ν is the Yukawa coupling matrix of neutrinos, m_0 is the universal scalar mass, A_0 is the universal trilinear coupling, M_P is the Planck mass, and M_R is the right-handed neutrino mass [10]. In this model, only right handed neutrinos contribute to the decay, meaning that the decay will have an angular distribution in the form of $1 - P_\mu \cos\theta_e$. Fig. 2.7 shows the branching ratios of $\mu \to e\gamma$ and $\tau \to \mu\gamma$ expected in this model. Considering the neutrino mixing angle $\theta_{13} \sim 9^\circ$ [9], the magenta region shows more or less the parameter region we still have to search.

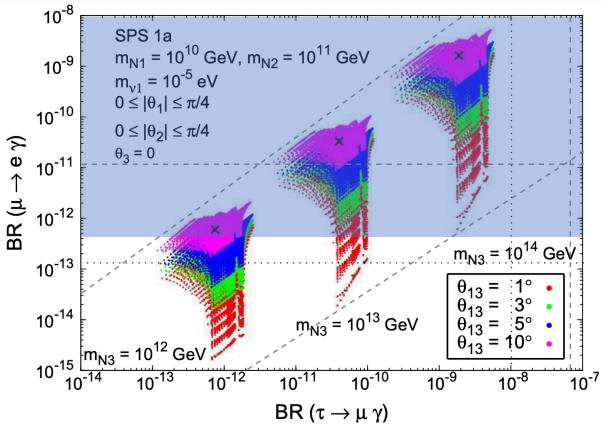

Figure 2.7: The branching ratio of $\mu \to e\gamma$ against $\tau \to \mu\gamma$ in the MSSM model with the seesaw mechanism. [11]. The current upper limit of the branching ratio of $\mu \to e\gamma$ [5] is added in blue to the original figure.

2.4.3.4 SUSY GUT

The SUSY GUT is also a well-motivated theory as it is capable of unifying the three gauge coupling constants via a larger symmetry group as explained in 2.2.1. The cLFV source in the SUSY GUT is quite different from that of the seesaw mechanism since it originates from off-diagonal elements in up quarks [12].

The smallest symmetry group satisfying this condition is SU(5), in which case off-diagonal elements appear in the right-handed slepton mass matrix as

$$(m^2_{\tilde{e}_R})_{ij} = -\frac{3}{8\pi^2}(V_R)_{i3}(V_R)^*_{j3}|y_u^{33}|^2 m_0^2(3 + |A_0^2|)\ln(\frac{M_P}{M_G}) \tag{2.20}$$

where V_R is a matrix to diagonalize the Yukawa coupling constant for leptons, y_u is the Yukawa coupling matrix of up quarks, and M_G is the GUT scale [10]. Thus, the $\mu \to e\gamma$ decay is made possible via right-handed slepton sector.

There are even larger symmetry groups, such as SO(10), which satisfy the unification condition, and are therefore promising candidates for the SUSY GUT. Fig. 2.8 shows the expected branching ratio of $\mu \to e\gamma$ against stau mass predicted by the SU(10) SUSY GUT.

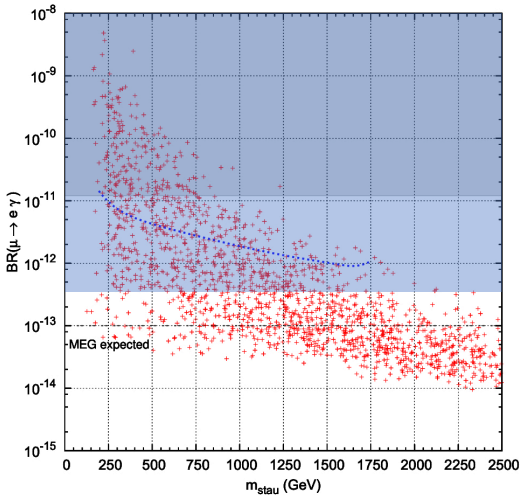

Figure 2.8: Branching ratio of $\mu \to e\gamma$ against stau mass expected in the SO(10) SUSY GUT [13]. The current upper limit of the branching ratio for $\mu \to e\gamma$ [5] is added in blue to the original figure.

2.4.3.5 Other models

Note that there are many other models which predict reasonably observable cLFV processes, such as the SM with a fourth generation of quarks and leptons [14], and the Randall-Sundrum model [15]. Therefore, the $\mu \to e\gamma$ search is an extremely promising probe for new physics beyond the SM. Both its discovery or its non-discovery at ultra-high sensitivity would give us the means to put stringent restrictions on the new physics model.

Chapter 3

MEG II Experiment

In this chapter, an overview of the MEG II experiment is given. After describing the principle of the $\mu \to e\gamma$ search, the MEG experiment is introduced as a preceding work of the $\mu \to e\gamma$ search, followed by a detailed explanation of the MEG II experiment focusing on the upgrade concepts from the MEG experiment.

3.1 Principle of $\mu \to e\gamma$ search

In experimental $\mu \to e\gamma$ search, muons are stopped in a target and are made to decay after their lifetime of $\mathcal{O}(10^{-6}\,\mathrm{s})$. The decay mode is identified by detecting the decay products and reconstructing the decay event. Positive muons are used to avoid the formation of muonic atoms in the target which can complicate the decay kinematics.

3.1.1 Signal

The kinematics of the $\mu^+ \to e^+\gamma$ is a simple two-body decay. In the rest frame of the muon, the muon emits back to back a time-coincident pair of a mono-energetic positron and a mono-energetic photon, as depicted in Fig. 3.1. Therefore, the signal can be identified by four observables satisfying the following conditions:

- $E_{e^+} = E_\gamma = \frac{m_\mu}{2} \simeq 52.8\,\mathrm{MeV}$
- $t_{e^+\gamma} = 0$
- $\theta_{e^+\gamma} = 180°$

where E_{e^+} and E_γ are the energies of the positron and the photon respectively, m_μ is the rest mass of muon, $t_{e^+\gamma}$ is the decay time difference between the positron and the photon, and $\theta_{e^+\gamma}$ is the opening angle between the positron and the photon.

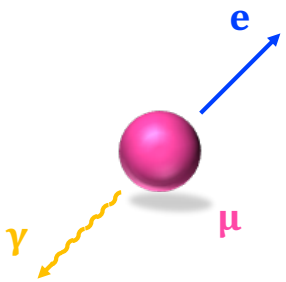

Figure 3.1: A kinematic diagram of the $\mu \to e\gamma$ decay.

The expected number of signals can be written in the form

$$N_{\text{sig}} = R_{\mu^+} \times T \times \Omega \times \mathcal{B} \times \epsilon_{e^+} \times \epsilon_\gamma \times \epsilon_{\text{s}} \tag{3.1}$$

where R_{μ^+} is the rate of muons stopping in the target, T is the total data acquisition time, Ω is the solid angle subtended by the positron and photon detectors, ϵ_{e^+} and ϵ_γ are the detection efficiencies of the positron and the photon respectively, and ϵ_{s} is the efficiency of the selection criteria. Each of the factors on the right hand side of Eq. (3.1) should be maximized to achieve the highest possible sensitivity, except for $\mathcal{B}$ which is determined by the BSM model.

3.1.2 Backgrounds

The background events in search for $\mu^+ \to e^+\gamma$ can be classified into two classes, the physics background and the accidental background. Both are depicted in Fig. 3.2. Since the kinematics of these background events are not exactly the same as that of signal events, in principle, we can identify them by measuring the four observables, E_{e^+}, E_γ, $t_{e^+\gamma}$, $\theta_{e^+\gamma}$, with high precision.

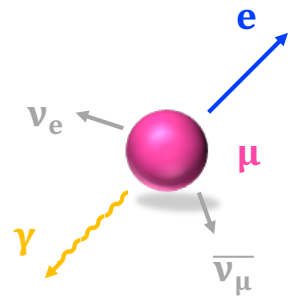

(a) Physics background

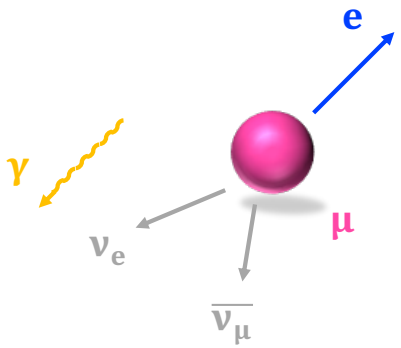

(b) Accidental background

Figure 3.2: Kinematic diagrams of background events for the $\mu \to e\gamma$ decay.

To discuss the expected number of background events, we introduce new quantities: $x = 2E_{e^+}/m_\mu$ and $y = 2E_\gamma/m_\mu$ which are the energies of the positron and the photon

respectively normalized to those of the signal, and $z = \theta_{e^+\gamma} - \pi$. Using these quantities, the search region of interest can be expressed as

$$\begin{cases} 1 - \delta x \leq x \leq 1 + \delta x & \text{(3.2a)} \\ 1 - \delta y \leq y \leq 1 + \delta y & \text{(3.2b)} \\ -\delta t_{e^+\gamma} \leq t_{e^+\gamma} \leq \delta t_{e^+\gamma} & \text{(3.2c)} \\ 0 \leq z \leq \delta z & \text{(3.2d)} \end{cases}$$

where the variables indicated with δ denote the range of the signal region for each corresponding observable.

3.1.2.1 Physics background

One type of background is the physics background. This occurs in a fraction of radiative muon decays (RMDs), which is depicted in Fig. 3.2a and can be written as $\mu^+ \to e^+\overline{\nu_e}\nu_\mu\gamma$. When the positron and the photon are emitted almost back to back, and little energy is carried out by the non-detectable neutrinos (i.e. $x \simeq 1$, $y \simeq 1$ and $z \simeq 0$), this decay mimics the signal and becomes a source of the physics background. Therefore, the probability of a muon becoming a physics background in an experiment can be obtained by integrating the RMD differential branching ratio $d\mathcal{B}(\mu^+ \to e^+\nu_e\overline{\nu_\mu}\gamma)$ over Eq. (3.2a), (3.2b) and (3.2d) as

$$\mathcal{B}_{\text{phys}} = \int_{1-\delta x}^{1+\delta x} dx \int_{1-\delta y}^{1+\delta y} dy \int_{0}^{\delta z} dz \frac{d\mathcal{B}(\mu^+ \to e^+\nu_e\overline{\nu_\mu}\gamma)}{dxdydz}. \tag{3.3}$$

Using this integrated value, the total expected number of physics background events can be expressed as

$$N_{\text{phys}} = R_{\mu^+} \times T \times \Omega \times \mathcal{B}_{\text{phys}} \times \epsilon_{e^+_{\text{phys}}} \times \epsilon_{\gamma_{\text{phys}}} \tag{3.4}$$

where $\epsilon_{e^+_{\text{phys}}}$ and $\epsilon_{\gamma_{\text{phys}}}$ are the detection efficiencies of background positrons and photons respectively.

3.1.2.2 Accidental background

The other type of background is the accidental background, in which a positron and a photon from independent sources mimic the signal and are detected as in Fig. 3.2b. The positron in this background event comes from a Michel decay of a muon $\mu^+ \to e^+\overline{\nu_e}\nu_\mu$, whereas the photon comes either from an RMD or an annihilation-in-flight (AIF) of a positron.

The fraction of Michel positrons entering the signal energy region, f_{e^+}, can be obtained by integrating the Michel positron energy spectrum, shown in Fig. 3.3, over Eq. (3.2a). As the spectrum is almost flat around the signal region ($x \simeq 1$),

$$f_{e^+} \simeq 2(\delta x) \tag{3.5}$$

approximately holds.

The fraction of photons entering the signal energy region, on the other hand, is more complicated, as it has contributions from both AIFs and RMDs. The AIF gamma spectrum depends on the material distribution in individual experiments, so here we focus on the contribution from RMDs. This can be obtained in a similar way, by integrating the RMD photon energy spectrum, shown in Fig. 3.4, over Eq. (3.2b). The fraction of photons entering the signal energy region can then be approximated to be

$$f_\gamma \simeq \frac{\alpha}{2\pi}(\delta y)^2\big(\ln(\delta y) + 7.33\big) \tag{3.6}$$

with the assumption of unpolarized muons. The detailed calculation can be found in [16].

The total number of expected accidental background events from RMD photons can then be written in the form

$$\begin{aligned} N_{\mathrm{acc(RMD)}} =& R_{\mu^+} \times f_{e^+} \times R_{\mu^+} \times f_\gamma \times \frac{(\delta z)^2}{4} \times 2(\delta t_{e^+\gamma}) \\ & \times T \times \Omega \times \epsilon_{e^+_{\mathrm{acc}}} \times \epsilon_{\gamma_{\mathrm{acc(RMD)}}} \end{aligned} \tag{3.7}$$

where $\epsilon_{e^+_{\mathrm{acc}}}$ and $\epsilon_{\gamma_{\mathrm{acc(RMD)}}}$ are the detection efficiencies of background positrons and photons respectively. The quadratic term of δz comes from the necessity to take into account the solid angle. By applying Eq. (3.5) and Eq. (3.6), the dependence of $N_{\mathrm{acc(RMD)}}$ on the beam rate and the signal region of each observable can be shown to be

$$N_{\mathrm{acc(RMD)}} \propto (R_{\mu^+})^2 \times \delta x \times (\delta y)^2 \times \delta t_{e^+\gamma} \times (\delta z)^2. \tag{3.8}$$

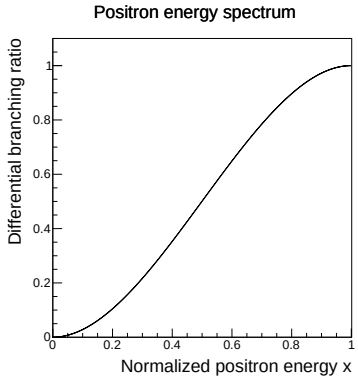

Figure 3.3: Positron energy spectrum from Michel decay

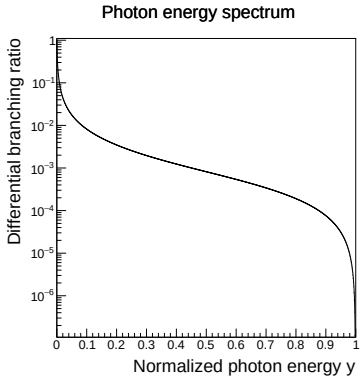

Figure 3.4: Photon energy spectrum from RMD

3.1.3 Experimental requirements

The physical requirements to achieve ultra-high sensitivity for $\mu \to e\gamma$ search can be summarized as maximizing Eq. (3.1) while minimizing Eq. (3.4) and Eq. (3.8). These in turn lead to the following experimental requirements.

Firstly, a high-intensity direct-current (DC) muon beam is required. High muon statistics is the first step to increase the number of signals in Eq. (3.1). However, while the signal increases linearly with the muon rate R_{μ^+}, the accidental background in Eq. (3.8) increases quadratically. Consequently, the overall muon intensity must be maximized while

minimizing the instantaneous muon intensity, which naturally results in the requirement of a high-intensity DC muon beam.

Secondly, the detectors must have high energy, time and position resolutions. Searching for such rare decays can only be achieved by an extreme reduction of the background. The use of high-intensity muon beam incidentally causes the accidental background to be dominant. Eq. (3.8) indicates that this can directly be suppressed by enhancing the resolution for each of the four observables. Eq. (3.3) indicates that the physics background can also be suppressed directly by high-resolution detectors.

While the two conditions stated above are the most crucial experimental requirements for $\mu \to e\gamma$ search, there are also other important requirements such as the ones below:

- Wide acceptance and high detection efficiency of each detector to earn the signal statistics.
- Low material distribution around the target to minimize accidental AIF photons.
- Capability of each detector to cope with the high-rate environment (e.g. radiation tolerance, high granularity to reduce pileup events, etc.).
- Fast electronics and trigger system.

3.2 MEG experiment

In this section the MEG experiment is introduced as a preceding work of the $\mu \to e\gamma$ search.

3.2.1 Overview

The MEG experiment searched for the $\mu \to e\gamma$ decay from 2008 to 2013 and set the current upper limit on the branching ratio, $\mathcal{B}(\mu \to e\gamma) < 4.2 \times 10^{-13}$ (at 90 % confidence level) [5]. The MEG experiment made use of the DC muon beam available at PSI in Switzerland. Fig. 3.5 shows the overall picture of the detectors used in the MEG experiment. Muons decay after stopping inside the target (3.2.2) and the decay products are measured by the surrounding detectors; positrons, bent into spirals by the COBRA magnet, are detected by the drift chamber and the timing counter (3.2.3), whereas photons are detected by the liquid-xenon calorimeter (3.2.4). The data acquisition in each detector is performed using Domino Ring Sampler chips (3.2.5).

The global coordinates in the MEG (and also MEG II) system are also depicted in Fig. 3.5. The origin is set to the target center and the z axis corresponds to the beam axis. Note also that the polar coordinates with respect to the z axis will also be referred to in the following discussions.

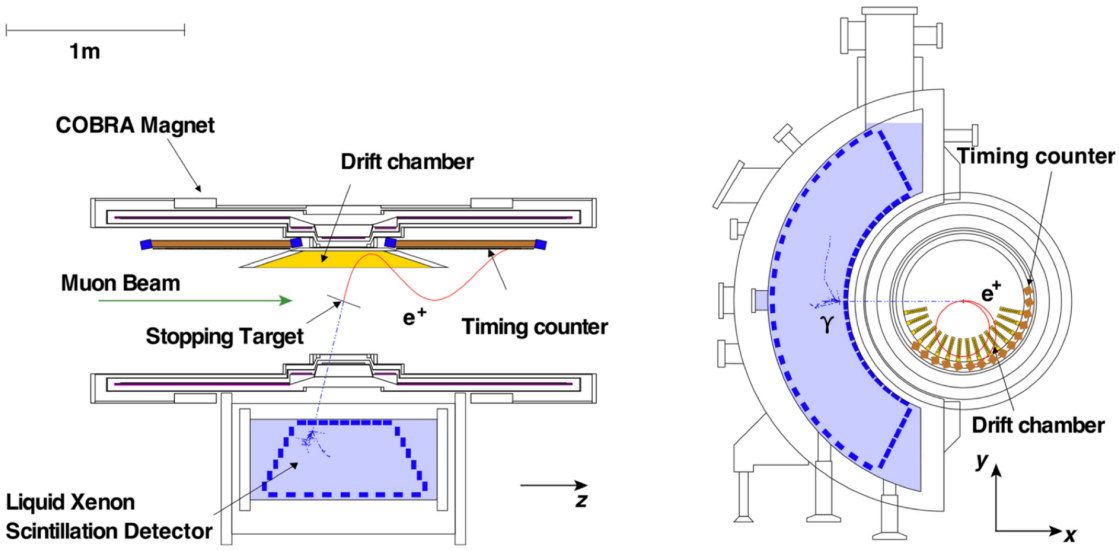

Figure 3.5: An overall picture of the detectors in the MEG experiment [17].

3.2.2 Beamline and target

The MEG experiment made use of the high-intensity DC muon beam available at PSI. The muons originate from a proton beamline. Protons from a hydrogen source are accelerated up to 590 MeV by a Cockcroft-Walton pre-accelerator and two cyclotrons. These accelerated protons produce pions via nuclear interactions in a target, which then decay into muons after being stopped in a target. The long lifetime of pions enables the production of a DC muon beam from the originally periodic proton beam. More details about the muon beamline at PSI are given in 3.3.2.

The muon stopping target used in the MEG experiment is shown in Fig. 3.6. It is composed of a 205 μm-thick layer of polyethylene and polyester in an elliptical shape with semi-major and semi-minor axes of 10 cm and 4 cm. The target was placed with an inclination of $\sim 20°$ with respect to the beam axis to maximize the muon stopping rate, while minimizing the scattering of observable decay products within the target.

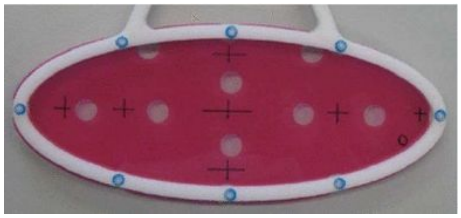

Figure 3.6: The muon stopping target in the MEG experiment mounted on a Rohacell frame [5].

While the maximum muon beam rate available at PSI is $\sim 10^8\,\mu^+/\mathrm{s}$, the MEG experiment operated at a lower beam intensity. This is due to a limitation of the detector performances. The consequential muon stopping rate at the target was $3 \times 10^7\,\mu^+/\mathrm{s}$.

3.2.3 Positron spectrometer

The positron spectrometer consists of three systems: the COBRA magnet, the drift chamber (DCH) and the timing counter (TC). The COBRA magnet is responsible for the trajectory of signal positrons, while the DCH and the TC reconstruct their track and timing respectively.

3.2.3.1 COBRA magnet

The COBRA magnet, which stands for the COnstant Bending RAdius magnet, is a superconducting solenoid developed specially for the MEG experiment [18]. It surrounds the target region completely, and also the DCH and the TC. It has a gradient magnetic field along z; 1.27 T at the center and 0.49 T at both ends. This gradient magnetic field is capable of leading the signal-like positrons (i.e. with energy of half the muon mass) to the DCH and the TC detector region, regardless of the positron emission angle. It is also capable of sweeping the positron outwards, to reduce pileup in the DCH and the TC. These characteristics are schematized in Fig. 3.7.

(a) (b)

Figure 3.7: A schematic view of the COBRA magnet showing (a) the weak dependence of the bending radius on the positron emission angle and (b) how it sweeps positrons away from the central region [17]. The labels in blue are added to the original figure.

3.2.3.2 Drift Chamber

The DCH is mainly responsible for providing the precise track of positrons [19]. It consists of 16 trapezoidal modules lined along ϕ direction as in Fig. 3.8. Each module consists of two detector planes with wires stretching parallel to the beam, and these two planes are staggered by half a drift cell to resolve the left-right position ambiguity as shown in Fig. 3.9, and determine the positron position in x-y plane. The z position is obtained by the charge division method and a method called the vernier pad method which is depicted in Fig. 3.10; the cathode foils are divided into two sub-cathodes, and the induced charge on each 5 cm zig-zag shaped pad provides the z coordinate.

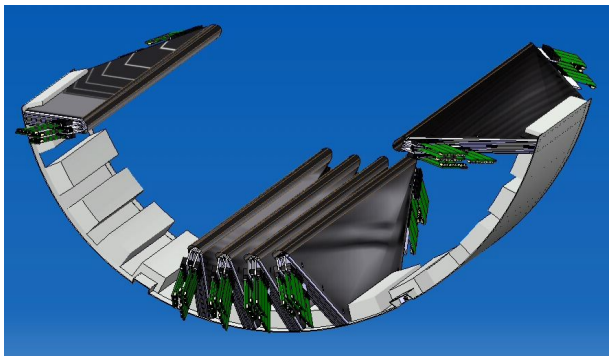

Figure 3.8: The design of the MEG DCH [20]. Only a fraction of the modules are depicted.

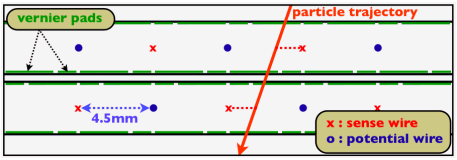

Figure 3.9: A schematic view of the drift cell structure [17].

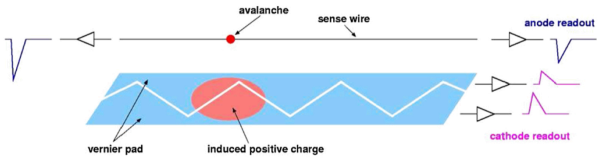

Figure 3.10: A schematic view of the vernier pad method [17].

The DCH must be of low material to minimize the multiple scattering of positrons and also the creation of accidental AIF photons. That is why each module is filled with a low-density gas mixture of He and C_2H_6 with the proportion of 1 : 1, and the support structure is also made of low-mass carbon fiber. With this design, the average amount of DCH material intercepted by a positron track is suppressed to $2 \times 10^{-3}\, X_0$.

3.2.3.3 Timing counter

The TC is responsible for providing the precise timing of positrons [21]. Its design is shown in Fig. 3.11. 15 scintillation counters, each 80 cm long and lined along ϕ direction, are placed below the DCH both upstream and downstream of the target. Each scintillation counter consists of a fast plastic scintillator (Saint-Gobain BC-404 [22]) and fine-mesh photomultiplier tubes (PMTs) (R5924 from Hamamatsu Photonics [23]) at both ends. The position information can also be obtained; the hit counter gives the ϕ position, while the time difference between the two channels in a counter gives the z position. Placed on top of the scintillation counters and perpendicular to the beam are scintillation fibers read out by avalanche photodiodes (APDs) (S8664-55 from Hamamatsu Photonics [24]). This can enhance the time resolution as well as improve the z position reconstruction.

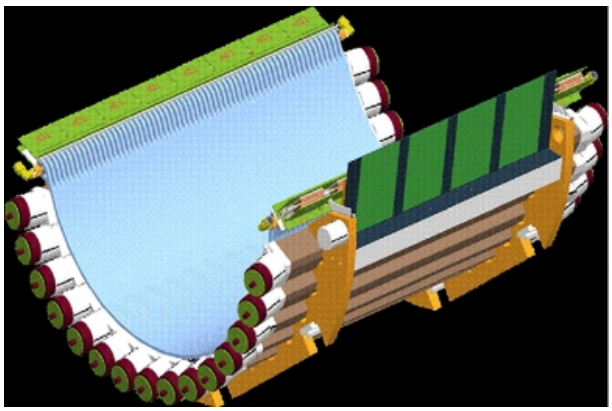

Figure 3.11: The design of the MEG TC [17].

3.2.4 Liquid-xenon calorimeter

The liquid-xenon (LXe) calorimeter is solely responsible for the energy, time and position reconstruction of photons [25]. Its design is depicted in Fig. 3.12. It has a C-shaped structure fitting the outer radius of the COBRA magnet and has the fiducial volume of ~ 800 L. It is filled with LXe, and its inner walls are covered with 846 PMTs (R9869 from Hamamatsu Photonics). It is a homogeneous calorimeter capable of fully containing the shower induced by signal photons, thus enabling the photon energy reconstruction. The fast time response of LXe allows a precise time reconstruction, and the photon direction can be inferred from the direction of the line between the reconstructed photon interaction vertex and the intercept of the positron trajectory at the muon stopping target.

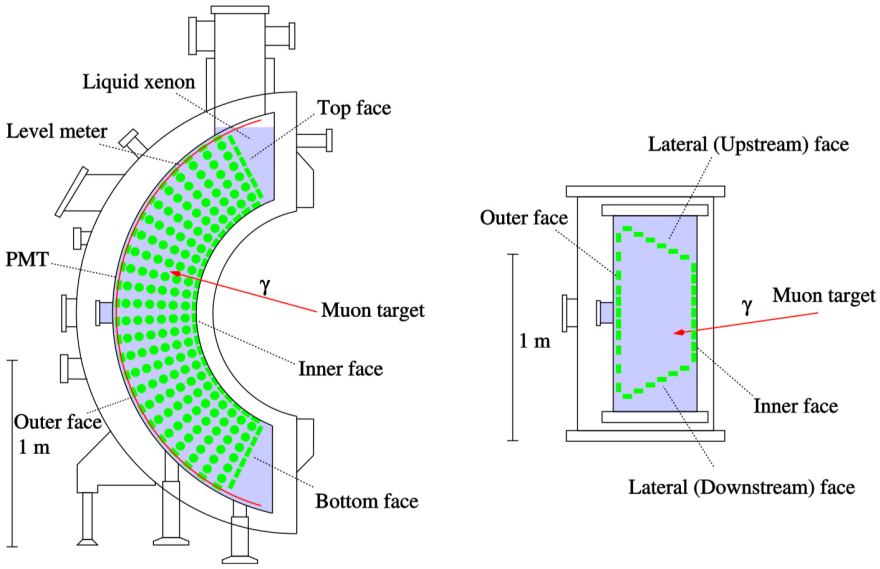

Figure 3.12: A schematic view of the MEG LXe calorimeter from the downstream side (left), and the top side (right) [17].

3.2.5 Data acquisition

The data acquisition (DAQ) system is dedicated to recording the signals from all the detectors in the experiment. The MEG experiment as a high-precision and high-rate experiment requires a significant precision and speed of the electronics, as well as the availability of raw waveforms for offline pileup reduction. This was achieved in the MEG experiment using high-speed waveform digitizers called Domino Ring Sampler 4 (DRS4) chips [26]. The chain of inverters in a ring, called the domino wave circuit, samples the signals. The sampled voltage information is kept in 1024 capacitors, which once triggered, is read out one by one by shift registers. The flexible sampling speed was fixed to 1.6 giga samples per second (GSPS) for the LXe calorimeter and the TC, and 0.8 GSPS for the DCH, which has less stringent timing requirements. A schematic view of the inverter chain and a functional block diagram of the DRS4 chip are shown in Fig. 3.13 and Fig. 3.14 respectively.

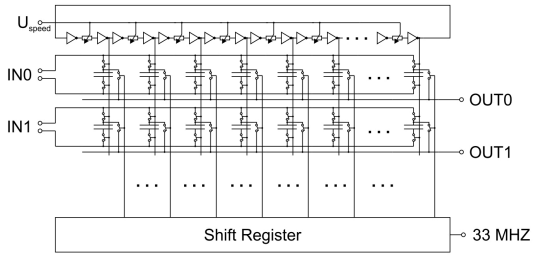

Figure 3.13: A simplified schematics of the inverter chain in the DRS4 chip [26].

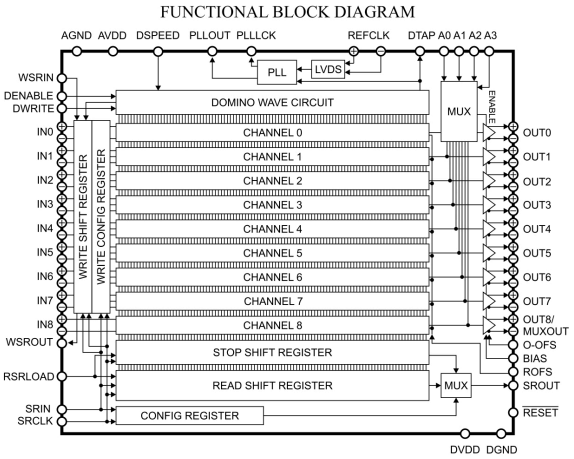

Figure 3.14: A functional block diagram of the DRS4 chip [26].

3.3 MEG II experiment

The MEG II experiment is an upgraded experiment of the MEG experiment, aiming to search for the $\mu \to e\gamma$ decay with one order higher sensitivity. Depicted in Fig. 3.15 is the overall picture of the MEG II experiment. Positron events are reconstructed by the cylindrical drift chamber and the pixelated timing counter, while photon events are reconstructed by the LXe calorimeter. Although the COBRA magnet used to control the positron tracks is retained from the MEG experiment, the radiative decay counter is newly installed. In this chapter, we discuss the necessary requirements for an upgrade, and the actual upgrades in each subsystem.

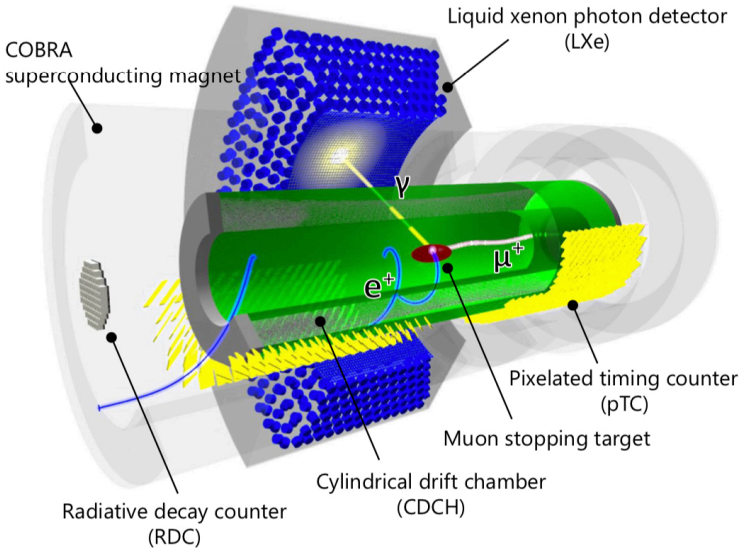

Figure 3.15: A schematic overview of the MEG II experiment [27].

3.3.1 From MEG to MEG II

As discussed in 3.1.3, the physical requirements to achieve a high sensitivity in $\mu \to e\gamma$ search is to maximize the number of signals given by Eq. (3.1) and to minimize the number of background events which are partly given by Eq. (3.4) and Eq. (3.8). The only realistic way to increase the number of signals is to increase the detection efficiency or the beam intensity. To achieve the former, the detector designs must be renewed. The latter is possible by utilizing the full beam available at PSI, but as explained in 3.1.3, the detector resolutions must be enhanced significantly to reduce the correspondingly-increased background.

This is exactly the concept of the MEG II experiment. It aims for one order higher sensitivity in the $\mu \to e\gamma$ search by

- Utilizing the maximum muon beam available at PSI.
- A significant improvement in each detector performance.

By detector performance, I mean increasing the detection efficiency to maximize the signal statistics, and enhancing the resolutions to minimize the background. Summarized in Tab. 3.1 and Tab. 3.2 respectively are the efficiencies and resolutions expected in the MEG II experiment compared to those achieved in the MEG experiment. The details of these variables will be discussed in the following subsections.

Table 3.1: The trigger and detection efficiencies achieved in the MEG experiment and expected in the MEG II experiment [27].

Efficiency type	Efficiency in MEG	Efficiency in MEG II
Trigger efficiency	99 %	99 %
Positron detection efficiency	30 %	70 %
Photon detection efficiency	63 %	69 %

Table 3.2: The resolutions achieved in the MEG experiment and expected in the MEG II experiment [5].

Observable	Resolution in MEG	Resolution in MEG II
Positron energy E_{e^+}	380 keV	130 keV
Positron emission angle θ_{e^+}	9.4 mrad	5.3 mrad
Positron emission angle ϕ_{e^+}	8.7 mrad	3.7 mrad
Normalized photon energy $2E_\gamma/m_\mu$ $(w < 2\,\text{cm})/(w > 2\,\text{cm})$	2.4 %/1.7 %	1.1 %/1.0 %
Photon conversion position $u_\gamma/v_\gamma/w_\gamma$	5 mm/5 mm/6 mm	2.6 mm/2.2 mm/5 mm
Time difference $t_{e^+\gamma}$	122 ps	84 ps

3.3.2 Beamline

The muon beam in the MEG II experiment originates from protons and are produced through three stages at PSI. Fig. 3.16 shows an overview of the PSI proton accelerator [28].

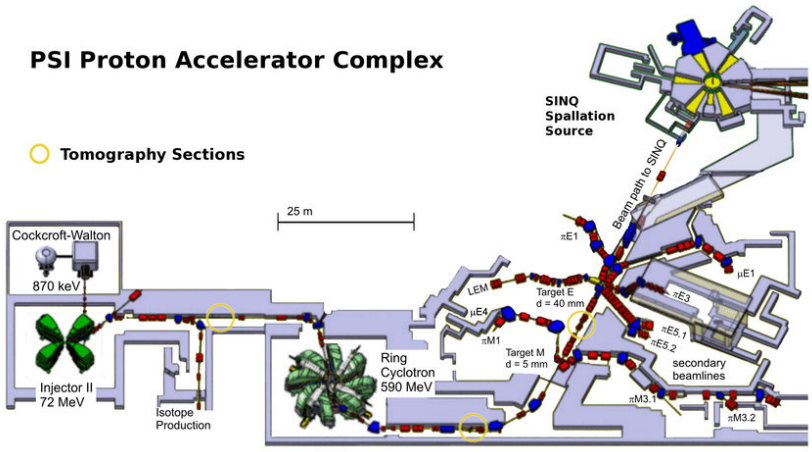

Figure 3.16: An overview of the PSI high-intensity proton accelerator complex [28].

3.3.2.1 Muon production

The first stage is the acceleration of protons, which is also performed in three steps. Protons from a hydrogen source are first accelerated up to 870 keV by a Cockcroft-Walton pre-accelerator shown in Fig. 3.17. The pre-accelerated protons are injected into an isochronous cyclotron called Injector II, which is equipped with two main radiofrequency (RF) cavities operating at ~ 400 kV, and two third-harmonic cavities operated at 30 kV [29]. This first cyclotron accelerates the proton up to 72 MeV and delivers 2.4 mA beam to the second cyclotron. The second cyclotron is the main cyclotron composed of four main RF cavities and eight magnets as shown in Fig. 3.18. The main cavities operate in a continuous wave mode at a frequency of 50.6 MHz and produce the final 590 MeV proton beam with a periodic 19.75 ns beam microstructure.

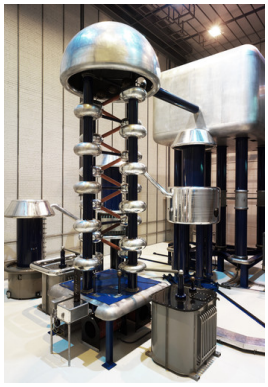

Figure 3.17: The Cockcroft-Walton pre-accelerator [30].

Figure 3.18: The 590 MeV ring cyclotron [30].

The second stage is the production of pions which are the source of muons. The accelerated proton beam is directed onto a 40 mm-thick graphite target called target E, after having passed through another 5 mm-thick target called target M. Here, protons impinging on the target produce Delta baryons, which then quickly decay into pions. These reactions can be written as below:

$$\begin{cases} p + p \to p + n + \pi^+ & \text{(3.9a)} \\ p + n \to n + n + \pi^+ & \text{(3.9b)} \\ p + p \to d + \pi^+. & \text{(3.9c)} \end{cases}$$

The third and last stage is the production of muons. The pions produced in the target subsequently produce muons via $\pi^+ \to \mu^+ \nu_\mu$ decay. Pions have a mean lifetime of $\sim 2.6 \times 10^{-8}$ s. The relatively long lifetime of pions enables the production of an effective DC muon beam from the originally-periodic proton beam.

3.3.2.2 Muon beam in the MEG II experiment

While there are several beamlines stretching from target E as shown in Fig. 3.16, the MEG II experiment will be conducted in the πE5 area, where the highest-intensity muon beam is available. The πE5 beamline utilizes surface muons [31], which means that they originate from pions stopped in a thin region from the target surface. Surface muons have momenta of ~ 28 MeV/c, and can be stopped in a very thin target, thus reducing unnecessary backgrounds.

These surface muons are delivered through a transport system to the muon stopping target in the MEG II detectors. The transport system consists of a first quadruple triplet magnet, a cross-field separator (Wien-filter), a second quadruple triplet magnet and a beam transport solenoid (BTS) as shown in Fig. 3.19. The magnets and the Wien-filter are capable of separating the muon beam from positron contaminations, and the BTS performs the final muon momentum adjustment. Thus, together with the muon stopping target to be explained in 3.3.3, a muon stopping rate of $7 \times 10^7\ \mu^+$/s is realized, which is more than twice that in the MEG experiment.

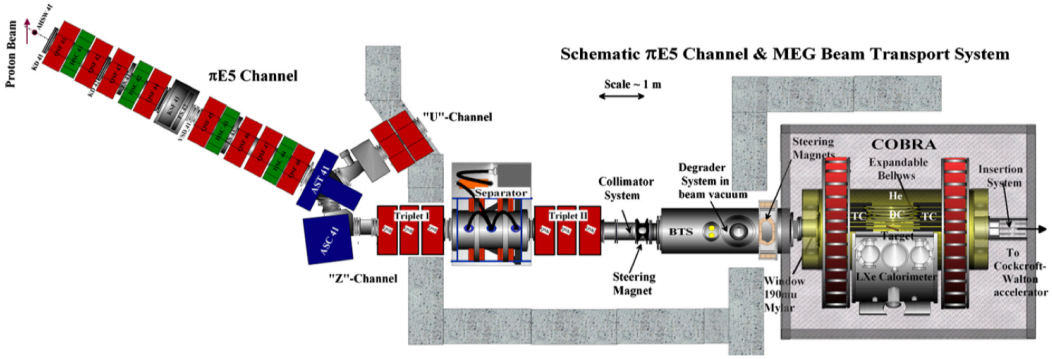

Figure 3.19: A schematic view of the πE5 channel and the beam transport system in the MEG II experiment [17].

3.3.3 Muon stopping target

The muon stopping target contains two contradictory requirements; one is to maximize the muon stopping rate, and the other is to reduce the target material in order to minimize the multiple scattering of emitted positrons and the production or background photons from positron bremsstrahlung or AIF. In the MEG II experiment, these requirements are realized by a 130 μm-thick scintillating polyvinyl toluene (PVT) foil shown in Fig. 3.20, which is capable of stopping $\sim 84\,\%$ of the muons. The use of a scintillating material also enables a monitoring of the beam intensity and profile by capturing the scintillation light with a CCD camera. It is placed at a slanting angle of 15° with respect to the beam to reduce the multiple scattering of positrons and the production of background photons.

In the MEG experiment, a severe deformation of the target foil was found, which could not be monitored. A lack of information on the precise target position and shape led to a significant systematic uncertainty in the positron angle measurement. This effect is expected to be compensated in the MEG II experiment by a photogrammetric monitoring of the dots printed on the target foil (see Fig. 3.20) by a CCD camera.

Figure 3.20: The muon stopping target in the MEG II experiment[27]. Optical markings are printed on the scintillator target.

3.3.4 Cylindrical drift chamber

In the MEG experiment, the efficiency and resolutions on the positron side was significantly worse than the designed values. This was mainly due to a low performance of the DCH as a positron tracker. The tracking inefficiency derived mainly from a track-matching inefficiency between the DCH and the TC, caused by the frontend electronics boards and the mechanical support of the DCH intercepting a large fraction of the positron tracks on their paths to the TC. The low position resolution arose from a generally-low amplitude of the induced signals on the cathodes, resulting in a poor z reconstruction. There were also some operational instabilities limiting the number of DCH planes during some of the data-taking periods.

To overcome these issues in the MEG II experiment, a completely-new, low-mass, single-volume, high-granularity, full-stereo cylindrical drift chamber was designed [32]. A picture of the constructed CDCH is shown in Fig. 3.21. It is composed of 11904 wires in total, the details of which are summarized in Tab. 3.3. The sense wires stretch over 9 layers. Each layer has a stereo angle ranging from $\sim 6°$ to $\sim 8°$ with two continuous layers having stereo angles of opposite signs. The drift cells are almost square, their size ranging from $\sim 6.6\,$mm in the most inner layer to $\sim 8.7\,$mm in the most outer layer. The whole chamber is filled with a low-density gas mixture of He and C_4H_{10} with the proportion of 90 : 10.

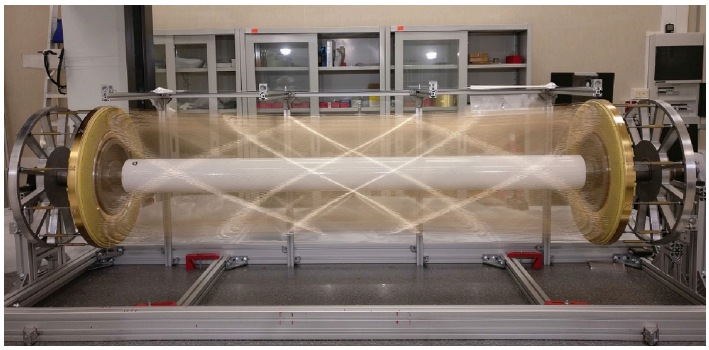

(a) An overview.

(b) An enlarged view of the endcap.

Figure 3.21: The MEG II CDCH [27].

Table 3.3: The wire configuration in the MEG II CDCH. The number of each wire is expressed as (number of wires per plane)×(number of planes).

Wire type	Diameter	Material	Number of wires
Sense wire	20 μm	Gold-plated W	$192 \times 9 = 1728$
Field wire (anode plane)	40 μm	Silver-plated Al	$192 \times 9 = 1728$
Field wire (cathode plane)	40 μm	Silver-plated Al	$384 \times 29 = 7680$
Guard wire	50 μm	Silver-plated Al	$192 \times 4 = 768$

The positron tracking inefficiency in the MEG experiment is solved by the use of single-volume chamber and eliminating any material between the CDCH and the pTC. The use of low-density gas also helps to reduce the multiple scattering of positrons and the generation of background photons; the equivalent radiation length per positron track turn is as small as $1.58 \times 10^{-3}\,X_0$. The highly-granular drift cell design enables operation in a high-rate environment whilst enhancing the position resolution in the positron tracking. The double readout of the wires with the techniques of time propagation difference and of charge division and the stereo configuration of the CDCH is expected to improve the z resolution considerably. Thus, the MEG II CDCH is expected to achieve the high efficiency and resolutions in Tab. 3.1 and Tab. 3.2.

3.3.5 Pixelated timing counter

The $t_{e^+\gamma}$ resolution in the MEG experiment was strictly limited by the positron time resolution, which was a factor of two worse than the designed value. This was partly due to a large uncertainty in the track length from the DCH, and partly due to a mediocre performance of the TC. The TC resolution was mainly limited by a large variation in the optical photon path lengths originating from the large scintillator size, and the degradation of PMT performance in the COBRA magnetic field.

Both these problems can be solved by the use of silicon photomultipliers (SiPMs); small silicon detectors with single-photon counting capability. The use of such small photo sensors enables us to utilize a highly-segmented scintillator design, which not only enhances the time resolution but also enables operation in a high-rate environment without

significant pileups. SiPMs are also known to be robust to magnetic fields, ensuring a stable performance of the detector over the data-taking periods.

A picture of the constructed MEG II pTC is shown in Fig. 3.23, in comparison to the MEG TC in Fig. 3.22. It is composed of 512 small ultra-fast scintillator tiles with SiPM readout on both ends. All the pixels are laid to be perpendicular to the signal positron track, so as to minimize multiple scattering. This highly-pixelated design of the detector realizes excellent time resolution below 40 ps by a multiple-pixel-hit scheme, and also provides efficient online positron time and position information for the signal triggering. The details of this detector will be discussed further in chapter 4.

Figure 3.22: The MEG TC [33].

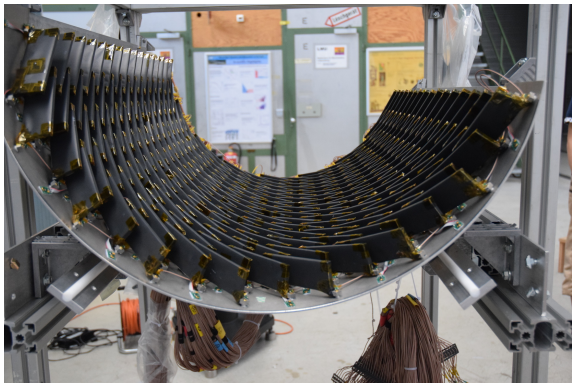

Figure 3.23: The MEG II pTC.

3.3.6 Liquid-xenon calorimeter

While the foreseen photon detection efficiency and position resolution were achieved in the MEG experiment, the achieved energy resolution was $\sim 40\,\%$ worse than the designed value. This led to twice the number of backgrounds (c.f. Eq. (3.8)), strongly limiting the physics reach of the MEG experiment. The low energy resolution was mainly due to a position dependence of the light collection efficiency caused by a non-uniformity of the PMT coverage, especially on the inner face.

The upgrade concept of the LXe calorimeter, therefore, is to eliminate this non-uniformity by replacing the inner 216 PMTs with smaller SiPMs, and also by modifying the layout of PMTs on the lateral faces [34]. Large-area multi-pixel photon counters (MPPCs), sensitive to vacuum-ultraviolet (VUV) scintillation light, was specially developed in corporation with Hamamatsu Photonics for this purpose [35]. The first upgrade point is depicted in Fig. 3.24, which shows the inner walls of the LXe calorimeter in the MEG and MEG II experiment, whilst Fig. 3.26 compares the event display for the same Monte-Carlo (MC) event. The highly-granular design clearly achieves an excellent position resolution of photons, and also a high energy resolution arising from the uniform readout. The second upgrade concept is depicted in Fig. 3.25, which illustrates a view of the detector in an r-z section. The inner face is extended, which reduces the energy leakage for events near the lateral walls and increases the detection efficiency by $\sim 10\,\%$.

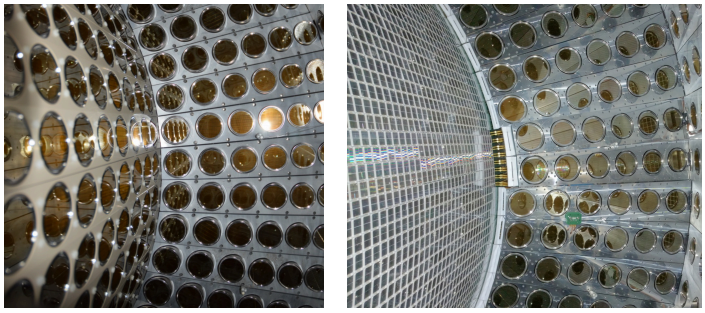

Figure 3.24: Inner walls of the LXe calorimeter in the MEG (left) and MEG II (right) detector.

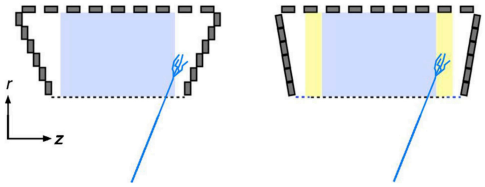

Figure 3.25: MEG (left) and MEG II (right) layout of the PMTs viewed in an r-z section [27].

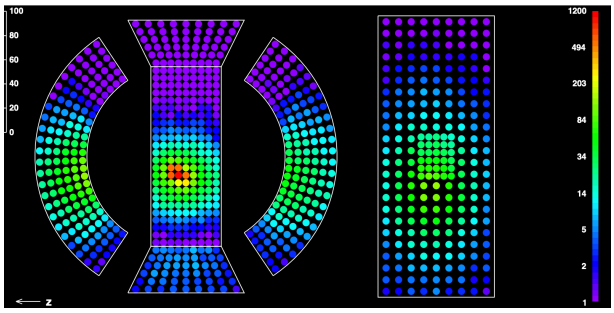

(a) Event display in the MEG LXe calorimeter

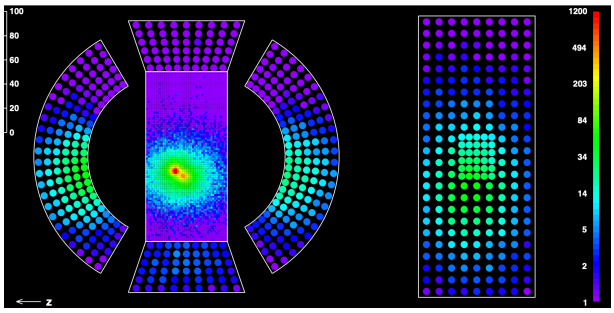

(b) Event display in the MEG II LXe detector

Figure 3.26: A comparison of the same MC event in the MEG and MEG II LXe calorimeter [27]. The capability of the new detector to distinguish different photons is depicted.

3.3.7 Radiative decay counter

3.3.7.1 Concept of RDC

The radiative decay counter (RDC) is an additional detector in the MEG II experiment. It is a unique detector solely for reducing the background, not by enhancing the resolution of the relevant physical quantities, but by identifying particular background events. Thanks to the low-density CDCH, the dominant background in the MEG II experiment is the accidental background whose photon comes from RMDs. A fraction of these events can be identified by tagging the low-energy positros from the RMDs. These positrons follow an almost helical trajectory with a small radius along the beamline. The RDC is placed on the beam axis and detects these low-energy positrons to identify accidental background events. In principle, the RDC can be placed both upstream and downstream of the target to maximize the identification of accidental background events. Fig. 3.27 shows a schematic view of the identification of an accidental background event with the downstream RDC (DS-RDC).

There are two potential observables to distinguish an accidental RMD event with the RDC; one is the positron time with respect to the photon detected in the LXe calorimeter, and the other is the positron energy. The helical trajectory paths of low-energy RMD positrons differ little event by event, yielding an almost fixed positron time with respect to the RMD photon detected in the LXe calorimeter. As background Michel positrons

have a random time distribution, this time difference can be used to identify accidental RMD events. This is depicted in Fig. 3.28. In addition, as the RDC detects low-energy RMD positrons, the energy information can also be used to distinguish them from the relatively high-energy Michel positrons.

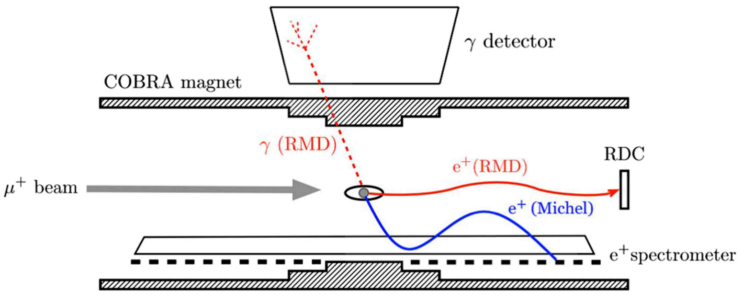

Figure 3.27: A schematic view of the identification of an accidental background event with the DS-RDC [27].

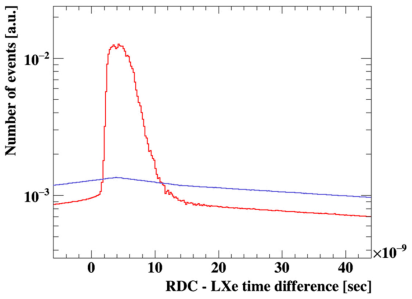

Figure 3.28: Simulated time differences between the positron detection in the RDC and the photon detection in the LXe calorimeter for accidental background events (red) and signal events(blue) [27].

3.3.7.2 Downstream RDC

The downstream RDC (DS-RDC) has already been designed and developed. It consists of two parts; a timing detector in front for the positron timing measurement, and a calorimeter attached to its back for the positron energy measurement. Both must have pixelated designs to cope with pileups.

The timing detector is composed of 12 differently-sized plastic scintillators (BC-418 from Saint-Gobain [36]) with SiPM (MPPC S13360-3050PE from Hamamatsu Photonics [37]) readout; its design is shown in Fig. 3.29. The use of fast plastic scintillators realizes a high time resolution, whilst the use of SiPMs enables operation in the COBRA magnetic field.

The calorimeter, on the other hand, is made of 76 LYSO crystals (from Shanghai Institute of Ceramics) with SiPM (MPPC S12572-025 from Hamamatsu Photonics [38]) readout; its design is shown in Fig. 3.30. LYSO crystals with a high light yield and a short decay constant are suitable for the positron energy measurement in a high-rate environment. LYSO also has intrinsic radioactivity, which can be used for a self energy calibration. Again, the use of SiPMs enables operation in the COBRA magnetic field.

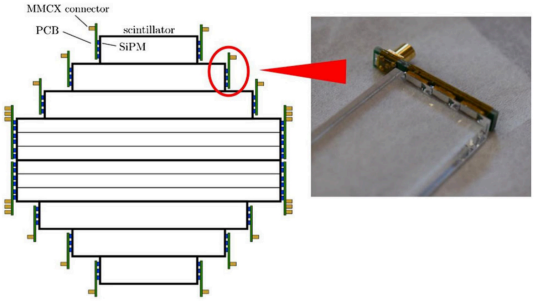

Figure 3.29: The design of the timing detector of the DS-RDC [27].

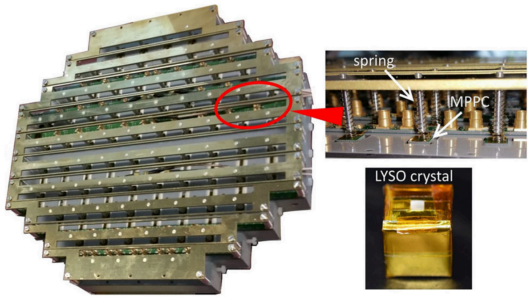

Figure 3.30: The calorimeter of the DS-RDC [27]. SiPMs are attached to LYSO crystals with springs.

3.3.7.3 Upstream RDC

While the DS-RDC distinguishes accidental background events from both the positron time and energy, the energy information is not available for the upstream RDC (US-RDC), as it must not degrade the muon beam energy. Therefore, the US-RDC must be capable of identifying background events from the positron timing measurement alone, and it must also be of little material so as not to affect the beam. Other harsh requirements also exist, such as radiation hardness of the detector, and a high time resolution to distinguish RMD positron signals immersed in the muon beam background.

Various detectors have already been tested, such as scintillating fibers, a diamond detector, a silicon detector, etc., but none satisfied all the necessary requirements. A gas detector is now being developed as a promising candidate [39]. It is a resistive plate chamber (RPC) with multi layers; its design is schematically shown in Fig. 3.31. A single-layer RPC consists of two highly-resistive plates, charged positive and negative respectively, separated by a gas volume. Charged particles are detected by the amplification of the ionized electron in the electric gaseous field. The use of diamond-like carbon (DLC) for resistive plates, can localize the electrical discharge, enabling high-rate detection of particles. The multi-layer structure can enhance the time resolution by reducing the thickness of each layer, while maintaining a high overall efficiency [40].

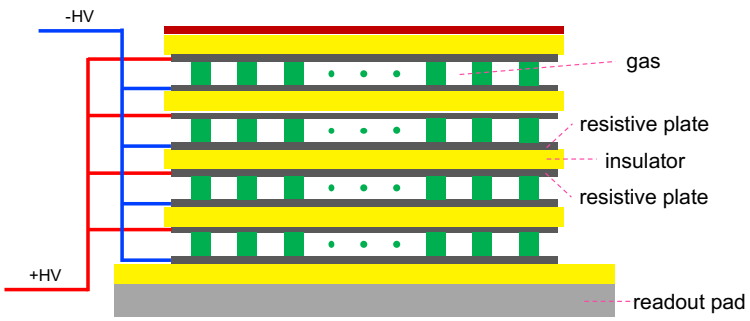

Figure 3.31: A schematic view of a multi-layer RPC.

3.3.8 Trigger and DAQ

The MEG II detectors meet the requirement to operate at a high-rate environment generally by a finer readout or a segmented design of the detectors. This has led to an almost tripling of the readout channels with respect to the MEG experiment, whilst an efficient offline pileup reconstruction and rejection requires the availability of raw waveforms. Thus, the DAQ waveform digitizer has to provide state-of-the-art time and charge resolution and a sampling speed in the GSPS range.

In addition, the general replacement of PMTs with SiPMs require electronic signal amplification as SiPMs have a lower internal gain compared to PMTs. The use of SiPMs in LXe prevents us from placing preamplifiers next to the SiPMs due to cooling problems. Thus, the new electronics must also incorporate a flexible amplification scheme for small signals.

3.3.8.1 WaveDREAM board

The requirements for the electronics are met by the development of WaveDREAM boards (WDBs) [41]. A WDB has the functionalities of DAQ, basic trigger, high voltage (HV) application and signal amplification all integrated into a single compact board. Fig. 3.32 shows a schematic view of the WDB. It contains an amplifier capable of amplification in the range from 0.5 to 100, as well as a waveform shaper through a programmable pole-zero cancellation. One WDB incorporates two DRS4 chips, which digitize the waveform with a maximum sampling speed of 5 GSPS. The DRS4 chips are connected to analog-to-digital converters (ADCs), which transmit the signal to a field-programmable gate array (FPGA) capable of treating trigger algorithms. The HVs for SiPMs can also be generated in the WDB by a Cockcroft-Walton (CW) voltage multiplier. A simple 5 V digital-to-analog converter (DAC) is mounted to apply different HV to each channel with a high precision.

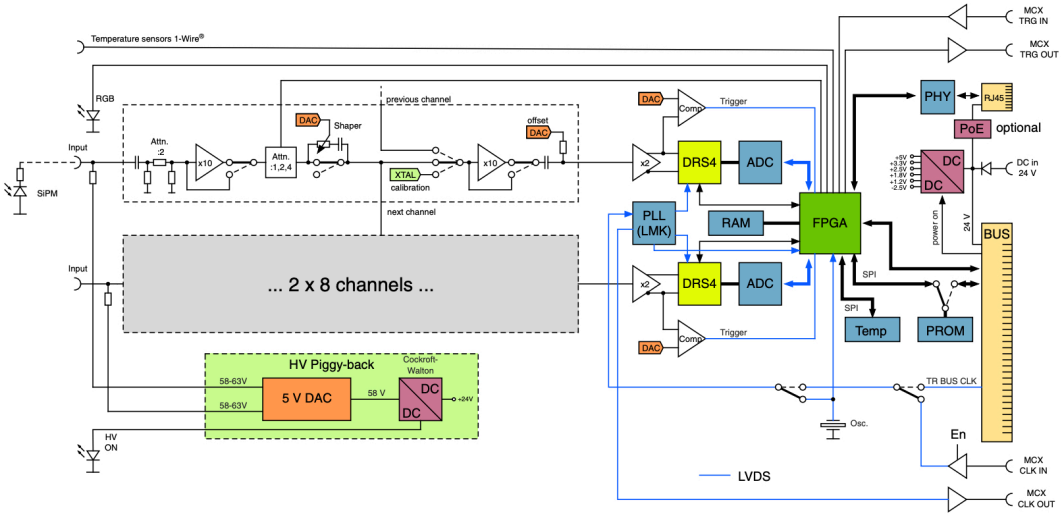

Figure 3.32: A schematic view of the WDB [27].

16 of these WDBs, each containing 16 channels, can be stored in a WaveDAQ crate,

together with a crate management board (CMB), a data concentrator board (DCB) and a trigger concentrator board (TCB). A picture of a single WDB and a sketch of the WaveDAQ crate are shown in Fig. 3.33 and Fig. 3.34 respectively. CMBs supply power to all the boards in the crate, and also manage the slow control system. DCBs are responsible for the configuration of all boards inside the crate, the distribution of the master clock and the trigger signals, the readout of waveform data, and the interface to the global DAQ computers. TCBs are in charge of online data processing for triggering, which gather information from lower level trigger boards to perform online reconstruction of the decay product observables. The trigger in the MEG II experiment will be discussed in more detail in 3.3.8.2.

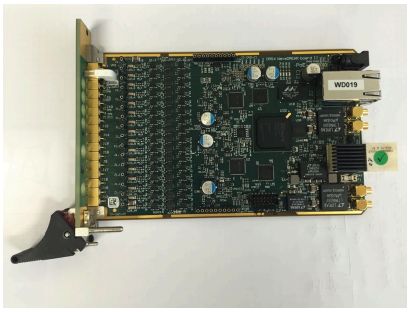

Figure 3.33: A WDB without a HV module [41].

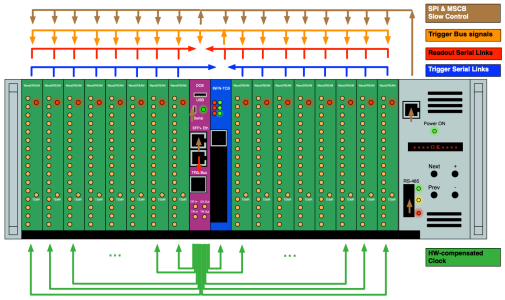

Figure 3.34: A sketch of a WaveDAQ crate with 16 WDBs (green), a DCB (magenta), a TCB (blue) and a CMB on the right [41].

3.3.8.2 Trigger

The trigger in the MEG II experiment is required to collect $\mu^+ \to e\gamma$-like events with a high efficiency by suppressing the backgrounds by almost six orders of magnitude, resulting in an DAQ rate of 10 Hz. This also leads to a substantial reduction in the data size. The slow response of the CDCH makes it impossible to use its information for online triggering. Therefore, the reconstructed information from the pTC on the positron side and the LXe calorimeter on the photon side are used for the online triggering. Hence, the observables used for the online triggering are E_γ, $t_{e^+\gamma}$ and $\theta_{e^+\gamma}$.

E_γ is reconstructed online by summing the amplitudes of MPPC signals and PMT signals, after having corrected for the gain, the quantum efficiency (QE), etc. of each photo sensor. An event is triggered when the reconstructed E_γ is above a certain threshold.

$t_{e^+\gamma}$ is reconstructed from the online time of the LXe calorimeter and the pTC, which are extracted by sampling the WDB discriminator output at 800 MHz and intercepting the first sample over the threshold. The positron detection time is extracted from a single pixel placed at the most inner z of all hit pixels. However, the unavailability of the positron track information from the CDCH at trigger level makes the correction of the propagation time from the target difficult. An estimation of the positron time of flight (TOF) can be made from the correlation between the triggered pixel ID and the TOF (see Fig. 3.35), but this depends on the number of positron turns, so the trigger time window must be kept relatively wide.

Lastly, $\theta_{e^+\gamma}$ direction match is performed by using a lookup table (LUT). Grouping 4×4 MPPCs in the LXe calorimeter as a single patch, the ID of the patch with the

highest signal has a strong correlation with the pixel ID of the first hit pTC pixel for signal events as shown in Fig. 3.36. This information is summarized in the online LUT, to which the trigger can refer in order to estimate $\theta_{e^+\gamma}$.

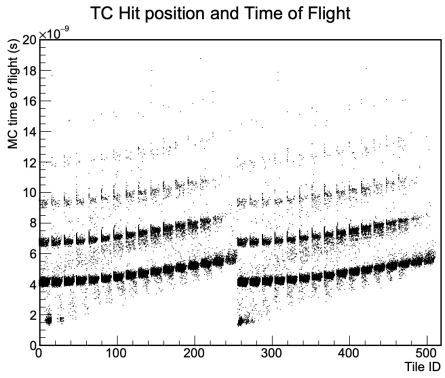

Figure 3.35: The TOF of positrons as a function of pTC pixel ID [42]. A clear correlation between the TOF and number of turns is seen.

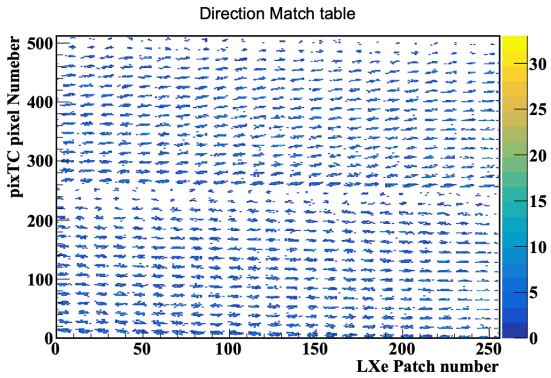

Figure 3.36: The LUT used for the $\theta_{e^+\gamma}$ direction matching [42].

Chapter 4

Pixelated Timing Counter

The MEG II pTC provides the precise decay time of muons and efficient trigger information on the positron side. In this chapter is described the concept and the design of the pTC to satisfy these requirements, along with its basic operation, analysis and calibration procedures. In the end, the remaining tasks concerning the pTC towards the physics run are introduced.

4.1 Concept

4.1.1 Requirements

The role of the pTC in the MEG II experiment is to reduce the number of background events by a precise reconstruction of the decay time of muons and to provide efficient trigger information on the positron side. Therefore, the parameters that must be maximized are as follows:

- The positron time resolution at the vertex point, $\sigma_{t_{e^+}}$.
- The positron tracking efficiency ϵ_{e^+}.
- The online positron time and emission angle resolution.

The $t_{e^+\gamma}$ resolution at the vertex point is given by

$$\begin{aligned}\sigma_{t_{e^+\gamma}} &= \sqrt{(\sigma_{t_{e^+}})^2 + (\sigma_{t_\gamma})^2} \\ &= \sqrt{\left((\frac{\sigma^{\mathrm{CDCH}}_{l_{e^+}}}{c})^2 + (\sigma^{\mathrm{pTC}}_{t_{e^+}})^2\right) + (\sigma_{t_\gamma})^2}\end{aligned} \tag{4.1}$$

where $\sigma_{t_{e^+}}$ is the positron time resolution, σ_{t_γ} is the photon time resolution, $\sigma^{\mathrm{CDCH}}_{l_{e^+}}$ is the CDCH positron track length uncertainty, c is the speed of light, and $\sigma^{\mathrm{pTC}}_{t_{e^+}}$ is the pTC positron time resolution. The photon time resolution using the LXe calorimeter is expected to be 50–70 ps from MC studies. Adopting a conservative value of $\sigma_{t_\gamma} \sim 70$ ps and considering the contribution from the CDCH track length uncertainty, $\sigma^{\mathrm{CDCH}}_{l_{e^+}}/c \sim 6$ ps, in order to achieve the expected $t_{e^+\gamma}$ resolution of 84 ps at the vertex (c.f. Tab. 3.2), the required pTC positron time resolution is calculated to be ~ 46 ps.

In addition, to achieve one order higher sensitivity than the MEG experiment, a realistic goal for the tracking efficiency is $\epsilon_{e^+} \geq 70\,\%$. The MEG II pTC is also required to be tolerant to a high-rate condition with the planned beam intensity increase.

4.1.2 Upgrade concept

The MEG TC together with the DCH tried to achieve lower but similar goals, but resulted in an unexpectedly poor result as summarized in Tab. 3.1 and Tab. 3.2. The low positron tracking efficiency was due to the material between the DCH and the TC, while the time resolution was strictly limited by the large scintillator size, the PMT performance degradation in the COBRA magnetic field, poor time calibration between scintillator bars, and pileup effects.

The MEG II pTC overcomes such limitations by a highly-segmented detector design. The 30 plastic scintillator bars of the MEG TC are replaced by 512 smaller scintillator tiles in the new configuration, which is made possible by the use of SiPMs as photo sensors. This new design of the pTC has various advantages over the previous one:

- A high single-pixel time resolution can be achieved for the small scintillator size.
- The multiple-pixel-hit scheme significantly improves the overall time resolution.
- A high online emission angle resolution can be achieved for its segmented design.
- A flexible detector layout enables maximization of the detection and tracking efficiencies.
- A stable detector performance is possible as SiPMs are unaffected by magnetic fields.
- Pileup becomes negligible due to the segmented design.

The most important point of these, concerning the pTC resolution, is the second point; the multiple-pixel-hit scheme (c.f. 4.5.1). The new design allows signal positrons to hit an average of ~ 9 pTC pixels as shown in Fig. 4.1. As the timing measurement in each pixel is independent of each other, in principle, the overall resolution should improve with $1/\sqrt{N_{\mathrm{hit}}}$, with the number of hit pixels, N_{hit}. This multiple-pixel-hit scheme significantly improves the pTC time resolution from the single-pixel time resolution, and the overall resolution goal of 46 ps is expected to be achieved.

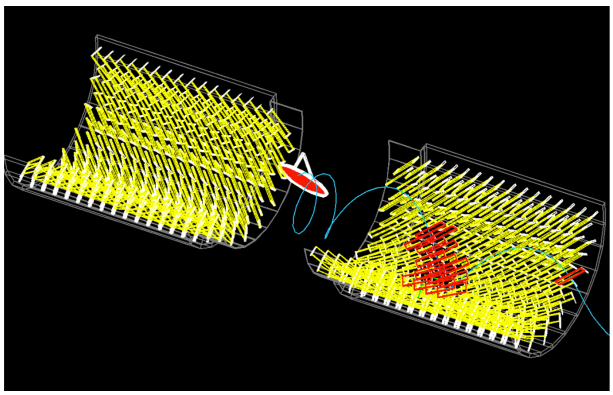

Figure 4.1: An example of a hit pattern by a simulated signal positron.

On the other hand, the most important point, concerning the positron efficiency is the third point. No material is placed between the CDCH and the pTC, and the pTC is placed just below the CDCH to allow positrons to be tracked up to just before the pTC. Hence, the efficiency goal of 70 % is also expected to be made possible with a suitable tracking algorithm.

4.2 Design

4.2.1 Overall design

The pTC consists of two semi-cylindrical super-modules, which are mirror-symmetric to each other and placed both upstream (US) and downstream (DS) of the target between the CDCH and the COBRA. Fig. 4.2 shows the design of the DS super-module. Each super-module is composed of 256 scintillation counters (or pixels) described in 4.2.2; 16 pixels align in z direction at 5.5 cm intervals, while 16 lines are cylindrically arranged at 10.3° intervals, alternately staggered by half a pixel. All the pixels are tilted at 45° to be perpendicular to the signal positron trajectories. This overall design covers $23.0\,\text{cm} < |z| < 116.7\,\text{cm}$ in the longitudinal direction and $-165.8° < \phi < 5.2°$ in the azimuthal direction, which fully covers the signal positron acceptance when the photon points to the LXe calorimeter.

The signals are read out through the backplanes (BPs); 32 BPs align in ϕ direction in each super-module, and a common BP is used for channels in the same ϕ. All the pixels are fixed onto these BPs, which lead the signals from SiPMs to higher $|z|$ and allow them to be read out through coaxial cables (RG-178 from Radiall [43]) and by the WDBs. This is shown in Fig. 4.3.

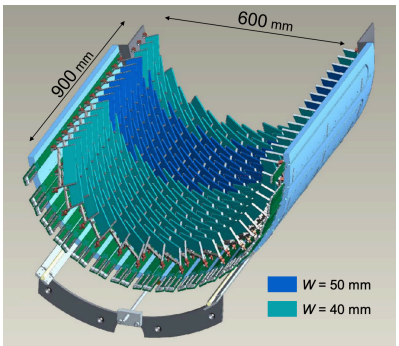

Figure 4.2: CAD design of the DS pTC super-module [27].

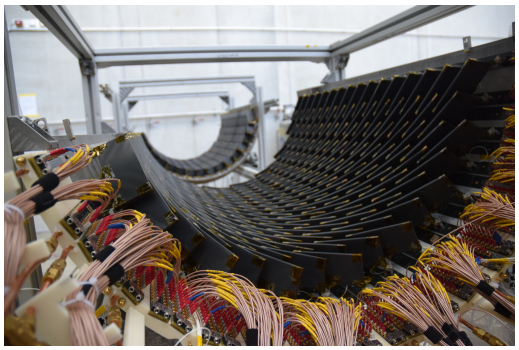

Figure 4.3: The pTC with cables prolonged from the BPs.

4.2.2 Single-pixel design

A single pixel is composed of a plastic scintillator with six series-connected SiPMs at both sides as shown in Fig. 4.4. The scintillation light produced by a charged particle penetrating the scintillator is detected by the SiPMs on both sides. The SiPMs are soldered onto specially-made print circuit boards (PCBs), and are glued to the scintillator using optical cement (BC600). Some pixels have a hole and a support structure at the

bottom to insert an optical fiber used for time calibration between pixels (see 4.4.3). The scintillator is wrapped with a reflective film (ESR from 3M), and afterwards with a polyvinyl fluoride film (Tedlar® [44]) together with the support structure for light shielding. A list of materials used for the pTC pixel assembly is shown in Tab. 4.1.

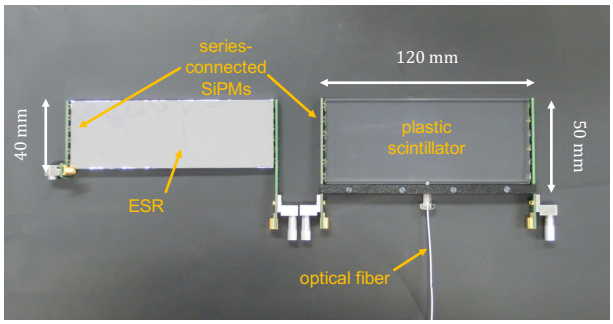

Figure 4.4: Single pTC pixels. One (left) is wrapped with an ESR, while the other (right) has an optical fiber inserted.

Table 4.1: Major materials used for pTC pixel assembly.

Material	Product	Manufacturer	Reference
Scintillator	BC-422 [36]	Saint-Gobain	[36]
SiPM	ASD-NUV3S-P High-Gain	AdvanSiD	
Reflector	ESR	3M	
Light shielder	Tedlar®	DuPont	[44]

4.2.2.1 Plastic scintillator

The main requirements for the scintillator material are a high light yield and a fast time response to achieve a high pixel time resolution. Thus, ultra-fast plastic scintillators, BC-422 from Saint-Gobain [36], are chosen. All the scintillator tiles have the same length ($L = 120\,\text{mm}$) and thickness ($T = 5\,\text{mm}$), while the width is either $W = 40\,\text{mm}$ or $W = 50\,\text{mm}$ depending on where the pixel is placed as already shown in Fig.4.2. Although there are some geometrical restrictions, the size of the pixels are generally optimized to maximize the acceptance and the resolution.

4.2.2.2 The principle of SiPMs

SiPMs are photo sensors made up of multi-pixel avalanche photodiodes (APDs) working in Geiger modes. By applying a reverse bias voltage, charge carriers generated by the absorption of photons are accelerated, trigger avalanches in the gain region, and thus multiply the signal. Fig. 4.5 shows a schematic view of the structure and the working principle of SiPMs.

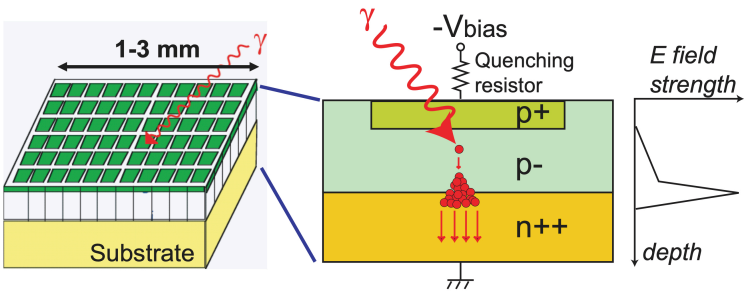

Figure 4.5: Schematic view of how a SiPM works [45].

Here, some basic parameters which characterize SiPMs are introduced.

- **Breakdown voltage and overvoltage**

  A SiPM needs a certain magnitude of reverse bias voltage for the produced charge carriers to cause an avalanche. This voltage is called the breakdown voltage and a SiPM must be operated above this voltage. The operational characteristic of SiPMs are determined by the overvoltage defined as

  $$V_{\text{ov}} = V - V_{\text{bd}} \tag{4.2}$$

  where V is the applied bias voltage and V_{bd} is the breakdown voltage. The breakdown voltage of SiPMs is known to have a strong dependence on the temperature.

- **Gain**

  SiPMs have high gains in the range of $\sim 10^5$–10^6. It is defined by the output charge from a single photoelectron and is known to be proportional to the overvoltage as

  $$G = \frac{Q}{q} \propto V_{\text{ov}} \tag{4.3}$$

  where G is the gain, Q is the output charge from an electron, and q is the electron charge.

- **Photon detection efficiency**

  The photon detection efficiency (PDE) is the probability of a photon entering the SiPM to cause an avalanche. This factor has a positive correlation with the overvoltage.

- **Dark noise**

  A dark pulse is a pulse generated not by a photon, but by the thermal excitation of an electron or via tunneling effect. This is quantize by the dark count rate (DCR), which is the number of dark pulses in a second. The dark noise a generic term for the SiPM noise from pulses that are not generated by photons. This dark noise is known to have a strong correlation with the overvoltage and the temperature. In addition, radiation damage to SiPMs can significantly increase the amount of dark noise as later explained (see 4.7.1).

- **Crosstalk**

  A crosstalk (CT) is caused when accelerated carriers in the high field region emit photons, which initiate a secondary avalanche in a neighboring microcell. A CT occurs in correlation with another pulse, and is therefore called a correlated noise. The CT probability increases with the overvoltage.

- **Afterpulse**

  An afterpulse (AP) is another type of the correlated noise. It occurs when charge carriers get trapped in crystal defects during an avalanche, and cause a delayed avalanche. Delayed CTs can also cause afterpulsing. The AP probability also increases with the overvoltage.

4.2.2.3 SiPMs in the pTC

The time resolution of scintillation counters strongly depend on the photon statistics. Higher photon statistics can be obtained either by increasing the SiPM coverage of the scintillator, or by using SiPMs with higher PDE. After testing various combinations of SiPMs, the combination of six 3 mm × 3 mm ASD-NUV3S-P SiPMs from AdvanSiD was chosen. The AdvanSiD SiPMs used for the pTC can be classified into three types according to when they were manufactured. This is summarized in Tab. 4.2. Type I SiPMs are used in most pixels, but ∼ 40 pixels consist of type II SiPMs. Type III SiPMs are newly used for the spare pixels introduced in chapter 6.

Table 4.2: SiPMs used for the pTC.

Type	SiPM	Cell size
I	ASD-NUV3S-P High-Gain	50μm × 50 μm
II	ASD-NUV3S-P	50μm × 50 μm
III	ASD-NUV3S-P [46]	40μm × 40 μm

These SiPMs can be connected either in parallel or in series. It was found that parallel connection of SiPMs can increase the signal rise time and the width, leading to a degradation in the time resolution, while a sharper pulse can be obtained using series connection [47]. This arises from the small capacitance in the series connection. These results are depicted in Fig. 4.6 and Fig. 4.7.

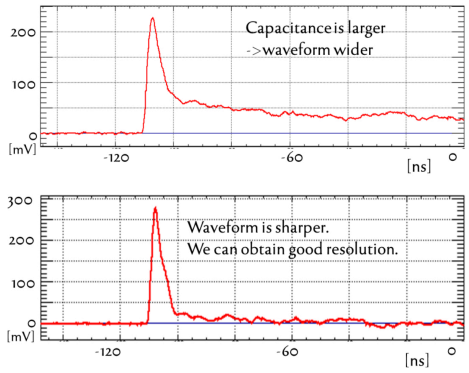

Figure 4.6: Waveforms obtained using parallel connection (top) and series connection (bottom) of SiPMs[47]. The waveforms are shaped using pole-zero cancellation.

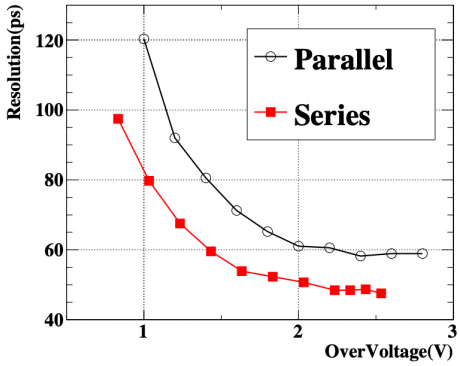

Figure 4.7: A comparison of the overvoltage dependence of the time resolution using parallel and series connection of SiPMs [47].

4.3 Analysis

Fig. 4.8 shows the reconstruction procedure of positrons. On the pTC side, first, an analysis of the waveforms obtained by the WDBs is performed. Second, pixel hits are reconstructed from the two channels in each pixel. Third, the hits which belong to the same positron track are grouped together into a cluster; this procedure is called the clustering. Fourth, the hits in the same cluster are combined into a single positron track. Finally, a matching between the pTC track and the CDCH track is performed to create one final positron track, and the positron momentum, time and emission angle are reconstructed. Methods for matching the pTC and the CDCH information are still under development, so I introduce the analysis procedures from the waveform analysis to the pTC tracking in this section. One thing to note is that the pTC tracking requires a certain minimum number of hits. When the number of the pTC hits is below this threshold, the pTC tracking is skipped and the pTC cluster information and the CDCH track information are combined.

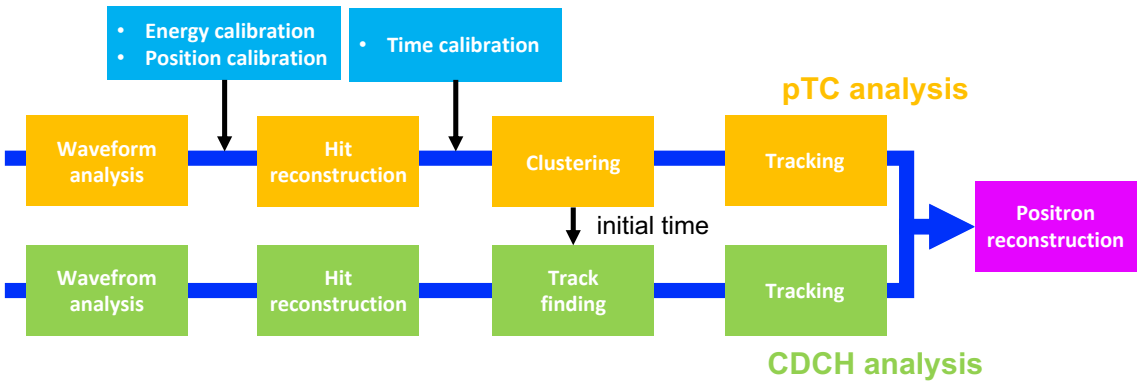

Figure 4.8: The analysis flow of the positron reconstruction.

4.3.1 Waveform analysis

To obtain the signal arrival time from the waveform, the constant fraction (CF) method is used, in which the time the waveform reaches a certain fraction of the peak point is extracted. Setting a fixed threshold can potentially cause time walks depending on the signal size, but this method always yields the same time as long as the waveform characteristic does not change. Hence, a better time resolution can be obtained using this method.

4.3.2 Hit reconstruction

The pixel hit time, t_{hit}, and the horizontal hit position, x_{hit}, are reconstructed in the hit reconstruction stage. The local coordinates in a pixel are defined in Fig.4.9.

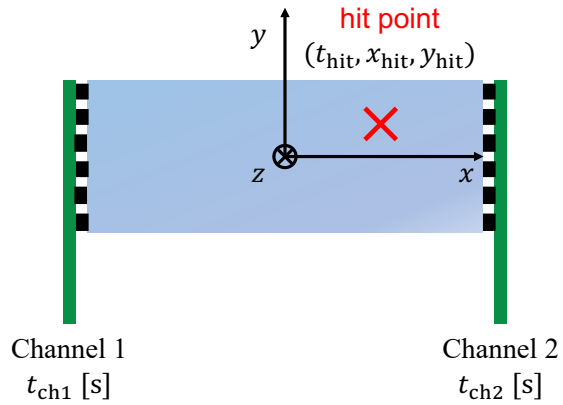

Figure 4.9: Definition of the local coordinates in a pixel.

4.3.2.1 Hit time

The time we measure with the two channels deviate from the true pixel hit time by the propagation time of the scintillation light to each channel, plus some time offset intrinsic to each channel. Thus, the two measured times can be written as

$$t_{\text{ch1}} = t_{\text{hit}} + \Delta t_{\text{ch1}} + (t_{\text{offset}} - \frac{\delta t}{2}) \tag{4.4}$$

$$t_{\text{ch2}} = t_{\text{hit}} + \Delta t_{\text{ch2}} + (t_{\text{offset}} + \frac{\delta t}{2}) \tag{4.5}$$

where the subscripts ch1 and ch2 correspond to the two readout channels, t_{hit} is the true pixel hit time, Δt is the propagation time of the scintillation light to each channel, t_{offset} is the intrinsic pixel time offset, and δt satisfies $\delta t = t_{\text{ch2}} - t_{\text{ch1}}$ when $x_{\text{hit}} = 0$. The intrinsic time offset of each channel is incorporated in $t_{\text{offset}} \mp \frac{\delta t}{2}$.

From Eq. (4.4) and Eq. (4.5), the hit time can be reconstructed as

$$\begin{aligned} t_{\text{hit}} &= \frac{t_{\text{ch1}} + t_{\text{ch2}}}{2} - \frac{\Delta t_{\text{ch1}} + \Delta t_{\text{ch2}}}{2} - t_{\text{offset}} \\ &= \frac{t_{\text{ch1}} + t_{\text{ch2}}}{2} - \frac{L}{2v_{\text{eff}}} - t_{\text{offset}} \end{aligned} \tag{4.6}$$

where $L(= 12\,\mathrm{cm})$ is the length of a pixel, and v_{eff} is the effective velocity of the scintillation light, which is assumed to be uniform throughout each pixel. In truth, $L/2v_{\mathrm{eff}} + t_{\mathrm{offset}}$ is obtained beforehand in the time calibration between pixels (see 4.4.3). Therefore, we do not actually have to consider the propagation time of the scintillation light in the hit time reconstruction, but obtain consistent hit times independent of x_{hit}.

4.3.2.2 Hit position

The horizontal hit position in a pixel can be obtained by the time difference of the two channels. The propagation time of the scintillation light to each channel can be written as

$$\Delta t_{\mathrm{ch1}} = \frac{\frac{L}{2} + x_{\mathrm{hit}}}{2} \tag{4.7}$$

$$\Delta t_{\mathrm{ch2}} = \frac{\frac{L}{2} - x_{\mathrm{hit}}}{2}. \tag{4.8}$$

By taking the difference between Eq. (4.7) and Eq. (4.8) and using Eq. (4.4) and Eq. (4.5), the hit position can be obtained as

$$\begin{aligned} x_{\mathrm{hit}} &= \frac{(\Delta t_{\mathrm{ch1}} - \Delta t_{\mathrm{ch2}})}{2} v_{\mathrm{eff}} \\ &= \frac{t_{\mathrm{ch1}} - t_{\mathrm{ch2}} + \delta t}{2} v_{\mathrm{eff}}. \end{aligned} \tag{4.9}$$

The effective velocity of the scintillation light in each pixel, v_{eff}, and the relative time offset of the two channels, δt, must, therefore, be obtained beforehand. These are obtained in the position calibration (see 4.4.2).

4.3.3 Clustering

In the clustering process, the reconstructed hits belonging to the same positron track are grouped together. To do this, an index called the geometry ID is defined as in Fig. 4.10 according to the order the positron track penetrates. Using this, each pixel hit time and x hit position are projected to the pixel with the youngest geometry ID (i.e. the assumed first-hit pixel). A typical TOF between adjacent pixels is used for the former projection, and a typical positron penetration angle is used for the latter. Thus, the hits with close projected hit times and projected hit positions are grouped together into a single cluster.

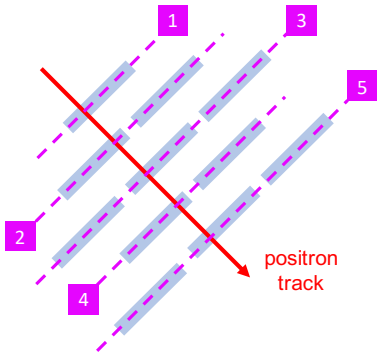

Figure 4.10: Definition of the geometry ID for clustering.

4.3.4 Tracking

The last stage of the pTC analysis is the reconstruction of a track from the hits in the same cluster. This procedure can be divided into two steps; the former is the estimation of the initial values for the track fit, and the latter is the actual track fit with the estimated parameters.

4.3.4.1 Parameter estimation

In order to colligate the hits into a single track, an estimation of a couple of quantities must be made in advance. First, a reasonable initial value of the positron momentum is needed, as it largely affects the positron trajectory. However, the positron acceptance of the pTC is strictly limited to those with momentum close to the signal positron; positrons with low momentum seldom reach the pTC due to the COBRA magnetic field. Therefore, a typical value of 45 MeV is sufficient as the initial value.

Another necessary parameter is the local y position in each pixel hit. x_{hit} is already estimated with $\sim 11\,\mathrm{mm}$ precision in the hit reconstruction as explained in 4.3.2.2. z_{hit} does not need to be estimated as each pixel is only 5 mm thick, and the mean value of 2.5 mm can be used. In some way y_{hit} must also be estimated to create a track.

This is realized by making use of the hit pattern in a cluster. The "hit" or "non-hit" in n pixels with consecutive geometry IDs can be converted into an n-bit information. In this way, all the cluster hit patterns can be listed up. Using MC simulation to obtain the averaged true y hit position for each hit in each cluster hit pattern, y_{hit} can be estimated with $\sim 8\,\mathrm{mm}$ precision. In truth, the hit pattern of five pixels in front and back of the pixel under estimation is used to estimate y_{hit}. This method is schematically depicted in Fig. 4.11.

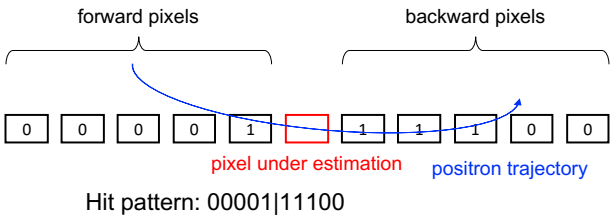

Figure 4.11: A schematic diagram of y_{hit} estimation from the cluster hit pattern.

4.3.4.2 Tracking

The pTC positron track is reconstructed using the Kalman Filter (KF) technique. Fig. 4.12 shows a schematic view of how the KF works. It is an efficient recursive algorithm to estimate the state vector and its covariance matrix based on the previous states, and can be used to estimate time-changing variables from discrete values with errors. In other words, the KF technique enables us to choose the most likely track from all the possible tracks, taking into account of the hit position error of each hit. In addition to the KF technique, an algorithm called the Deterministic Annealing Filter (DAF) is implemented, which is an extension of the KF and allows us to exclude any outlier hits from the track.

Fig. 4.13 shows a graphic view of a reconstructed positron track in a MC event using the pTC tracking. You can see how the KF technique creates a continuous track from the discrete hit information. A GENFIT package is used for the calculation.

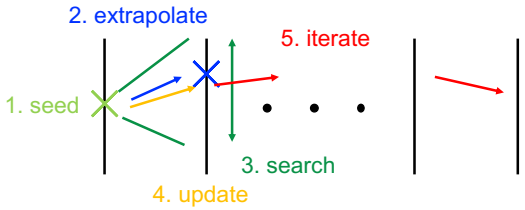

Figure 4.12: A schematic diagram of the principle of the KF.

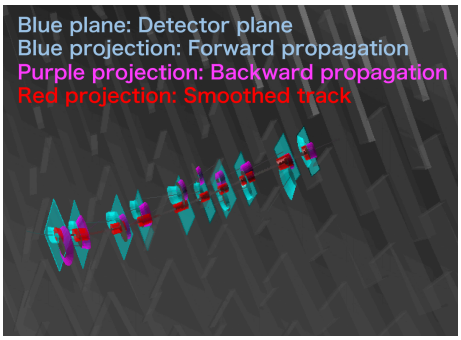

Figure 4.13: A graphic view of a reconstructed pTC track [48].

4.4 Calibration

There are various quantities that must be calibrated to analyze the pTC data. Here I briefly introduce some of them which are relevant to the coming discussions.

4.4.1 Energy calibration

The energy deposited in a pixel by a positron is reconstructed from the pulse charge. In the waveform analysis, the collected charge is calculated by the integration of the waveform. The charge-to-energy conversion factor can then be obtained by fitting the

reconstructed charge distribution to the energy deposit distribution obtained using MC simulation. To be more specific, the energy calibration factor C_E is obtained as

$$C_E = \frac{E^{\text{peak}}}{\sqrt{Q_{\text{ch1}}^{\text{peak}} \cdot Q_{\text{ch2}}^{\text{peak}}}}^{1} \tag{4.10}$$

where E^{peak} is the peak in the MC energy deposit distribution, and $Q_{\text{ch1}}^{\text{peak}}$ and $Q_{\text{ch2}}^{\text{peak}}$ are the peaks of the reconstructed charge in the two channels. This conversion factor is obtained for each pixel and retained for the analysis.

4.4.2 Position calibration

In order to reconstruct the hit position in each pixel as explained in 4.3.2.2, the relative time offset of the two channels and the effective velocity of the scintillation light must be calibrated. To do this, the reconstructed hit position distribution in each pixel as shown in Fig. 4.14 is used. The horizontal length essentially demonstrates the effective light velocity, while the center position of the distribution shows the time offset between the two channels. The x_{hit} position resolution of each pixel can also be obtained from the standard deviation of the convoluted Gaussian.

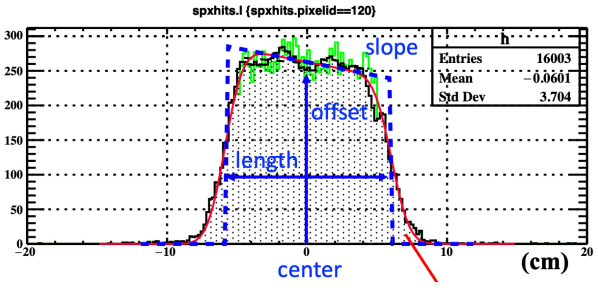

Figure 4.14: An example of the reconstructed x_{hit} distribution in a pixel. The black histogram shows the position distribution after taking the moving average from the original distribution(green). This is fitted with a Gaussian-convoluted trapezoid (red) [49].

4.4.3 Time calibration

The MEG TC performance was partly limited by the inaccuracy of the time calibration between the TC bars. A more precise inter-pixel time calibration is required for the MEG II pTC with a higher time resolution and much more components. Two complementary methods have already been developed to achieve the required time calibration precision between pixels. The characteristics and the performance of each method is summarized in Tab. 4.3.

[1] It was found in past studies that a geometrical mean of the two charges gives a better reconstruction than an arithmetic mean.

Table 4.3: A comparison of the two time calibration methods.

Method	Laser calibration	Michel calibration
Number of pixels	432	512
Uncertainty	24 ps	$\sim$ 10 ps
Major advantage	No beam needed	High coverage and precision

4.4.3.1 Laser calibration

One is a time calibration method using laser light. As was shown in Fig. 4.4, most pixels have a laser fiber inserted into the scintillator, from which a laser light can be injected.[2] Fig. 4.15 shows the overall picture of the laser system (PLP-10 from Hamamatsu Photonics [50] is used for the light source). The laser light is divided using optical splitters and can be injected into 432 of the 512 pixels. By illuminating multiple pixels simultaneously, a time synchronization between pixels is possible. The optical lengths of the laser system components are measured in advance. Using this method, a time calibration accuracy of 24 ps was already demonstrated in the pre-engineering run in 2016 (pER2016) [51]. The laser system can also be used for a signal check or other various DAQs without the muon beam.

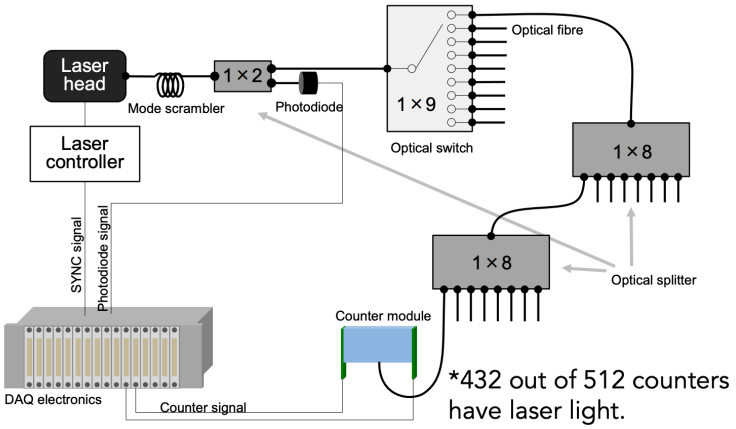

Figure 4.15: A schematic overview of the laser system.

4.4.3.2 Michel calibration

The other method is based on the positron tracks using the muon beam, and is commonly called the "Michel calibration". Since the positron TOF between pixels can be obtained from the positron track, the inter-pixel time offsets can be calibrated using multiple-hit events. The Michel calibration minimizes the χ^2 defined as

$$\chi^2 = \sum_{i=1}^{N_{\text{event}}} \sum_{j=1}^{N_{\text{hit}}} \left(\frac{t_{ij} - (t_{i1} + TOF_{i1j} + \Delta T_j)}{\sigma} \right)^2 \tag{4.11}$$

[2]Pixels positioned in the most inner z do not have the laser fiber inserted due to geometrical restrictions.

where N_{event} is the number of events, N_{hit} is the number of pixel hits in a track, t_{ij} is the reconstructed hit time of the j-th hit in the i-th event, t_{i1} is the estimated hit time of the first-hit pixel, and TOF_{i1j} is the estimated TOF from the first-hit pixel to the j-th hit in the i-th event. Here, ΔT_j is the intrinsic time offset of the j-th hit pixel, and the parameter to be calibrated. In MC simulation, 6 ps precision can be obtained.

The Michel calibration was performed with the fully constructed pTC in the pER2017. The difference between the time offsets obtained in the two methods is plotted in Fig. 4.16, in which a standard deviation of ~ 50 ps is seen. From this result, the uncertainty of the time calibration for an arbitrary pixel is estimated to be $50\,\text{ps}/\sqrt{2} \sim 35$ ps.

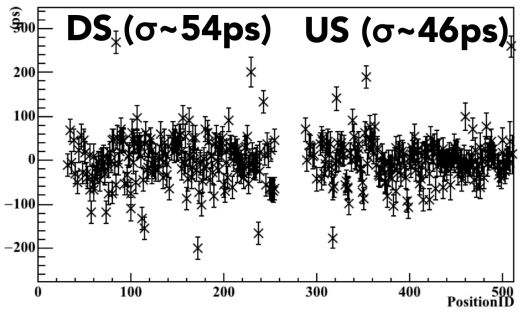

Figure 4.16: Difference between the time offsets obtained in the Michel and the laser calibration method [52].

4.5 Performance

4.5.1 Multiple-hit scheme

The pTC time resolution has greatly improved from the MEG TC for its segmented design. First, the small size of each pixel greatly reduces the variation of the optical path lengths of the scintillation light, which results in a high single-pixel time resolution. The time resolution strongly depends on the noise condition, but a mean resolution of ~ 72 ps and ~ 81 ps are obtained for 4 cm and 5 cm pixels respectively in lab tests.

Second, the positron time resolution improves by a factor, $1/\sqrt{N_{\text{hit}}}$, with the number of hit pixels, N_{hit}. Fig. 4.17 is a preliminary result showing a distribution of the number of hit pixels for signal positrons using MC simulation, and Fig. 4.18 shows the pTC resolution as a function of the number of hit pixels. A typical signal positron hits ~ 9 pixels, so the overall pTC resolution can be estimated as roughly 1/3 of the single-pixel resolution.

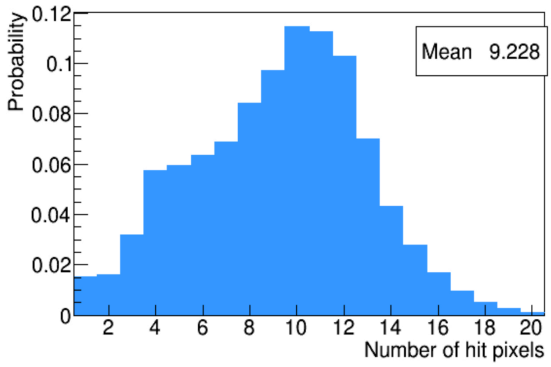

Figure 4.17: Distribution of the number of hit pixels for signal positrons in MC simulation [47].

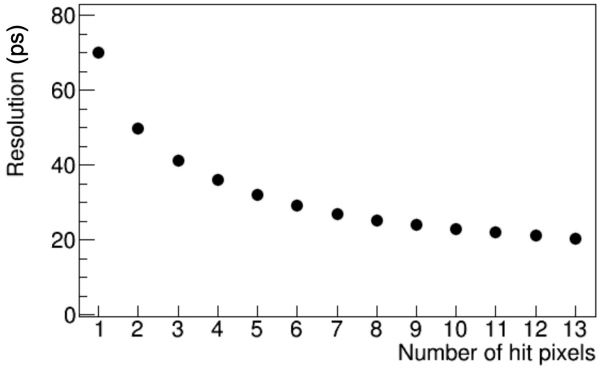

Figure 4.18: The overall pTC resolution as a function of the number of hit pixels [47].

4.5.2 Expected performance

To get a more precise estimate of the pTC resolution, some additional effects, like the uncertainty of the inter-pixel time calibration must be taken into account. Indeed, a more accurate resolution of the pTC for a N_{hit}-hit event can be written in the form

$$\sigma_{t_e^+}(N_{\mathrm{hit}}) = \sqrt{\frac{\sigma^2_{\mathrm{single}} + \sigma^2_{\mathrm{inter-pixel}} + \sigma^2_{\mathrm{elec}}}{N_{\mathrm{hit}}} + \sigma^2_{\mathrm{const}}} \tag{4.12}$$

where σ_{single} is the intrinsic resolution of a single pixel, $\sigma_{\mathrm{inter-pixel}}$ is the uncertainty of the inter-pixel time calibration, σ_{elec} is the uncertainty from the electronics jitter, and σ_{const} is the uncertainty from other effects that does not scale with $1/\sqrt{N_{\mathrm{hit}}}$, such as the effect from the multiple scattering of positrons.

A rough estimation of the pTC resolution has already been made in [51] using the pER2016 data. It assumes the single-pixel resolution of 93 ps, which also includes the electronics jitter and the uncertainty of the inter-pixel calibration to be 39 ps by comparing the consistency between the laser and the Michel calibration. In addition, making a rough estimation of $\sigma_{\mathrm{const}} \sim 10$ ps and using a typical value of 9 pixel hits, the overall pTC resolution is roughly evaluated to be

$$\sigma_{t_e^+} \sim \sqrt{\frac{(93\,\mathrm{ps})^2 + (39\,\mathrm{ps})^2}{9} + (10\,\mathrm{ps})^2} \simeq 35\,\mathrm{ps}. \tag{4.13}$$

4.6 Slow control system

The slow control system enables the monitoring and the controlling of the physical quantities that change slowly over time during operation, such as the temperature and the humidity. The pTC is actually planned to be operated in a cooled and dried condition, so here, I introduce the temperature and humidity control system for the pTC.

4.6.1 Motivation

4.6.1.1 Radiation damage to SiPMs

As briefly mentioned in 4.2.2.2, radiation damage to SiPMs can significantly increase the amount of dark noise. There are two types of radiation damage; one is bulk damage to Si from non-ionizing energy loss (NIEL) of energetic particles, and the other is surface damage to SiO_2 from ionizing energy loss (IEL) of charged particles such as electrons. The former can potentially create lattice defects, which give rise to new energy levels in the Si band gap and increase the thermal excitation of electrons. The latter can cause charge accumulation in the oxide, again creating new energy levels. The latter effect is already known to be negligible in our case [53], and therefore, the dominant damage for the MEG II pTC is the former. The precise dose level is estimated to be equivalent to $\sim 5 \times 10^9\,/\mathrm{cm}^2$ 1 MeV neutrons in the three-year physics run. The details of the dose calculation are given in Appendix A.

The problem with the increase of dark noise is that it can degrade the time resolution of the pTC. A basic study on the effect of radiation damage to SiPMs on the pTC performance has already been conducted [54]. In this study, SiPMs were irradiated with an electron source in several steps to a level comparable to the MEG II pTC damage level, and the single-pixel time resolution was measured at each damage level. From this study, a resolution deterioration of $\sim 30\,\%$ is expected at the temperature of 30 °C.

4.6.1.2 Effect of cooling

As mentioned in 4.2.2.2, the DCR of SiPMs has a strong dependence on the temperature. This means that the dark noise can be suppressed by cooling the SiPMs and thus reducing the thermal excitation of electrons. The effect of cooling SiPMs on the pTC performance was also studied in [54], and the results are shown in Fig. 4.19. The increase of dark noise with radiation damage is apparent from the current increase, and the effectiveness of cooling is apparent from comparing the two plots. The conclusion was that the $\sim 30\,\%$ degradation of the pTC resolution at 30 °C can be suppressed to $\sim 5\,\%$ by cooling the SiPMs to 10 °C.

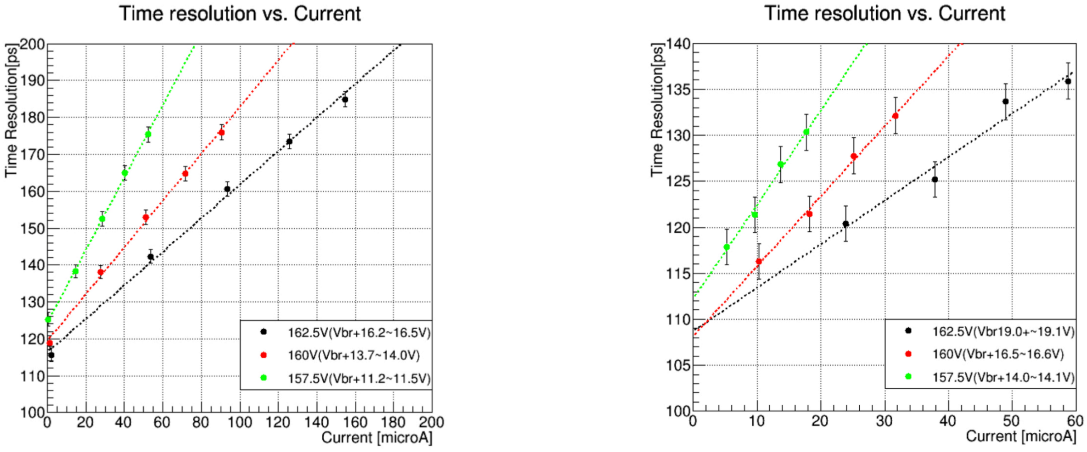

(a) Measurement at 30 °C (b) Measurement at 10 °C

Figure 4.19: The single-pixel time resolution as a function of the readout current [54]. Different points in the same color show measurements at different damage levels.

4.6.2 Temperature control

From the study described above, the pTC is planned to be operated in a 10 °C cooled condition. A basic cooling system has already been developed [54]. Water chillers (SH150-1000 from LabTech [55]) are used to deliver cooled water to the copper pipes attached to the backside of the support structure. This is schematically depicted in Fig. 4.20. The water cools the entire support structure including the BPs. As each pixel is fixed onto the BP using a thermal link and thermal paste to enhance the thermal conductivity, the SiPMs should also be sufficiently cooled with this system. Numerous thermometers (DS28EA00 from Maxim Integrated [56]) are mounted on the BPs for monitoring, and the temperature stability at 10 °C has already been confirmed.

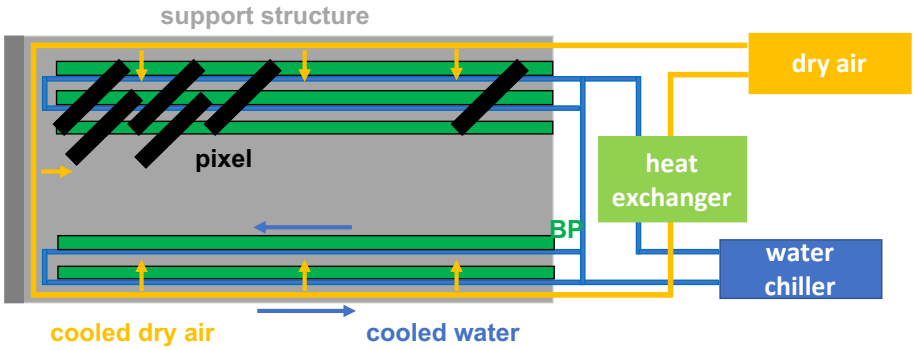

Figure 4.20: A schematic view of the pTC cooling system.

4.6.3 Humidity control

The humidity must also be controlled as the cooled operation can potentially cause water condensation in the pTC, which we do not want both from the material and the

electronic stability point of view. The humidity control system has also been developed [54], and is also demonstrated in Fig. 4.20. It makes use of the dry air available at PSI; the dry air is cooled down by the cooled water at the heat exchanger and is flushed into the pTC through pipes mounted around the support structure. There are also several hygrometers (HIH-4000 Series from Honeywell [57]) attached to the BPs to monitor the humidity. The stability of the humidity control system at 10 °C condition has already been achieved by covering the pTC with a thin plastic foil to keep the dry air in.

4.7 Operation

The construction of the pTC started in 2015, and since then, several pERs have already been performed to demonstrate the performance of the pTC. Tab. 4.4 summarizes the number of readout channels, together with the major update in each year. In this section, I summarize what has already been achieved by the pTC group in the past years.

Table 4.4: A summary of the past pERs.

Year	Number of channels	Readout region	Major update
2015	256	1/2 DS (middle ϕ)	1/4 detector constructed
2016	256	1/2 DS (middle ϕ)	Laser system developed
2017	512	DS and US	Full detector constructed
2018	256	1/2 DS (latter z)	Cooling system developed
2019	256	1/2 US (middle z)	Advance in positron analysis

4.7.1 pER2015

The construction of the pTC started in 2015, and 128 DS pixels had been integrated onto a prototype support structure by the pER2015. The basic method of the pixel assembly, as well as the pTC insertion and extraction system were established this year. In addition, a first test of the laser system was performed with 8 pixels. However, the analysis of the data was strictly limited by some issues on the DAQ side.

4.7.2 pER2016

There were two major updates in the pER2016 from the hardware point of view. First, the final support structure was constructed and all of the 256 DS pixels were integrated. Second, the laser calibration was performed with 40 pixels. DAQ issues in the previous year were fixed and the calibration and the data analysis were made possible. The effectiveness of the multiple-hit scheme was demonstrated using the pTC clustering analysis.

4.7.3 pER2017

The construction of the full detector was finished in 2017, and although the number of readout electronics was limited, all channels were read out by dividing the DAQ period

in two, one for the DS and one for the US pTC. The laser calibration was also performed with the full system, demonstrating ~ 35 ps inter-pixel time calibration precision together with the Michel calibration. For the data analysis, a first realistic evaluation of the overall pTC resolution was performed using fixed geometrical combinations of pixels in clusters, yielding the value of ~ 38.5 ps.

4.7.4 pER2018

The full cooling system was established in 2018, and its general effect and its stability were demonstrated in the pER2018. There was also another big update on the software side; the pTC tracking algorithm (c.f. 4.3.4) was developed. This allows us to get a better evaluation of the pTC resolution, as well as improve the pTC-CDCH positron matching quality.

Concerning the positron spectrometer as a whole, the construction of the CDCH was completed and it was installed for the first time. Although the CDCH showed very different behaviors to that of the MC CDCH (e.g. low gain, instability of the baseline, etc.), a combined analysis of the CDCH and the pTC was finally made possible.

4.7.5 pER2019

Further understanding of the detector and advances on the software side were achieved in the pER2019, which are the topics of this thesis. In addition, a basic combined tracking algorithm of the pTC and the CDCH was developed, which is beyond the scope of this thesis.

4.8 Tasks

As explained above, the hardware system of the pTC has already been constructed, and the standard calibration methods and analysis algorithms have also been established. However, there still remain some issues that must be solved.

One concerns the stable operation of the pTC. Our group has faced a malfunctioning of some channels in the past. Although the cause was investigated and some countermeasures were taken, we cannot deny the possibility of a similar malfunctioning occurring in the future, in which case we expect to partly lose the efficiency and the resolution. In preparation for such accidents, the construction of spare pixels is essential. By doing so, even if we encounter some unexpected failure of some pixels, we would be able to replace them immediately and maintain the expected pTC performance.

Another remaining task is a detailed study on the effect of radiation damage to SiPMs. Although a basic study on the general effect of radiation damage to SiPMs has been conducted, no study has been performed to see its effect on SiPMs connected in series. This is a fundamental but essential study that must be done to get a precise understanding of our detector.

These topics are covered in chapter 5 and chapter 6 respectively. The rest of this thesis demonstrates various attempts to maintain the high pTC performance in the long run.

Part II

Long-term Operation of pTC

Chapter 5

New Pixel Assembly

18 new pixels were assembled as spares. In this chapter, I describe the assembly procedure and the various tests at each assembly step. In the end, the single-pixel performance of the newly-assembled pixels are given.

5.1 Background

The series connection of SiPMs have the advantage of sharper signal waveforms. However, from the viewpoint of the long-term detector operation, there is a risk that a malfunctioning of a single SiPM can result in a dead channel. Such a case has already been confronted in the past, where the anode and the cathode of a SiPM suddenly became electrically disconnected.

Another known case of malfunctioning is the detachment of SiPMs from the scintillator tile as depicted in Fig. 5.1a. It is assumed to be caused by a mechanical stress on the SiPM array arising from a mismatch between the channel interval of the pixel and that of the support structure. A countermeasure for this problem has already been taken; a tiny scratch is created to the scintillator, and additional optical cement is put between some SiPMs to reinforce the adhesiveness. This is depicted in Fig. 5.1b.

(a) (b)

Figure 5.1: A schematic drawing of (a) the detachment problem and (b) the countermeasure against it.

Although we expect the detachment problem to have been solved by the reinforcement, we do not know the cause for the former problem, and we cannot deny the possibility of

some dead channels appearing in the three-year physics run. A dead channel degrades the single-pixel resolution, and also makes impossible the hit time and position reconstruction in the pixel. Therefore, to maintain the pTC performance, it is necessary to construct spare pixels, to which we can swap the pixel with a dead channel if any such case arises.

5.2 Overview

18 new pixels were assembled: nine 4 cm pixels and nine 5 cm pixels. The assembly procedure is shown in Fig. 5.2. First, the SiPMs were soldered onto PCBs in groups of six. Second, the SiPM arrays were glued onto scintillator tiles cut into the standard size, and thus the pixels were constructed. Lastly, the scintillators were wrapped with reflective foils and then with polyvinyl fluoride films for light-shielding.

There were also some measurements to be performed at each assembly stage. After the soldering process, a current-voltage (I-V) measurement of each SiPM array was performed to obtain the breakdown voltage. A signal check using an LED light was also performed to see the signal size of each SiPM array. After the pixel assembly, measurements using a ^{90}Sr radiation source were performed. The bias voltage was scanned first for each pixel to determine the operation voltage. Lastly, a hit position scan was performed to evaluate the final single-pixel performance of each pixel.

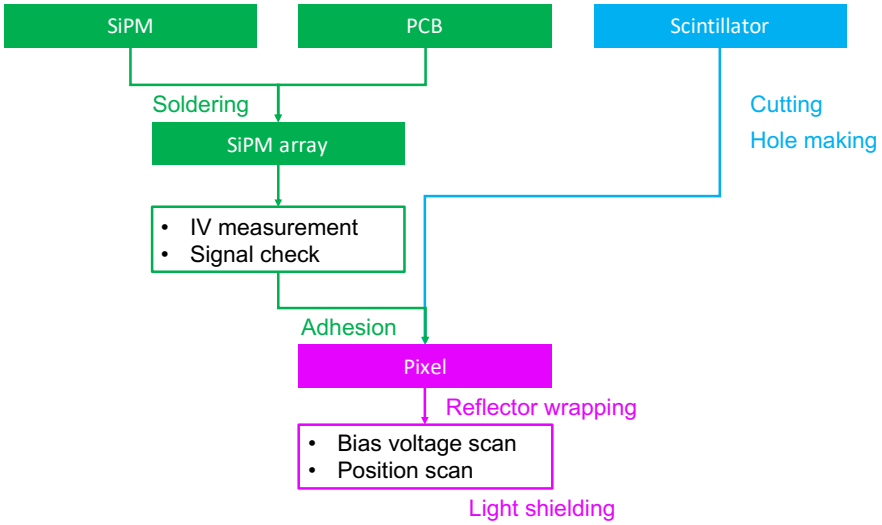

Figure 5.2: The procedures for a pixel assembly.

5.3 I-V measurement

5.3.1 Measurement

After the soldering process, I-V measurements were performed for the SiPM arrays, in which the behavior of the current flow with respect to the applied bias voltage was measured. The breakdown voltage of a SiPM array can be obtained from the obtained I-V curve. The I-V measurement is particularly important for the new pixels as the

constituting SiPMs (type III in Tab. 4.2) are different from the ones used in old pixels (type I or II), and have different I-V characteristics. The new SiPMs soldered onto PCBs are shown in Fig. 5.3.

The setup for the I-V measurement is schematically shown in Fig. 5.4. The PCBs were placed in a thermal chamber kept at 30 °C, and both the HV application and the current readout were performed using a picoammeter (6487 picoammeter from Keithley [58]). The data was taken in 0.1 V steps and all the 36 SiPM arrays were measured.

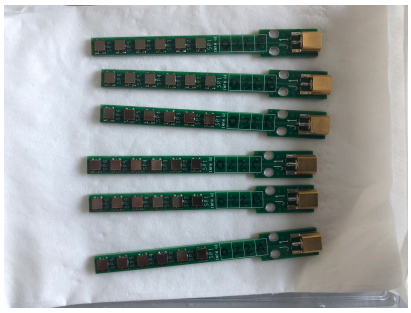

Figure 5.3: A picture of new SiPMs soldered onto PCBs.

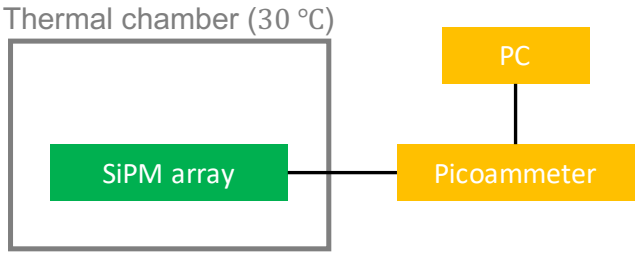

Figure 5.4: A schematic drawing of the I-V measurement setup.

5.3.2 Breakdown voltage

Fig. 5.5 shows the obtained I-V curves of all 36 SiPM arrays. One SiPM array (O24F) shows a strange I-V curve, but similar I-V characteristics are seen in all the others. The apparent breakdown voltage of $\sim$ 160 V is relatively high compared to old SiPM arrays (type I and II), whose breakdown voltages are typically $\sim$ 145 V at the same temperature.

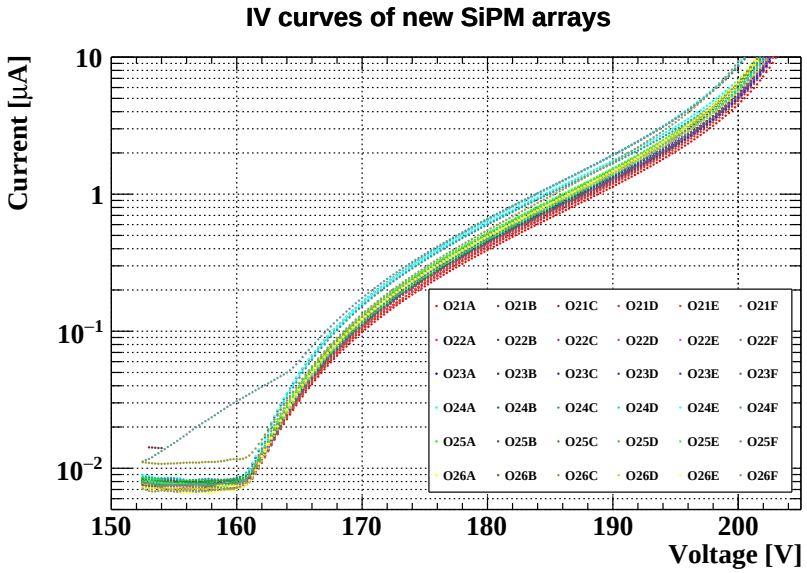

Figure 5.5: I-V curves of new SiPM arrays.

The breakdown voltage of each SiPM array was obtained in the following procedures:

1. Take the moving average of the I-V curve using five points to suppress the measurement error.
2. Calculate the second derivative of the curve.
3. Take the moving average of the curve again.
4. Fit the peak with a quadratic function.

Fig. 5.6 shows the result at each analysis step for a typical channel. The breakdown voltage in this method is defined as the axis of the fitted quadratic function. The obtained values are shown in Fig. 5.7. The variation of the breakdown voltages is very small except for O24F previously mentioned.

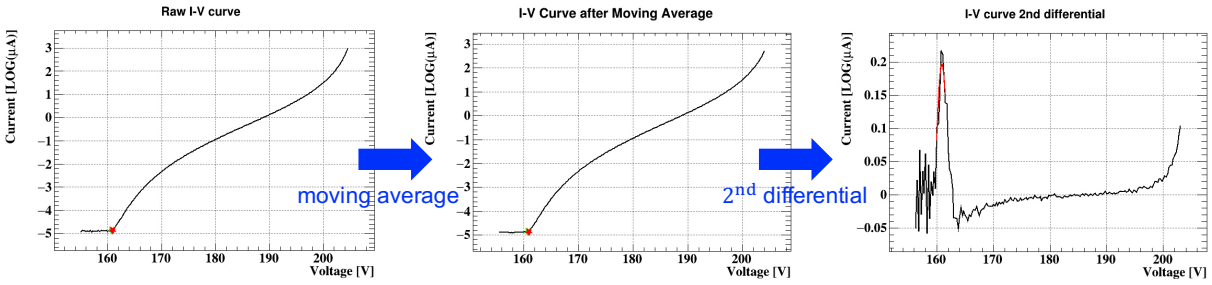

Figure 5.6: The procedure to calculate the breakdown voltage from the raw I-V curve (left). The middle shows the curve after taking the moving average, and the right shows the curve after taking the second derivative and then the moving average again.

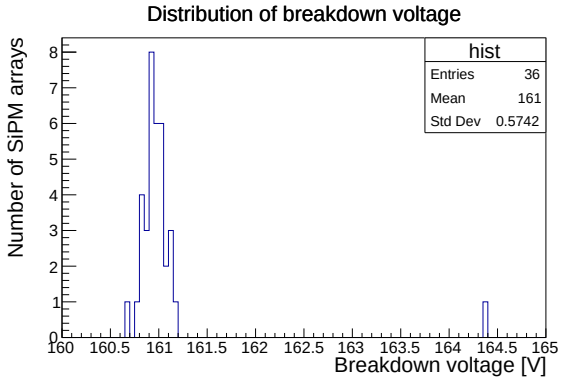

Figure 5.7: Distribution of the obtained breakdown voltages.

5.4 Signal check

After the I-V measurement, the signal check of each SiPM array was performed using an LED light source. The measurement setup is shown in Fig. 5.8 and Fig. 5.9. The SiPM arrays were again placed in a thermal chamber kept at 30 °C. The HV to the SiPMs were applied using the same picoammeter, and the voltage was set to +18 V of the obtained

breakdown voltage[1]. The signals were amplified using an amplifier developed at PSI. For the DAQ, a DRS Evaluation Board was used, which was also developed at PSI and works in the same way as the WDBs.

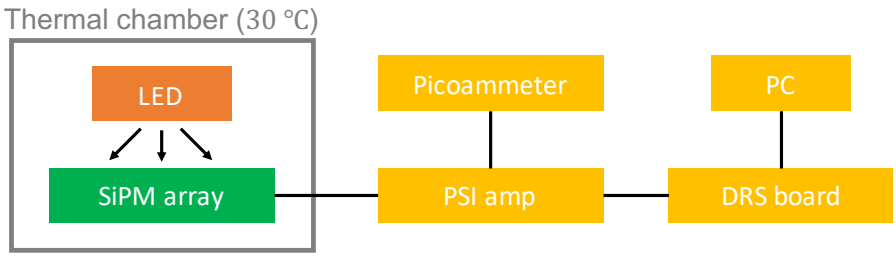

Figure 5.8: A schematic drawing of the signal check setup.

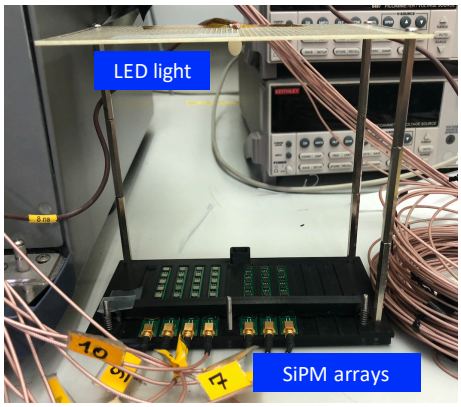

Figure 5.9: The SiPM arrays fixed onto a support structure with an LED light.

The result is shown in Fig. 5.10. The amount of light injected into each SiPM array depends on the PCB position in the support structure, so this effect is corrected offline. The signal can be seen in all SiPM arrays, including the one with a strange I-V characteristic, with $\sim 10\,\%$ deviation in the observed signal size.

[1]The breakdown voltage of the SiPM array with a strange I-V characteristic (O24F) was assumed to be a typical value of 161 V, and the overvoltage was set to 179 V.

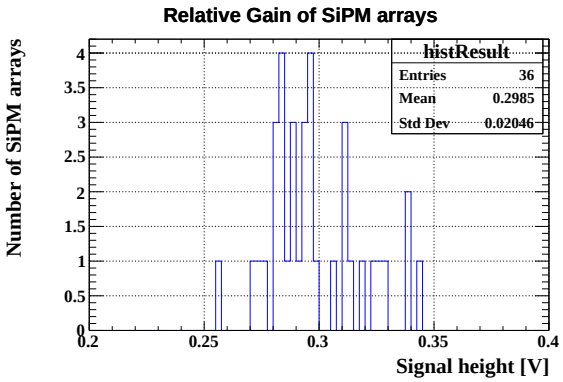

Figure 5.10: Distribution of the obtained mean signal height.

5.5 Pixel assembly

After the basic tests of the SiPM arrays, the pixels were assembled one by one. First, the optical cement (BC600) was evacuated and heated to remove any void in the material. Second, using a jig shown in Fig. 5.11, the SiPM arrays were glued onto both sides of the scintillator tiles. In this procedure, SiPM arrays with close breakdown voltages obtained in 5.3.2 were chosen as pairs and used in the same pixel. The procedure to strengthen the connection (c.f. 5.1) was also taken. After the SiPM-array attachment, each scintillator was wrapped with a reflective foil (ESR from 3M). Afterwards, each pixel was wrapped with a polyvinyl fluoride film (Tedlar® [44]) and a black tape for light shielding and the assembly was completed. The assembly procedure is shown in Fig. 5.11.

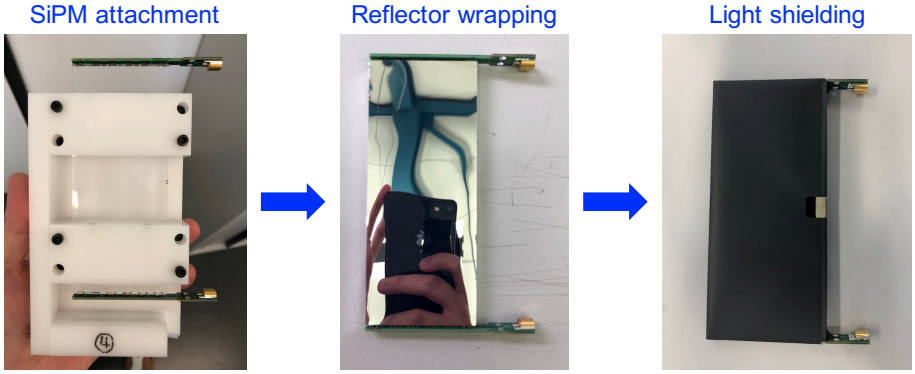

Figure 5.11: The pixel assembly procedure.

5.6 Bias voltage scan

The bias voltage scan is necessary to determine the operation voltage of SiPMs. The setup for the measurement is shown in Fig. 5.12. Electrons from a ^{90}Sr radiation source were injected to the center of the pixel and to a trigger counter below it. The trigger counter is composed of a 5 mm × 5 mm × 5 mm plastic scintillator wrapped with Teflon

and a SiPM (S10362-33-050C from Hamamatsu Photonics [59]) for readout. The two channels of the pixel and the trigger counter were read out using PSI amplifiers and a DRS Evaluation Board. The HV to each channel was supplied from different picoammeters.

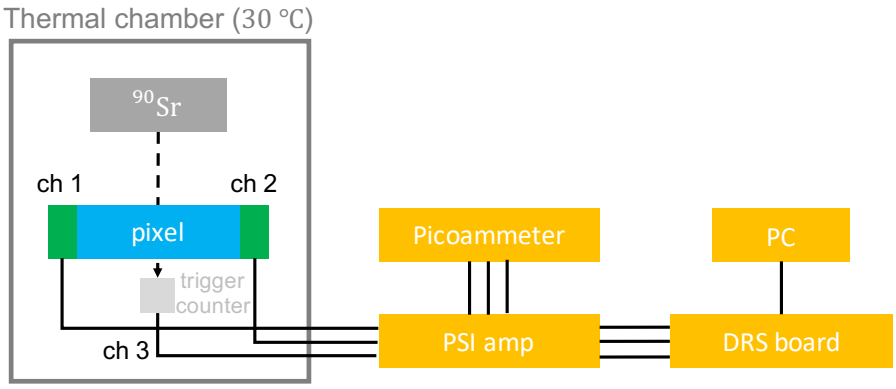

Figure 5.12: A schematic drawing of the bias voltage scan setup. Two PSI amplifiers and two picoammeters are omitted in the drawing.

The bias voltage scan was performed in steps of 0.5 V for five of the newly assembled pixels. The resulting single-pixel resolution is plotted as a function of the overvoltage in Fig. 5.13. The single-pixel resolution for each pixel is obtained from the distribution of

$$t = \frac{t_{\mathrm{ch1}} + t_{\mathrm{ch2}}}{2} - t_{\mathrm{trigger}} \tag{5.1}$$

where t_{ch1} and t_{ch2} are the signal times obtained in the two channels, and t_{trigger} is the time obtained by the trigger counter. The standard deviation of this t distribution, corrected by the ~ 30 ps resolution of the trigger counter is defined as the single-pixel resolution.

Fig. 5.13 indicates that an optimal overvoltage from the time resolution viewpoint lies somewhere around ~ 25 V for all pixels. This is because the signal-to-noise ratio (S/N) largely affects the time resolution and both the signal and noise level are dependent on the overvoltage. From this result, all new pixels will be operated at the overvoltage of 24 V, which corresponds to 4 V overvoltage for each SiPM.

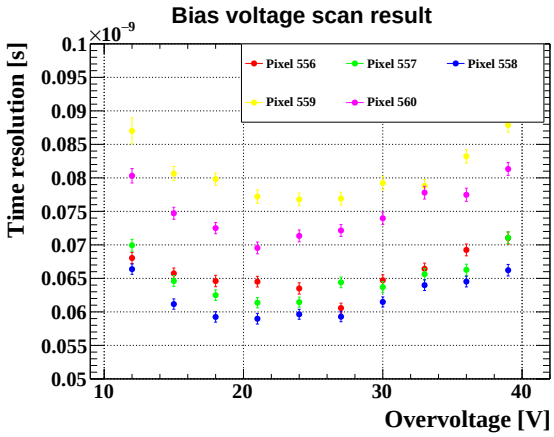

Figure 5.13: Overvoltage dependence of the single-pixel resolutions.

5.7 Position scan

The final single-pixel resolutions were determined by performing position scans at the determined bias voltage. While the bias voltage scan was performed for only a part of the pixels, the position scan was performed for all new pixels. The measurement setup was almost exactly the same as the bias voltage scan. The only difference was that the pixel was mounted on a stage mover, and could be moved in local x direction.

The position scan was performed at three points of $x = -4.25\,\mathrm{cm},\ 0\,\mathrm{cm},\ 4.25\,\mathrm{cm}$ with a fixed $y = 0\,\mathrm{cm}$. The results are shown in Fig. 5.14. High resolutions are achieved independent of the hit position, and 4 cm pixels yield higher performance than 5 cm ones as expected. The resolution at the center position is defined as the final single-pixel resolution of each pixel.

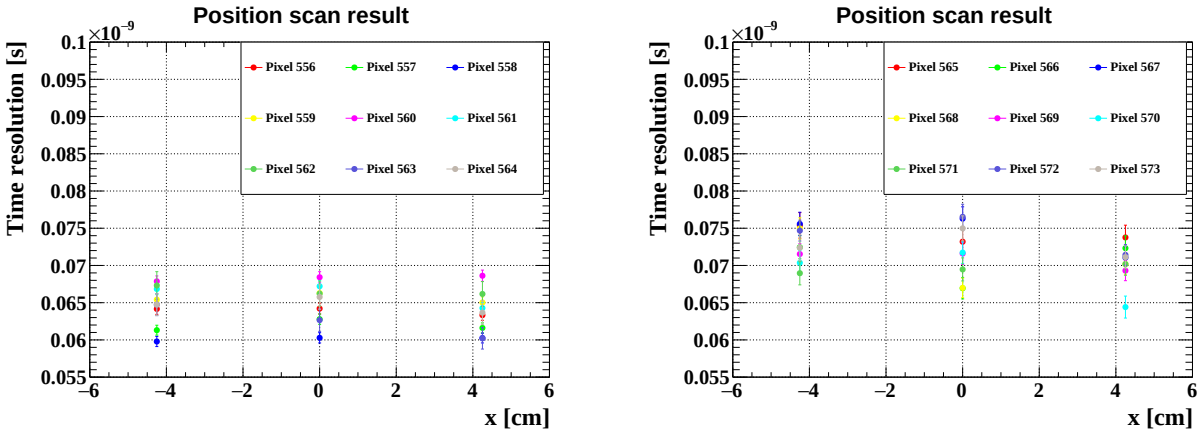

(a) 4 cm pixels (b) 5 cm pixels

Figure 5.14: x hit position dependence of the single-pixel resolutions.

The distribution of the obtained single-pixel resolutions are shown in Fig. 5.15, together with those of old pixels. It is obvious that the new pixels have a higher time resolution than the old ones. This is due to a higher gain and a lower noise level in the new SiPMs.

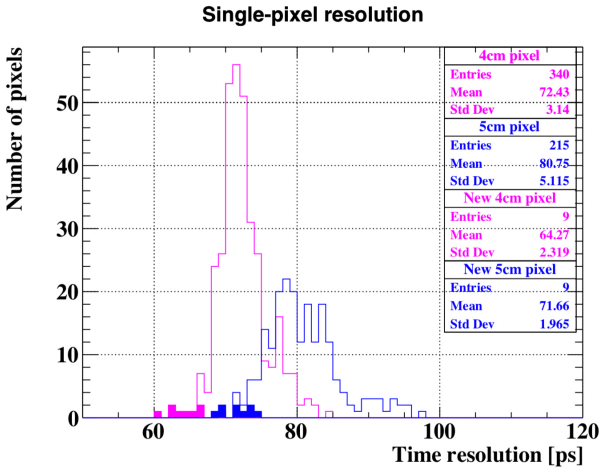

Figure 5.15: Distribution of the single-pixel resolutions. The color-filled histograms represent the new pixels, while the non-filled ones represent the old ones.

5.8 Conclusion

The original purpose of the new pixel assembly was to retain the new pixels as spares, to which we can replace any broken ones. However, as the new pixels showed better performance than the old ones, we decided to install the new ones in the pTC and keep the replaced ones as spares. Indeed 16 of these new pixels were installed in the US pTC and successfully operated in the pER2019.

Chapter 6

Radiation Damage to SiPMs

Measurements were performed to understand the effect of radiation damage to SiPMs on the time response of scintillation counters. Discussed in this chapter, are the results obtained in lab tests and their interpretations. In the last section, the impact of the newly-found effect on the pTC performance is evaluated.

6.1 Radiation damage to pTC SiPMs

Many studies on the general effect of radiation damage to SiPMs have been carried out in the past. The most prominent known effect is the increase of dark noise, which can directly deteriorate the time resolution of scintillation counters. However, as mentioned before, we already know that this can be suppressed to some extent by lowering the temperature of SiPMs.

In the case of the MEG II pTC, a linear increase of the current level due to the dark noise increase was observed in the past pERs. A simple extrapolation indicates that the originally $\sim 10\,\mu$A current level can reach $\sim 100\,\mu$A in the three-year physics run. This is consistent with a past study [54], in which SiPMs were irradiated to the radiation level expected in the MEG II pTC in the three years and yielded a current level of $\sim 100\,\mu$A. This study demonstrated that the deterioration of the pTC resolution due to the dark noise increase can be suppressed to $\sim 5\,\%$ by operating the detector at $10\,^{\circ}$C.

However, in the MEG II pTC case, there may be other effects of radiation damage other than the simple dark noise increase. One factor comes from the fact that the pTC utilizes a series connection of SiPMs, which is unique and has not been studied in detail before. Another comes from the gradation of the damage level within the series connection. Fig. 6.1 shows the positron hit dose dependence on the radial length in the pTC. It is apparent that SiPMs at higher local y receive more radiation damage than the ones at lower y. Such a special case has never been investigated before, and an additional study is essential in order to know the potential effects.

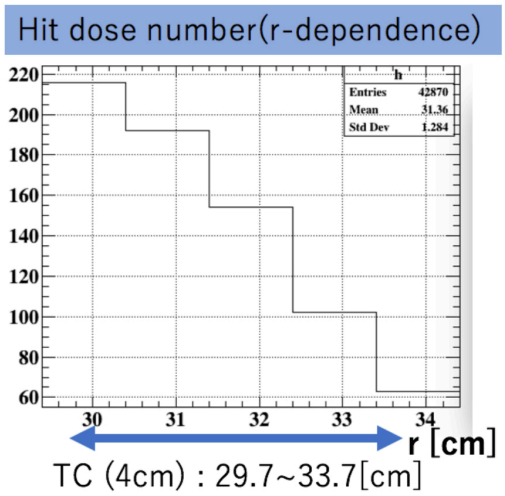

Figure 6.1: r dependence of the positron hit dose [54]. The number of positrons with each curvature radius is calculated using MC simulation.

6.2 Measurement

The aim of this study, therefore, was to investigate how radiation damage to series-connected SiPMs affect the pixel performance, especially when the radiation damage level is not uniform. To test this, we prepared SiPMs with different damage levels, and the measurement setup was designed to be flexible to be able to change the array of SiPMs and test various damage patterns. The details of the setup is explained in this section.

6.2.1 SiPMs

SiPMs with four damage types were prepared for this measurement; one was completely free from damage, another was irradiated with electrons, and the other two were irradiated with neutrons but to different levels. The electron irradiation was performed in the lab with a 37 MBq ^{90}Sr source and a collimator, and the final dose level was evaluated to be equivalent to $\sim 3 \times 10^9$ /cm^2 1 MeV neutrons. On the other hand, the neutron-irradiated samples were irradiated using reactor neutron facilities at the Laboratory of Applied Nuclear Energy (LENA) of University of Pavia. The dose levels were evaluated to be equivalent to $\sim 8.7 \times 10^8$ /cm^2 and $\sim 5.5 \times 10^9$ /cm^2 1 MeV neutrons respectively. This is summarized in Tab. 6.1. Note that the dose level expected in the pTC in three years is $\sim 5 \times 10^9$ /cm^2 1 MeV neutrons at the highest point. For the details of the dose calculation, see Appendix A.

Table 6.1: A list of SiPMs used in the measurement.

SiPM type	Damage type	Dose level equivalent to 1 MeV neutrons
a.	Non-damaged	0
b.	Neutron-damaged	$\sim 8.7 \times 10^8$ /cm^2
c.	Electron-damaged	$\sim 3 \times 10^9$ /cm^2
d.	Neutron-damaged	$\sim 5.5 \times 10^9$ /cm^2

Using these SiPMs, three types of SiPM arrays were created for the following measurements, each imitating the non-uniform damage pattern in a different way. The damage patterns are summarized in Fig. 6.2. The damage pattern C imitates the most realistic case, where the six SiPMs have gradient damage levels in sets of two. On the other hand, the damage pattern A and B are the extreme cases where two (four) of the SiPMs are damaged and four (two) are not at all.

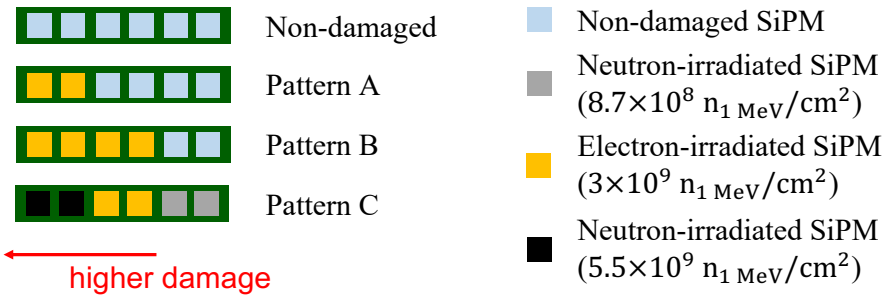

Figure 6.2: The damage pattern of SiPM arrays used for the measurements.

6.2.2 Pixel assembly setup

In order to test SiPM arrays with different damage patterns, the setup had to be flexible to allow an easy replacement of the SiPMs. This was realized by the parts shown in Fig. 6.3a and the assembly structure shown in Fig. 6.3b. The parts were designed using computer-aided design (CAD) and produced using a plastic 3D printer.

The scintillator plate was pinched between the two parts labeled 1. SiPMs were placed in the dimples in part 2 and stuck to both sides of the scintillator using optical grease. The two parts were fixed using screws. Part 3 with twelve spring test probe pins was fixed onto part 2 in such a way that the probe pins attached the electrodes of SiPMs through the holes in part 2 and created a series-connected circuit of SiPMs. The attachment of probe pins to the SiPMs can be seen in Fig. 6.4. By adopting this design, the SiPMs could be replaced simply by removing part 2 and part 3 temporarily.

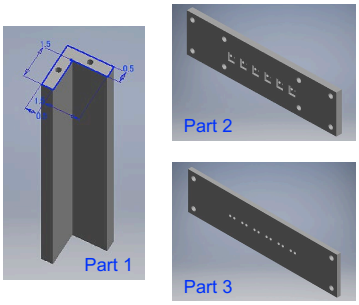

(a) The parts used in the assembly setup.

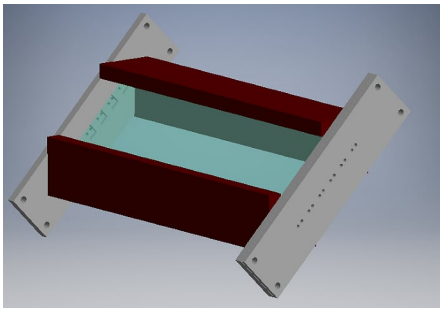

(b) The assembled structure with the scintillator plate in the middle.

Figure 6.3: A CAD design of the pixel assembly structure.

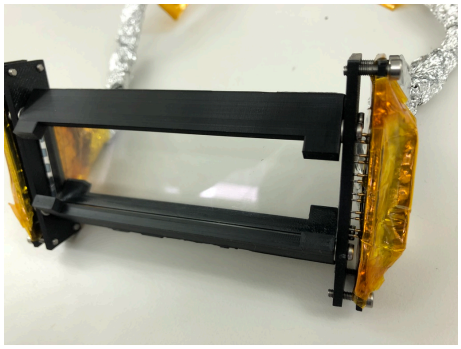

Figure 6.4: The assembled setup.

6.2.3 Overall setup

The overall setup was almost the same as the one used for the position scan in 5.7. The same ^{90}Sr source was used, the thermal chamber was set to $\sim 30\,^{\circ}$C, and the triggering was performed by the same trigger counter. The SiPM array to be tested was placed in channel one, whereas channel two was used as a reference with non-damaged SiPMs. The only additional requirement was the capability to scan the position in y direction to see the effect of non-uniform radiation damage.

This was realized by the setup depicted in Fig. 6.5. The position of the radiation source was fixed, so the pixel had to move in y direction. As the moving stage was capable of position scanning only in x direction, two aluminium bars were fixed onto the moving stage with screws. These bars had a number of screw holes at 5 mm intervals, making y position scanning possible.

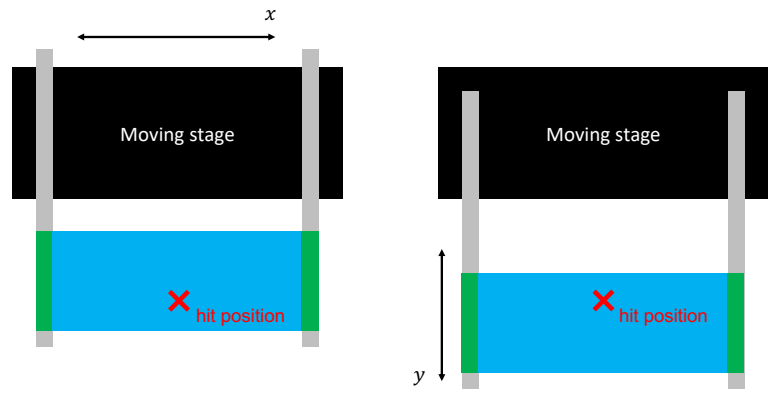

Figure 6.5: A schematic diagram of y position scanning.

6.2.4 Measurement

In order to clearly distinguish the effect of radiation damage to SiPMs from other effects, each damage pattern was tested with two configurations; one with the standard array of SiPMs, in which the SiPMs at higher y have higher damage, and the other with the reversed order of SiPMs. The difference in the two results can then be assumed to be caused by the unbalanced radiation damage to SiPMs. In addition, a completely damage-free array of SiPMs was also tested as a control experiment.

For each of these seven configurations, a position scan was performed both in x and y direction. x position scan was performed using the moving stage, while y position scan was performed by shifting the aluminium bars.

Besides that, I-V measurements were performed for each SiPM used in the measurement and for the series-connected SiPM array of each damage pattern, as the I-V characteristic reflects the damage level most effectively. The measurement setup used for the I-V measurement was exactly the same as that used in the new pixel measurement (c.f. 5.3).

6.3 I-V characteristics

The obtained I-V curves for each of the used SiPMs are depicted in Fig. 6.6. The I-V characteristics are clearly different according to the damage level of SiPMs; the ones with more damage show higher noise levels.

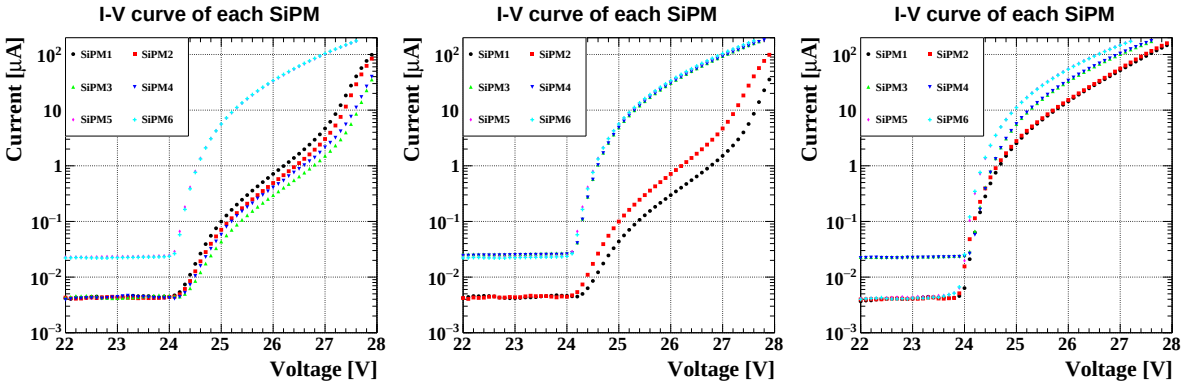

(a) Pattern A (b) Pattern B (c) Pattern C

Figure 6.6: I-V curves of SiPMs used in each damage pattern at 30 °C. SiPMs with less damage are labeled with younger numbers.

The I-V curves of the SiPM arrays with each damage pattern are shown in Fig. 6.7. From this, the overall damage level in each pattern can be extracted; pattern C has the highest damage, pattern B the second highest, and pattern A the lowest.

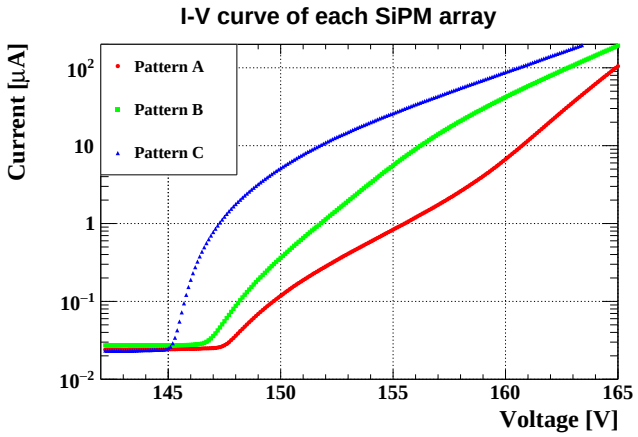

Figure 6.7: I-V curves of SiPM arrays with each damage pattern.

6.4 Effect on signal height

The effect of radiation damage on the signal height was checked. The pulse height in the following discussions are obtained by fitting the pulse height distribution with a Landau function convoluted with a Gaussian, and extracting the peak of the fitted function.

6.4.1 Position dependence of pulse height

Fig. 6.8 shows y hit position dependence of the pulse height when the hit point is close to the damaged channel ($x = -4.25\,\mathrm{cm}$) for each damage pattern. A similar and

clear position dependence is seen in all damage patterns, and the behavior is opposite for the standard and the reversed configuration. This clearly implies that this position dependence is a result of the gradient damage to SiPMs.

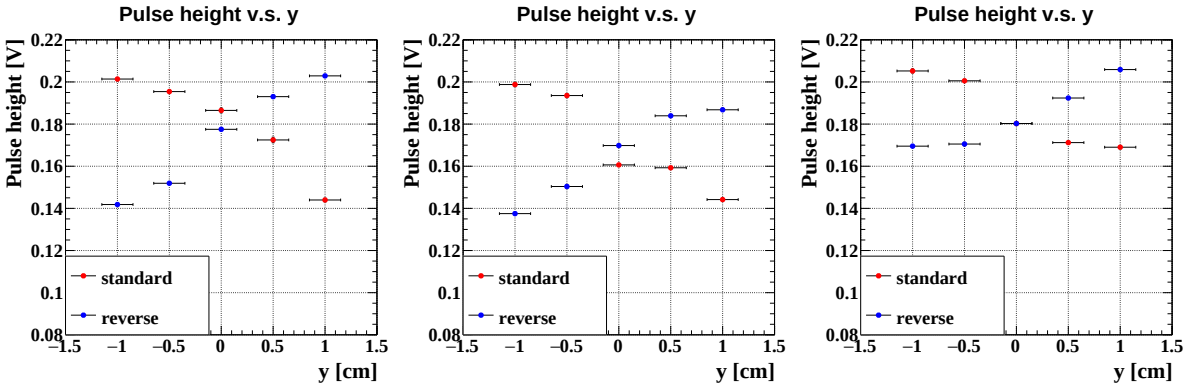

(a) Pattern A (b) Pattern B (c) Pattern C

Figure 6.8: y hit position dependence of the pulse height at $x = -4.25\,\mathrm{cm}$ in each damage pattern. The red and blue markers correspond to the standard and the reversed configuration respectively.

Fig. 6.9 shows the same position dependence for pattern A, but when the hit point is farther away from the damaged channel. The position dependence becomes less prominent as the hit point shifts farther away. Similar results are seen in other damage patterns.

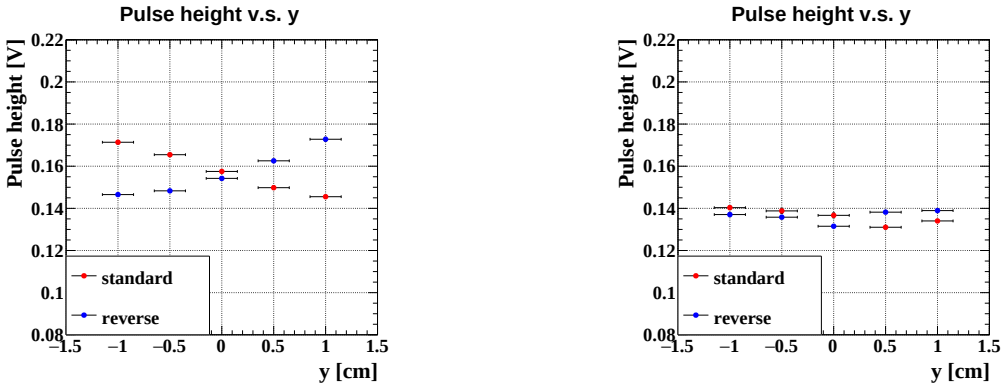

(a) $x = -3\,\mathrm{cm}$ (b) $x = 0\,\mathrm{cm}$

Figure 6.9: y hit position dependence of the pulse height in pattern A at different x.

6.4.2 Interpretation

The general drop in the signal height as the hit point shifts farther away can be explained by a decrease in the scintillation light collection efficiency. This must also be true in y direction; that is more scintillation light is collected by SiPMs placed closer to the hit point. Therefore, it naturally follows that the SiPM closest to the hit point must produce the dominant signal. Combining this speculation with the position dependence

result in Fig. 6.8, it is concluded that SiPMs with less damage produce larger signals than the ones with more damage.

This is caused by a variation in the SiPM gains. In a series connection of SiPMs, the bias voltage to each SiPM is applied in such a way that a common current flows through all SiPMs. Therefore, the applied voltage to each SiPM depend on the I-V characteristics of the constituting SiPMs. This effect is schematically depicted in Fig. 6.10. The difference in I-V characteristics causes overvoltage variation, and therefore gain variation amongst SiPMs. This interpretation explains the general position dependence, as well as the smaller position dependence in pattern C arising from a smaller damage difference.

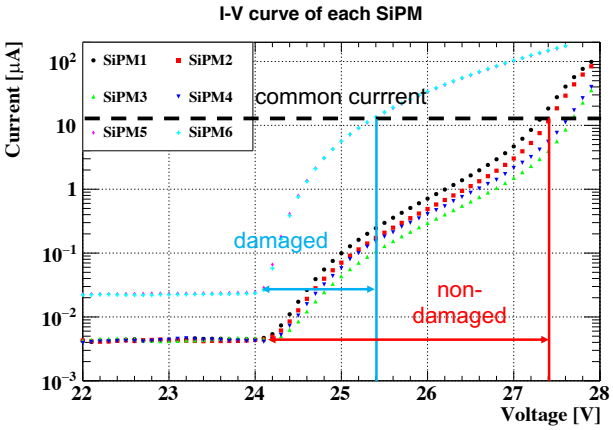

Figure 6.10: A schematic view of how the overvoltage variation among series-connected SiPMs is produced. I-V curves of SiPMs in pattern A are used.

6.5 Effect on time response

In a similar way, the effect of the radiation damage on the time response was checked, as this is most important for the pTC operation. The time center in this section is defined as the Gaussian mean of the $t_{\mathrm{ch1}} - t_{\mathrm{trigger}}$ distribution. The constant fraction (CF) method is used in the analysis with the fraction set to 20 %.

6.5.1 Position dependence of time center

Fig. 6.11 shows y hit position dependence of the time center at $x = -4.25\,\mathrm{cm}$ for each damage pattern. A similar and clear position dependence is seen in all damage patterns. This time, however, the two configurations yield similar results. This implies the existence of some intrinsic position dependence of the time center independent of the radiation damage.

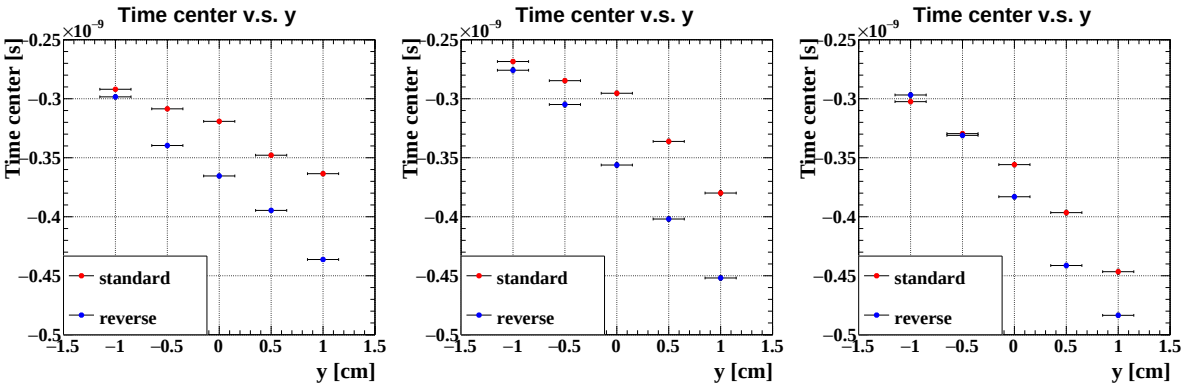

(a) Pattern A (b) Pattern B (c) Pattern C

Figure 6.11: y hit position dependence of the time center at $x = -4.25\,\mathrm{cm}$ in each damage pattern.

Fig. 6.12 shows the same position dependence using SiPMs without any damage. An intrinsic position dependence is clearly seen. However, the results in each damage pattern in Fig. 6.11 show significant deviations from this result, suggesting that some additional effect is caused by the radiation damage. This additional effect seems to enhance the position dependence in the reversed configuration more than in the standard configuration.

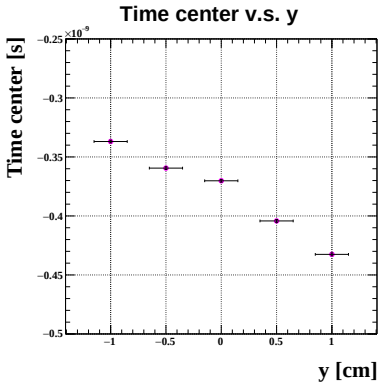

Figure 6.12: y hit position dependence of the time center at $x = -4.25\,\mathrm{cm}$ for a SiPM array with damage-free SiPMs.

Fig. 6.13 shows the same position dependence for pattern A, but at different x. The position dependence becomes less prominent as the hit point shifts away from the channel. Similar results are seen in other damage patterns.

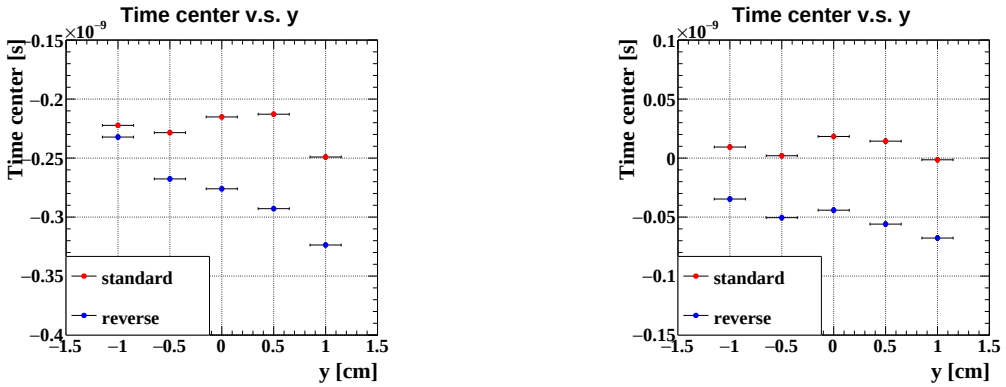

(a) $x = -3\,\mathrm{cm}$ (b) $x = 0\,\mathrm{cm}$

Figure 6.13: y hit position dependence of the time center in pattern A at different x.

6.5.2 Interpretation

First, the intrinsic position dependence is assumed to be caused by a finite propagation time of the scintillation light through the scintillator and the electronic signal through the SiPM array. In our measurement setup, the readout is in $+y$ direction, so this accounts for the general position dependence that the signals from higher y hit are detected earlier than those from lower y hit.

The additional effect from radiation damage is more complex. In fact, the time center behavior is determined mainly by the following four factors:

- The distribution of photons to each SiPM.
- The gain of each SiPM.
- The time response of each SiPM.
- The signal propagation speed in the SiPM array.

This is because the CF method utilizes both the leading edge of the pulse, which is determined by the fastest fraction of the signal, and the pulse peak, which is determined more or less by the sum of signals from all SiPMs. Assuming a finite signal propagation speed, the rising part of the signal is likely to be produced by a few SiPMs closest to the readout. However, the non-uniform radiation damage can complicate matters by creating an overvoltage variation amongst the SiPMs, which can affect both the gain and the time response of SiPMs.

The mechanism to cause a gain variation was discussed in 6.4.2. The time response of a SiPM also has an overvoltage dependence. This dependence was checked by performing a bias voltage scan with the same setup. The result is shown in Fig. 6.14. Both damaged and non-damaged SiPMs show faster time response with higher overvoltage, although it saturates at some point. This can be explained by the charge collection speed in SiPMs; charge carriers in Si can be collected faster in a stronger electric field. Thus, SiPMs with less damage, and therefore higher overvoltage, show a faster time response than the ones with more damage.

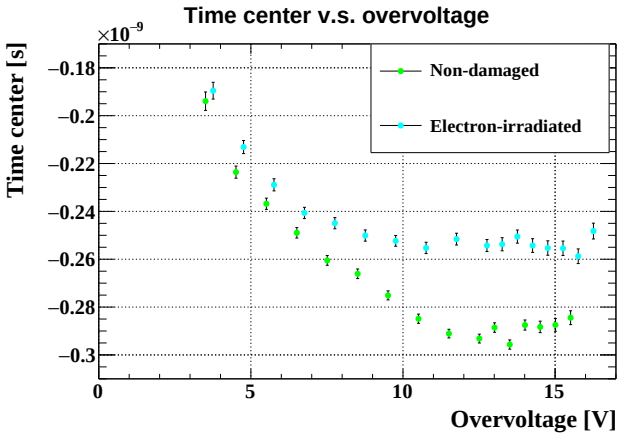

Figure 6.14: Overvoltage dependence of the time center. The green and cyan markers correspond to a SiPM array of four non-damaged and four type c SiPMs respectively. The number of SiPMs is set to four for technical reasons.

Due to this complex mechanism, which incorporates some parameters impossible to measure directly, a quantitative explanation for each pattern is not possible. However, the general difference between the standard and the reversed configuration can be explained as follows. When the hit point is at higher y, the rising part of the pulse is dominantly produced by the SiPMs closest to the readout (i.e. at higher y). These SiPMs yield smaller and slower signals in the standard configuration, and thus a larger time center is obtained with respect to the reversed configuration. The difference is smaller in pattern C as the damage difference is smaller.

On the other hand, when the hit point is at lower y, little scintillation light is collected by the SiPMs closest to the readout, and the signals from successive SiPMs are needed to generate the minimum signal fraction in the CF method. This weakens the effect of the gradient radiation damage, because, for instance, the damage level of the middle two SiPMs are the same in the two configurations. Thus, similar time center values are obtained in the two configurations.

6.5.3 Verification

The interpretation given above can be verified by performing a scan of the CF threshold used in the waveform analysis. If the above interpretation is correct, the position dependence should be sensitive to the CF threshold, and different position dependences should appear in the CF scan. Different behaviors should also be observed in the two configurations.

Fig. 6.15 and Fig. 6.16 show the same data as in Fig. 6.11, and Fig. 6.17 shows the same data as in Fig. 6.12, but analyzed with different CF values. In all damage patterns, including the one using a non-damaged SiPM array, the position dependence becomes less prominent as the CF value is raised. In addition to this, the standard configuration in each damage pattern show a somewhat reversed position dependence at higher CF values.

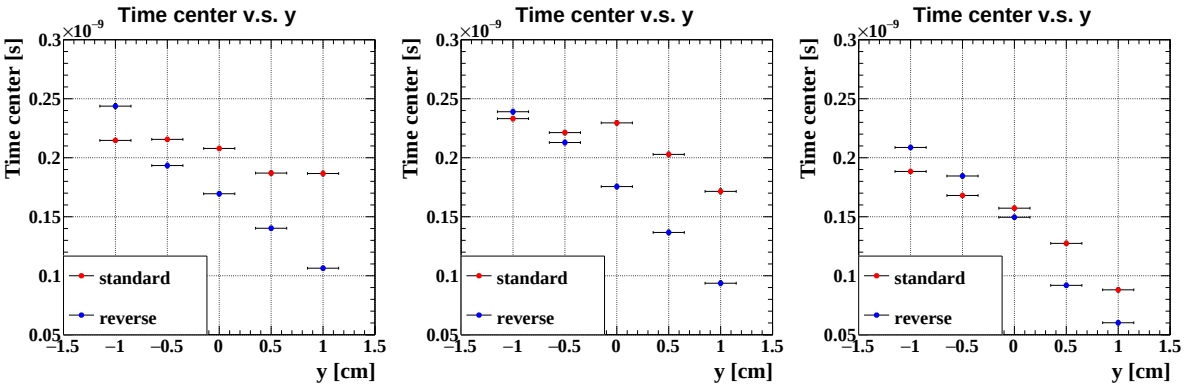

(a) Pattern A (b) Pattern B (c) Pattern C

Figure 6.15: y hit position dependence of the time center at $x = -4.25\,\mathrm{cm}$ in each damage pattern. The CF threshold is set to 50 %.

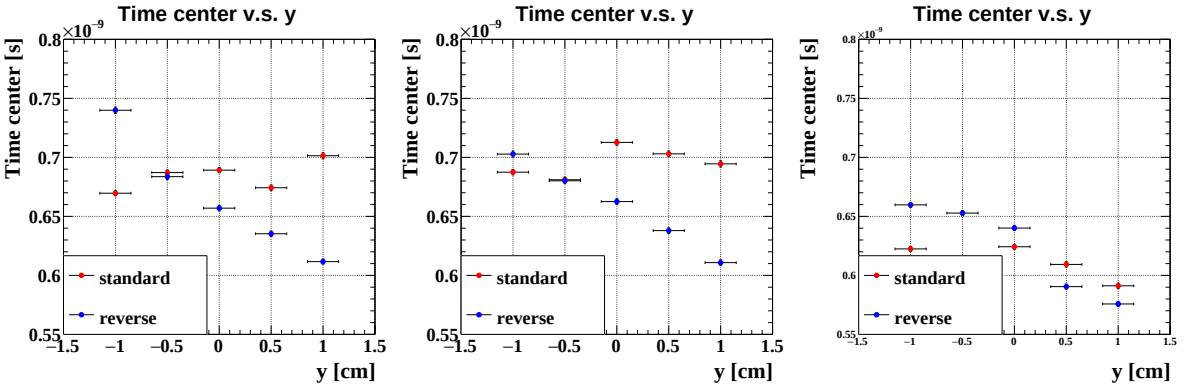

(a) Pattern A (b) Pattern B (c) Pattern C

Figure 6.16: y hit position dependence of the time center at $x = -4.25\,\mathrm{cm}$ in each damage pattern. The CF threshold is set to 80 %.

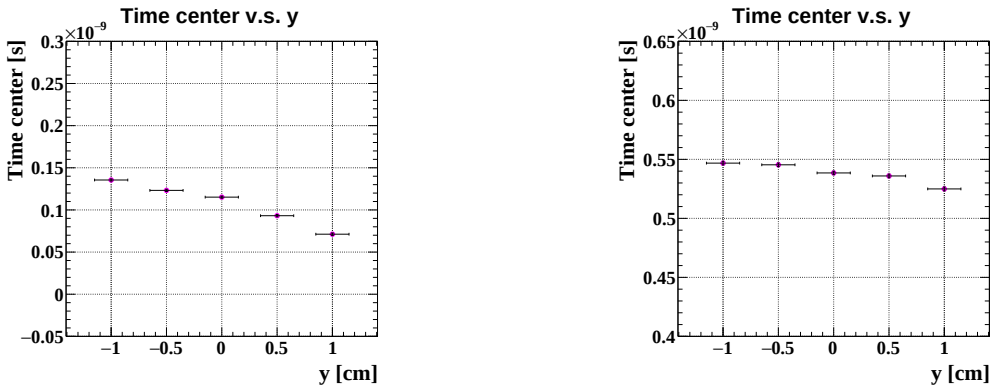

(a) 50 % threshold (b) 80 % threshold

Figure 6.17: y hit position dependence of the time center at $x = -4.25\,\mathrm{cm}$ for non-damaged SiPMs using different CF thresholds.

These behaviors can be explained by the low gain and the slow response of damaged SiPMs. In order to create a large fraction of the peak pulse, signals of latter SiPMs are needed in addition to the former ones. This effect should be more prominent in the standard configuration as the SiPMs closer to the readout have lower gain and slower time response. Therefore, even if the hit position is at higher y, the dominant signal can only be carried through the SiPMs at lower y. This causes the signals from higher y hit to be delayed than or comparable to those from lower y hit.

6.6 Effect on pTC performance

The intrinsic position-dependent time offsets found in this study, arises from a finite signal propagation time in the SiPM array. This effect had never been considered before, and therefore it was not implemented in MC simulations to evaluate the pTC resolution. Considering this effect, the single-pixel resolution is expected to worsen.

Furthermore, non-uniform damage to SiPMs were found to create additional position-dependent time fluctuations. The readout of the pTC pixels are in $-y$ direction, whereas the damage is higher at higher y. This corresponds to the reversed configuration in the above study, which means that position-dependent time offsets can be enhanced severely. This is expected to further worsen the pTC resolution.

6.6.1 Effect of cooling

One thing to note is that the effect of radiation damage found in this study cannot be suppressed by cooling the SiPMs. Operation at a lower temperature can reduce the dark noise, but the damage difference itself does not change. Therefore, the overvoltage variation of SiPMs in a series connection remains, and the position-dependent time offsets are unaffected.

Fig. 6.18 shows the I-V curves of SiPMs used in each damage pattern measured at 10 °C. Although the dark noise is reduced from the measurement at 30 °C (see Fig. 6.6), the differences in the I-V characteristics between differently-damaged SiPMs are retained.

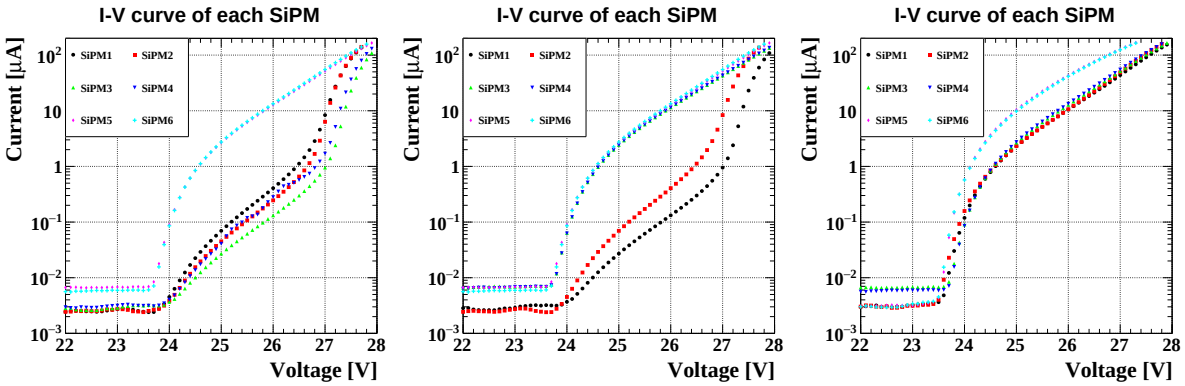

(a) Pattern A (b) Pattern B (c) Pattern C

Figure 6.18: I-V curves of SiPMs used in each damage pattern at 10 °C. SiPMs with less damage are labeled with younger numbers.

6.6.2 Effect of intrinsic time offsets

A MC simulation study was performed to see the effect of the intrinsic time offsets between SiPMs arising from the signal propagation time in the SiPM array. In MC simulation, the scintillation photons are tracked using Geant4 and the signal of each SiPM is formed by adding up the single photon waveforms at each photon arrival time. In the original MC setup, all the SiPM signals in a series connection were added up simultaneously. In this study, however, a fixed time offset was set between adjacent SiPMs when adding the signals from each SiPM. As this time offset cannot be measured directly, it must be estimated from the position dependence of the time center.

6.6.2.1 Reproduction of data

First, the y hit position dependence of the time center in the pTC was checked using the pER2017 data; the pER2017 data was chosen for its maximum number of readout channels (c.f. Tab. 4.4). The pTC tracking was used to exploit the position information.

Shown in Fig. 6.19 is the y hit position dependence of the time center in channel 1 for edge hits ($x_{\mathrm{hit}} < -5\,\mathrm{cm}$). The reconstructed hit position from the pTC tracking is used both to select edge hits, and to estimate y. The time center for each channel using the pTC data is defined as the Gaussian mean of

$$t^{\mathrm{ch1}}_{i_{\mathrm{hit}}} - t_{\mathrm{ave}} - TOF_{1i_{\mathrm{hit}}} \tag{6.1a}$$

$$t^{\mathrm{ch2}}_{i_{\mathrm{hit}}} - t_{\mathrm{ave}} - TOF_{1i_{\mathrm{hit}}} \tag{6.1b}$$

distribution respectively, where $t^{\mathrm{ch1}}_{i_{\mathrm{hit}}}$ and $t^{\mathrm{ch2}}_{i_{\mathrm{hit}}}$ are the signal detection times of the i_{hit}-th hit pixel in the two channels, and $TOF_{1i_{\mathrm{hit}}}$ is the TOF from the first to the i_{hit}-th hit pixel, and

$$t_{\mathrm{ave}} = \frac{1}{N_{\mathrm{hit}}} \sum_{i_{\mathrm{hit}}=1}^{N_{\mathrm{hit}}} (t_{i_{\mathrm{hit}}} - t_1 - TOF_{1i_{\mathrm{hit}}}), \tag{6.2}$$

where N_{hit} is the number of hit pixels in a track, and $t_{i_{\mathrm{hit}}}$ is the reconstructed hit time of the i_{hit}-th hit pixel in a track. A general inclination is clearly seen, confirming the existence of intrinsic time offsets between SiPMs. The sign of the inclination is different from that of the lab test result because the direction of the readout is opposite in the pTC. A similar position dependence in seen in channel 2 for $x_{\mathrm{hit}} > 5\,\mathrm{cm}$ hits.

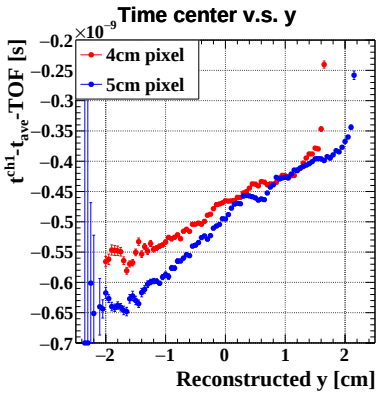

Figure 6.19: y hit position dependence of the time center for edge hits ($x_{\mathrm{hit}} < -5\,\mathrm{cm}$) in channel 1 using the pER2017 data. Hits for 4 cm and 5 cm pixels are analyzed separately, and shown in red and blue markers respectively.

Second, various MC-simulated datasets were produced, but with different time offsets between adjacent SiPMs. By performing the same analysis as above, the one that reproduces the y hit position dependence best contains the most plausible time offset. The input time offset should be different for 4 cm and 5 cm pixels as the circuit lengths differ, so the time offset in 5 cm pixels is fixed to be 5/4 of those in 4 cm pixels. Fig. 6.20 shows the position dependence obtained using MC simulation but with different time offsets between SiPMs. The position dependence becomes more prominent as the input time offsets are increased. Comparing these with Fig. 6.19, Fig. 6.20b best reproduces the data. As a conclusion, $\sim$ 60 / 75 ps time offsets roughly exist between adjacent SiPMs in 4 / 5 cm pixels.

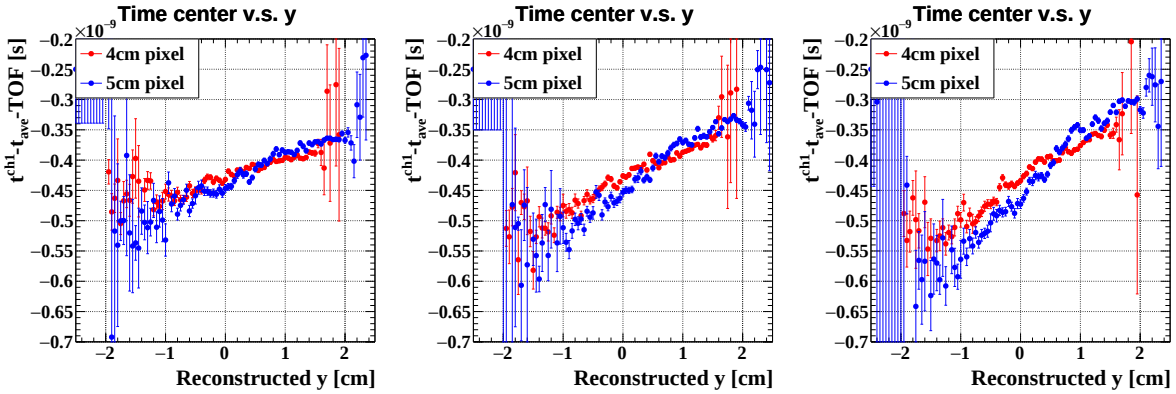

(a) 40 / 50 ps (b) 60 / 75 ps (c) 80 / 100 ps

Figure 6.20: y hit position dependence of the time center for edge hits ($x_{\mathrm{hit}} < -5\,\mathrm{cm}$) in channel 1 using MC-simulated data. The input time offsets between adjacent SiPMs in 4 / 5 cm pixels are denoted in each subcaption.

6.6.2.2 Effect on pTC resolution

The effect of the intrinsic time offsets between SiPMs on the pTC resolution was evaluated using MC simulation. First, the pTC resolution for events with each number of hit

pixels was obtained using MC datasets with no and the intrinsic time offsets implemented. The result is shown in Fig. 6.21. The event time resolution for N_{hit}-hit events is obtained from the standard deviation of

$$\begin{aligned}&\frac{1}{N_{\mathrm{hit}}}\sum_{i_{\mathrm{hit}}=1}^{N_{\mathrm{hit}}}\left((t^{\mathrm{rec}}_{i_{\mathrm{hit}}}-t^{\mathrm{MC}}_{i_{\mathrm{hit}}})-(TOF^{\mathrm{rec}}_{1i_{\mathrm{hit}}}-TOF^{\mathrm{MC}}_{1i_{\mathrm{hit}}})\right)\\&=\frac{1}{N_{\mathrm{hit}}}\sum_{i_{\mathrm{hit}}=1}^{N_{\mathrm{hit}}}(t^{\mathrm{rec}}_{i_{\mathrm{hit}}}-TOF^{\mathrm{rec}}_{1i_{\mathrm{hit}}}-t^{\mathrm{MC}}_{1})\end{aligned}\tag{6.3}$$

distribution where $t^{\mathrm{rec}}_{i_{\mathrm{hit}}}$ and $t^{\mathrm{MC}}_{i_{\mathrm{hit}}}$ are the reconstructed and MC-true hit time respectively of the i_{hit}-th hit pixel, and $TOF^{\mathrm{rec}}_{1i_{\mathrm{hit}}}$ and $TOF^{\mathrm{MC}}_{1i_{\mathrm{hit}}}$ are the reconstructed and the MC-true TOF from the first to the i_{hit}-th hit pixel. The pTC resolution is clearly deteriorated by the existence of time offsets between SiPMs. Note that adding different time offsets for 4 cm and 5 cm can create a systematic time offset between the two. However, this effect is removed offline when working out each resolution, as this systematic time offset is expected to be removed by the inter-pixel time calibration.

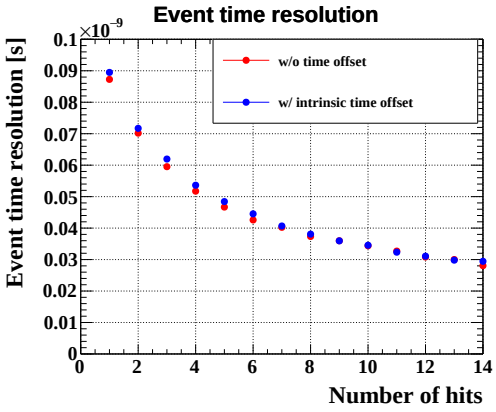

Figure 6.21: The pTC resolution for events with each number of hit pixels. MC datasets with 0 ps and 60 / 75 ps time offsets between SiPMs are used to obtain the red and blue plots respectively.

In order to compute the overall pTC resolution, the obtained resolution for each number-of-hit events must be summed up considering the probability of each number-of-hit events as was shown in Fig. 4.17. Calculating the appropriate weighted sum of these resolutions yield 38.1 ps and 38.7 ps respectively for the datasets with no and the intrinsic time offsets. In conclusion, the pTC resolution worsens by $\sim$ 2 % from the originally-expected value by considering the intrinsic time offsets between SiPMs.

6.6.3 Additional effect of radiation damage

The enhanced position dependence of the time center caused by a gradient radiation damage to SiPMs, is expected to further degrade the pTC resolution. However, the exact effect of the radiation damage is not easy to simulate, as it requires a precise evaluation

of the gradient damage level in each pixel, the overvoltage variation amongst SiPMs, the SiPM time response dependence on the overvoltage, etc. Therefore, we do not simulate the exact effect of the gradient damage, but imitate this effect by increasing the time offset between SiPMs.

First, we assume that the reversed configuration of pattern C in the previous study embodies a typical pTC channel after three years of data-taking. As the damage level in pattern C is comparable to the most damaged channel expected in the pTC, this assumption should be conservative enough. As the position dependence of the time center in a non-damaged sample (c.f. Fig. 6.12) is enhanced by a factor of ~ 1.8 in the reversed configuration of pattern C (c.f. Fig. 6.11c), it should be reasonable to set the time offsets in the MC simulation to be 1.8 of the original; namely 108 ps for 4 cm pixels and 135 ps for 5 cm pixels.

Fig. 6.22 shows the y hit position dependence of the time center for edge hits using a MC-simulated dataset with the enhanced time offsets implemented. The analysis procedure is exactly the same as that used to obtain the results in Fig. 6.20. The position dependence of the time center is clearly enhanced.

Calculating the pTC resolution for events with each number of hit pixels gives the magenta plots in Fig. 6.23. The enhanced time offsets clearly cause a further deterioration of the pTC resolution. By calculating the weighted sum of these resolutions, the overall pTC resolution is obtained to be 44.4 ps.

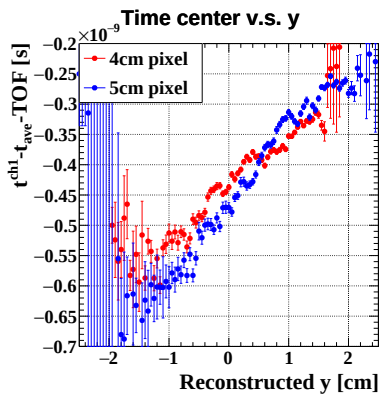

Figure 6.22: y hit position dependence of the time center for edge hits ($x_{\mathrm{hit}} < -5$ cm) in channel 1 using MC-simulated data with 108 / 135 ps time offsets implemented between adjacent SiPMs in 4 / 5 cm pixels.

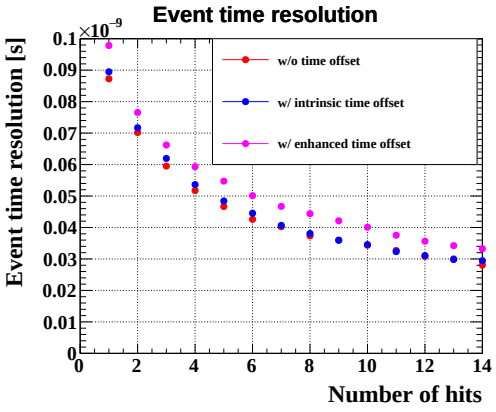

Figure 6.23: The pTC resolution for events with each number of hit pixels. The MC datasets with 0 ps, 60 / 75 ps and 108 / 135 ps time offsets between SiPMs are used to obtain the red, blue and magenta plots respectively.

Although the pTC resolution obtained here is rather conservative, as it assumes the maximum damage in all pixels, it is clear that a non-uniform radiation damage to SiPMs can significantly degrade the pTC resolution. The intrinsic time offsets, which had not been considered before, worsens the pTC resolution by $\sim 2\,\%$ from the expected, and the additional effect from radiation damage to SiPMs can cause a further $\sim 13\,\%$ deterioration of the pTC resolution. Therefore, in order to achieve the target performance, it is essential to bring out the maximum pTC resolution possible both from the hardware and software

point of views.

Chapter 7

Optimization of Operation and Analysis Parameters

The degradation of the pTC resolution due to radiation damage to SiPMs must be recovered somehow to achieve the target performance. This can partly be realized by optimizing the operation and analysis parameters. In this chapter is introduced new schemes to optimize the bias voltage applied to SiPMs and the CF parameter in the analysis.

7.1 Motivation

The conventional way to optimize the bias voltage and the CF parameter is to perform a scan of these parameters and find the value which yields the best time resolution. Ideally, the beam data should be used, but obtaining each channel time resolution with reasonable statistics requires a huge amount of beam data, and performing a scan on the hardware side is not realistic. Therefore, the beam data is only used for the CF scan, and the bias voltage scan is performed using the laser system (c.f. Fig 4.15).

However, optimizing the bias voltage using the laser data can cause some bias. We know that the optimal values of both the bias voltage and the CF parameter depend sensitively on the signal-to-noise ratio (S/N). This means that if the laser signal is considerably different from that of the signal positron, then this scheme does not give the true optimal value. One motivation here was to optimize the bias voltage with respect to the signal positron by somehow converting the laser bias voltage scan result.

Another motivation was to optimize the two parameters at each time point. As already mentioned, the optimal values of both these parameters depend on the S/N. This means that the optimal points are expected to shift as the dark noise is increased by the radiation damage to SiPMs. In the conventional method, a time-by-time optimization is possible for the CF parameter, but not for the bias voltage as the laser data is needed at each time point. Therefore, by developing a scheme to optimize the two parameters at each time point, we would always be able to bring out the maximal pTC resolution.

The last idea for improvement was to optimize these parameters for each channel independently. In the conventional method, the overvoltage or the CF value which yields the best average resolution of all channels was chosen as the optimal. However, the speed of the dark noise increase should differ from channel to channel, as the radiation

damage to SiPMs depend on the global pixel position. Therefore, considering the long-term operation, a channel-by-channel optimization of both these parameters should give a better resolution.

The aim of this study, therefore, was to develop fixed channel-by-channel HV and CF optimization schemes with respect to the signal positrons, which would require no dedicated DAQ, but determine the optimal values solely from the observed noise level at a particular time. The maximal pTC resolution can then be extracted at each time point both from the hardware and software side.

7.2 Measurement

7.2.1 SiPMs

The SiPMs used in this study were the type c SiPMs in Tab. 6.1. The irradiation of electrons to these SiPMs were conducted in the lab in four steps. The dose level at each irradiation step is summarized in Tab. 7.1.

Table 7.1: Dose level of type c SiPMs at each irradiation step.

Damage step	Hours of electron irradiation	Dose level equivalent to 1 MeV neutrons
Step 0	0 hours	$0\,/\mathrm{cm}^2$
Step 1	70 hours	$7.5 \times 10^8\,/\mathrm{cm}^2$
Step 2	140 hours	$1.5 \times 10^9\,/\mathrm{cm}^2$
Step 3	210 hours	$2.25 \times 10^9\,/\mathrm{cm}^2$
Step 4	280 hours	$3 \times 10^9\,/\mathrm{cm}^2$

7.2.2 Measurement

A bias voltage scan was performed at each irradiation step. The measurement setup used for the bias voltage scan was the same as the one used in chapter 6 except for the SiPM array. While SiPMs with different damage levels were used in the previous measurement, the bias voltage scan here was performed using six SiPMs at the same irradiation step (i.e. with the same damage level). This is because our interest was in the total dark noise increase, and the difference in the behavior of each SiPM was irrelevant. The other parts of the setup were exactly the same as in chapter 6; the pixel assembly setup, the radiation source, and the trigger counter are all the same. The bias voltage scan was performed with the thermal chamber set both to 10 °C and 30 °C, except at damage step 0 where the measurement was only performed at 30 °C.

7.3 Bias voltage optimization

7.3.1 General idea

We know empirically that the time resolution has a strong correlation with the S/N. In fact, that is why an optimal bias voltage exists from the time resolution viewpoint.

The signal of SiPMs increase almost linearly with the overvoltage, as the gain has a linear correlation with the overvoltage[1]. On the other hand, although the electronics noise is expected to be constant, the SiPM noise increases drastically with the overvoltage. As a consequence, the S/N is maximized at a particular bias voltage, and an optimal bias voltage is produced.

Another factor that affects the S/N, apart from the overvoltage, is the radiation damage to SiPMs. This is not expected to affect the signal size, but the dark noise is increased, so the S/N changes accordingly. Thus, the optimal overvoltage is expected to shift lower with the accumulation of radiation damage, as schematically shown in Fig. 7.1.

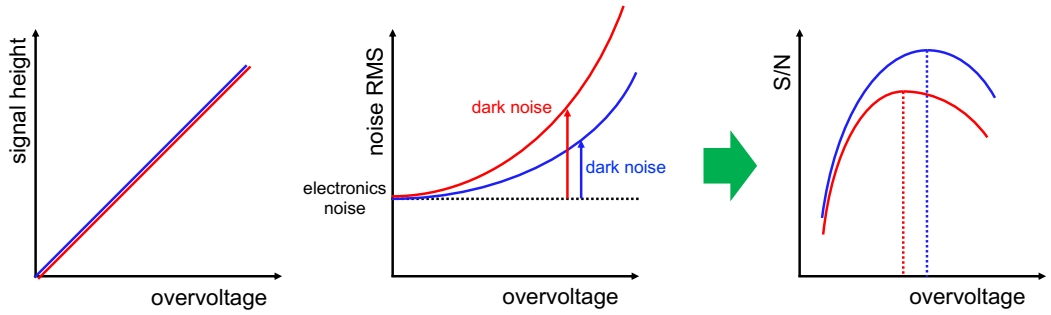

Figure 7.1: A schematic view of the how the optimal bias voltage is determined. The red lines show the case with higher radiation damage with respect to the blue lines.

The idea for the new HV optimization scheme is as follows. We assume that the time resolution is maximized when the S/N is maximized. If we know the overvoltage dependence of both the signal and the noise, then the bias voltage at which the maximum S/N is given can be calculated mathematically. However, as already mentioned, the noise curve in Fig. 7.1 shifts over time. Therefore, in order to realize this scheme, we must be capable of predicting the noise curve at a particular time from the observed noise level, assuming that the electronics noise is stable. This is, in principle, possible if the noise curve can be expressed by a simple function with only one degree of freedom. The feasibility of this scheme was checked in this study, using the bias voltage scan data at different irradiation steps.

7.3.2 Understanding of the time resolution

In order to confirm our understanding of the time resolution, its correlation to various parameters was checked. Fig. 7.2 shows the relation between the S/N and the time resolution. The S/N here is defined as the mean of the (pulse height)/(noise root mean square (RMS)) distribution. As expected, setups with higher S/N yield better time resolutions.

[1]The PDE also has an overvoltage dependence but it is saturated in the operation region.

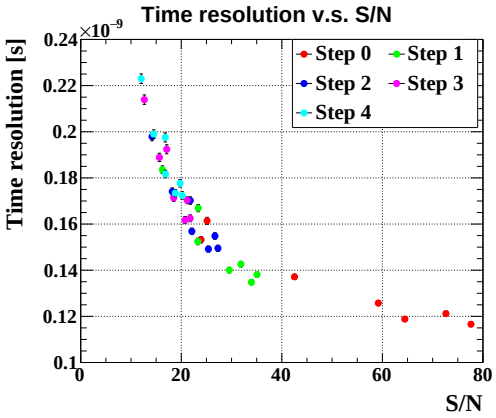

Figure 7.2: Relation between the S/N and the time resolution. The bias voltage scan data at 30 °C with different damage levels is used.

In addition, it was found that the noise-to-signal ratio (N/S), which is defined here as the inverse of the S/N, has a linear and much clearer correlation with the time resolution. This is shown in Fig. 7.3a. However, the distribution in Fig. 7.3a is relatively broad, suggesting some other effect on the time resolution other than the N/S.

This can be understood by checking the bias voltage dependence of this result as shown in Fig. 7.3b. It is clear that the plots at each bias voltage is in a clear linear correlation, and that a better time resolution is achieved at higher bias voltages if the N/S is fixed. This can be speculated to be the caused by less deviation in the SiPM charge collection time at higher overvoltages.

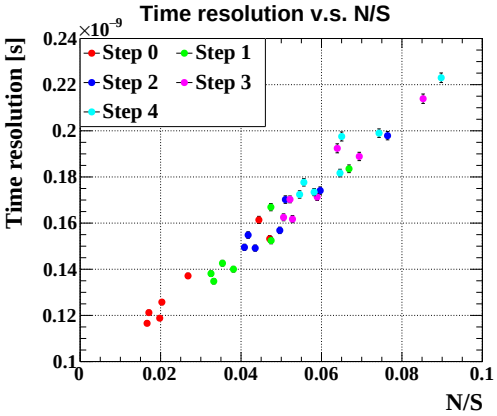

(a) Different marker colors represent different damage levels.

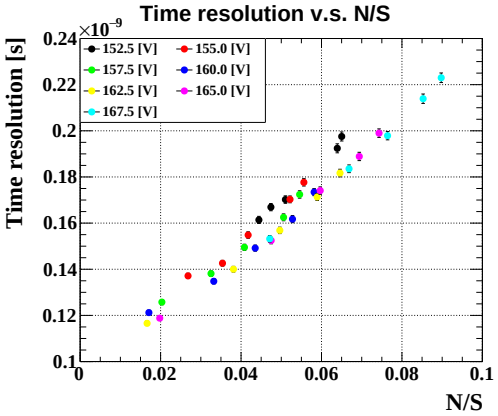

(b) Different marker colors represent different bias voltages.

Figure 7.3: Relation between the N/S and the time resolution. The bias voltage scan data at 30 °C with different damage levels is used.

Thus, the time resolution of a pixel is assumed to be determined by two factors; the overvoltage, which sets some intrinsic time resolutions of SiPMs, and the N/S, which linearly worsens the time resolution from the intrinsic value. However, in the actual pTC in the πE5 area, the noise level is generally larger than the lab environment, so the time

resolution is expected to be dominated by the N/S factor. Therefore, we can neglect the overvoltage-dependent factor and simply search for the bias voltage which yields the minimal N/S.

7.3.3 Bias voltage dependence

First, the overvoltage dependence of the signal height was checked, which is shown in Fig. 7.4. As expected, the signal increases linearly with the overvoltage, and the radiation damage to SiPMs does not affect the signal size. Although the SiPMs are equally damaged in this measurement, this is expected hold true for the non-uniform damage case too, as the total bias voltage to SiPMs does not change.

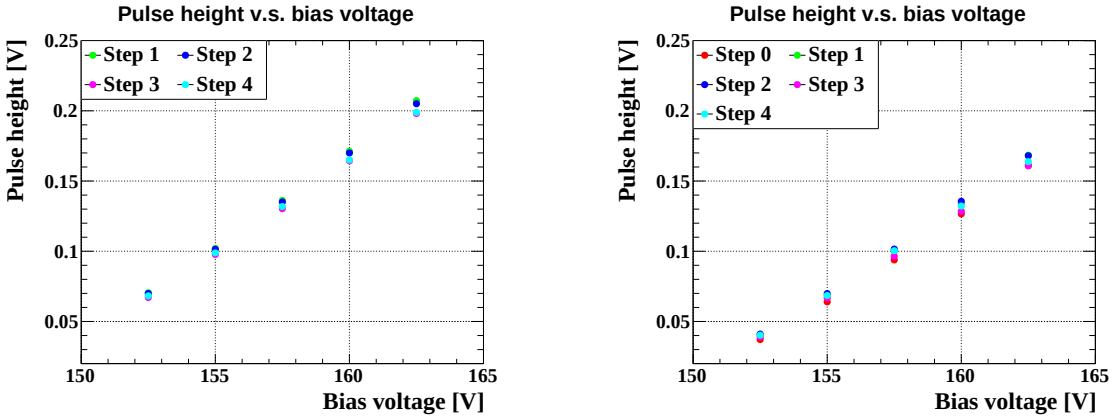

(a) 10 °C (b) 30 °C

Figure 7.4: Bias voltage dependence of the signal height at different damage levels.

Next, the overvoltage dependence of the noise RMS was checked, which is shown in Fig. 7.5. The general dependence on the overvoltage and the damage level is as was assumed in Fig. 7.1. Our goal is to find a function that fits the plots of all damage steps by changing a single parameter, and then the whole noise curve can be estimated from the observed noise level at a particular applied voltage.

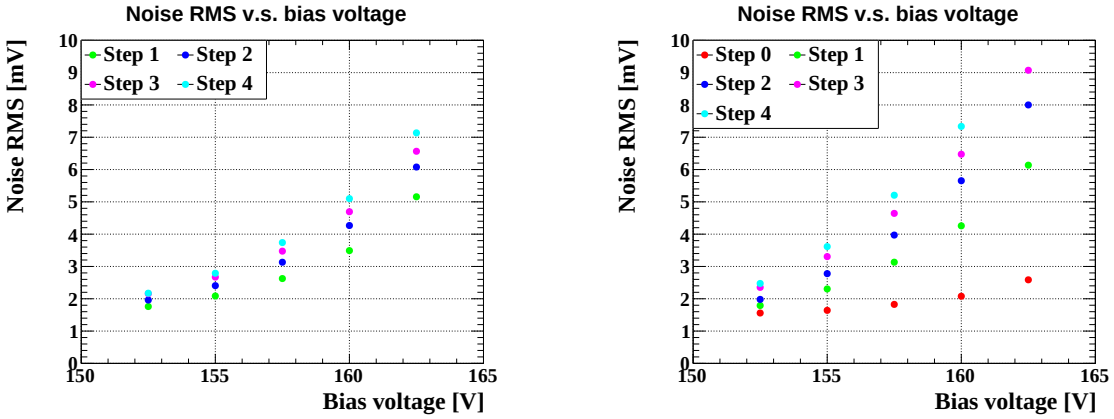

(a) 10 °C (b) 30 °C

Figure 7.5: Bias voltage dependence of the noise RMS at different damage levels.

Assuming, that the noise is composed of two components, namely the electronics noise and the SiPM noise, then the noise RMS should be expressed as the square root of the squared sum of these two;

$$N = \sqrt{N_{\mathrm{SiPM}}^2 + N_{\mathrm{elec}}^2} \tag{7.1}$$

where N is the observed noise RMS, and N_{SiPM} and N_{elec} are the noise deriving from the SiPMs and the electronics respectively. N_{elec} is a constant which does not change with the bias voltage, whereas N_{SiPM} must be an increasing function of the overvoltage and is expected to converge to zero at the breakdown voltage.

Several such functions were tested, and it was found that at 10 °C, which is the operation temperature of the pTC, a cubic function depicts the SiPM noise very well:

$$N_{\mathrm{SiPM}} = C \times (V - V_{\mathrm{bd}})^3 \tag{7.2}$$

where C is a constant that changes with the damage level, V is the applied voltage, and V_{bd} is the breakdown voltage of the SiPM array. This is shown in Fig. 7.6. Although N_{elec} was a free parameter in the fit, it differed very little in the four steps. This difference is assumed to derive simply from the difference in the noise situation in each measurement. In any case, the difference is negligibly small ($\sim 0.3\,\mathrm{mV}$), and assuming the N_{elec} to be constant should not be a problem.

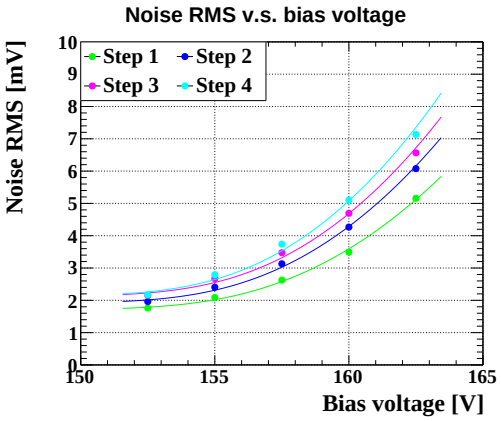

Figure 7.6: Bias voltage dependence of the noise RMS at different damage levels at 10 °C fitted with $N = \sqrt{C^2(V - V_{\mathrm{bd}})^6 + N_{\mathrm{elec}}^2}$ where V_{bd} is fixed. Each fit function corresponds to the markers of the same color.

In this strategy, therefore, only C changes with the damage level, and the other parameters do not change over time. Thus, once V_{bd} and N_{elec} are obtained, the noise RMS at an arbitrary bias voltage can be obtained simply from the observed noise level. This, in principle, allows a channel-by-channel optimization of the pTC bias voltage at any damage level.

7.3.4 Application to pER2019 data

7.3.4.1 Optimization procedure

To apply the optimization scheme to the pTC, a bias voltage scan data of 256 channels was obtained using the laser system. The bias voltage scan was performed in steps of 0.5 V from −15 V to +1 V of the nominal HV in the pER2019.

The procedures for the bias voltage optimization for each channel is as follows:

1. Perform an I-V measurement and obtain the breakdown voltage.

2. Using the obtained breakdown voltage, fit the bias voltage v.s. noise RMS relation with the function discussed above.

3. Obtain the dependence of the signal height on the bias voltage during the laser bias voltage scan.

4. Check the signal size in the beam data at a particular bias voltage, and convert the bias voltage dependence of the signal height to meet the beam data.

5. From the two functions, calculate the bias voltage that minimizes the N/S factor.

In this way, the optimal bias voltage can be obtained independently of the laser signal size. The I-V measurement for all channels can be performed simultaneously using the WDBs.

Fig. 7.7 shows the relation between the bias voltage and the signal height for some typical channels obtained in the bias voltage scan. They are clearly fitted well with linear functions. Fig. 7.8 shows the relation between the bias voltage and the noise RMS for the same channels, fitted with the function discussed above. The cubic function in Eq. (7.2) seems to depict the bias voltage dependence of the SiPM noise in the pTC very effectively.

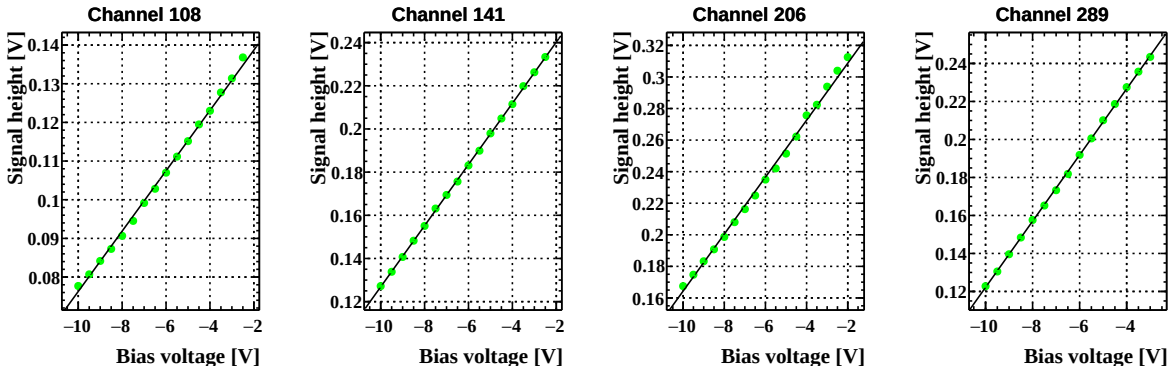

Figure 7.7: Bias voltage dependence of the signal height for some typical channels in the pTC bias voltage scan using the laser system. The horizontal axis is taken with respect to the nominal HV in the pER2019. Each plot is fitted with a linear function.

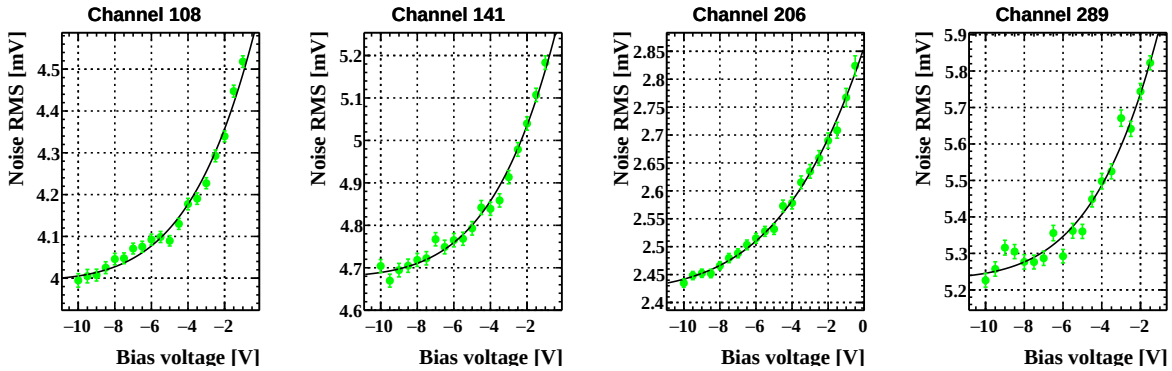

Figure 7.8: Bias voltage dependence of the noise RMS for some typical channels in the pTC bias voltage scan using the laser system. The horizontal axis is taken with respect to the nominal HV in the pER2019. Each plot is fitted with the function discussed in the text.

7.3.4.2 Effect on pTC resolution

In order to verify the effect of this optimization scheme, the pTC time resolution before and after this optimization must be checked. This has not been performed yet, as we have had any DAQ time with the muon beam after this scheme was developed. Therefore, the verification of this optimization method will be left for future studies, although we expect it to be effective.

7.4 Constant fraction optimization

7.4.1 General idea

If the waveform is always the same or only different in the voltage scale, then the CF method should always give the same timing. In reality, however, both the leading edge and the peak point fluctuate event by event, as they are determined by a complex combination of the number of scintillation photons, their optical paths, the time response of SiPMs, the baseline fluctuation, and so on.

However, an optimal CF value exists which gives the best time resolution. This is determined by the balance between the time fluctuation of the leading edge and the peak point. This effect is schematically shown in Fig. 7.9. When the noise level is low, the fluctuation of the baseline is small enough, and therefore, the time fluctuation of the leading edge is kept small. However, the peak time is affected by a number of probabilistic factors and the fluctuation is relatively large. Therefore, a lower CF threshold gives a better time resolution. On the other hand, when the noise level is high, the fluctuation of the baseline becomes large. This leads to a comparable or larger time fluctuation of the leading edge with respect to the peak time, and a higher CF value is preferred. This explains how the optimal CF value depends sensitively on the S/N.

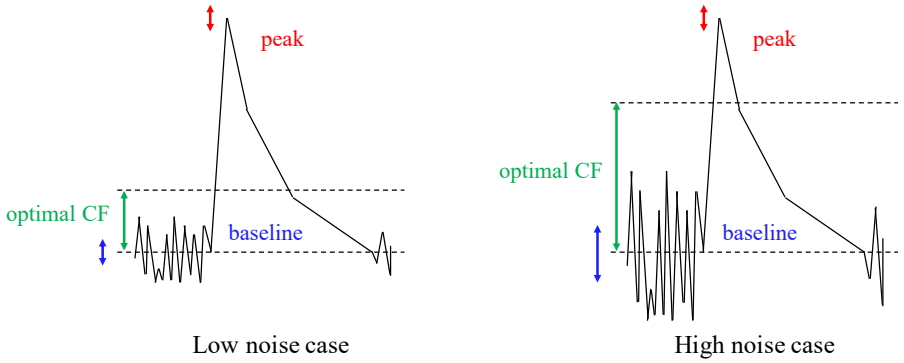

Figure 7.9: A schematic drawing showing the concept of the CF optimization.

7.4.2 Dependence on the noise level

A CF scan was performed in steps of 0.05 from 0.15 to 0.6 for the data at each bias voltage in each damage step. Fig. 7.10 shows the dependence of the time resolution on both the bias voltage and the CF value. The optimal CF clearly shifts higher as the damage level increases, confirming our understanding of the CF method.

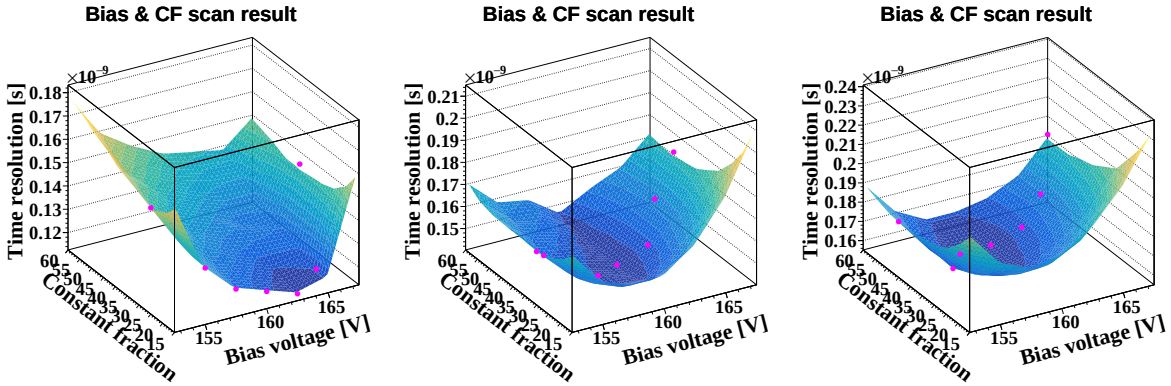

(a) Damage step 0 (b) Damage step 2 (c) Damage step 4

Figure 7.10: Bias voltage and CF dependence of the time resolution at 30 °C at different damage levels. The magenta markers show the optimal CF values at each bias voltage.

If our understanding is correct, the optimal CF value should depend sensitively on the S/N. To confirm this, the correlation between the optimal CF value and various parameters was checked. In fact, it was found to have a moderately clear, linear correlation with the N/S as demonstrated in Fig. 7.11.

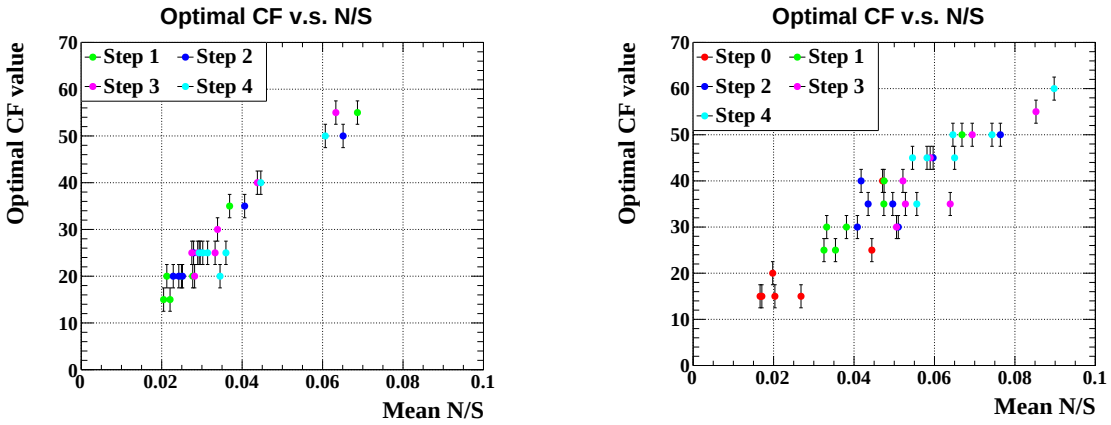

(a) 10 °C (b) 30 °C

Figure 7.11: Relation between the N/S and the optimal CF value at different temperatures.

Using this correlation, it is possible to optimize the CF value channel by channel from the observed noise RMS at a particular time and the typical signal height. It is also obvious from Fig. 7.10 that such an optimization is important in order to suppress the resolution degradation due to the dark noise increase.

7.4.3 Application to pER2019 data

7.4.3.1 Optimization procedure

To apply the optimization scheme to the pTC, the same laser bias voltage scan data as in 7.3.4 is used. The reason for using the bias voltage scan data is that it yields a variety of N/S values and its correlation with the optimal CF value should be seen clearly.

The procedures for the CF optimization for each channel is as follows:

1. Perform a CF scan to the bias voltage scan data.
2. Obtain the CF value which yields the best time resolution for each data point.
3. Fit the N/S v.s. optimal CF relation with a linear function.
4. Obtain a typical N/S using the beam data.
5. Calculate the corresponding optimal CF using the linear function.

In this way, the optimal CF value can be obtained independently of the laser signal size.

Fig. 7.12 shows the correlation between the N/S and the optimal CF in the obtained laser data for some typical channels. The linear correlations can be seen clearly, and the correlation seems to differ from channel to channel, indicating that a channel-by-channel optimization is effective even without considering the radiation damage effect. Although the reason for the channel-by-channel difference has not been investigated yet, it is assumed to be caused by the difference in the SiPM characteristics, such as the rise time and the correlated noise probability. In any case, the linear function for each channel was obtained.

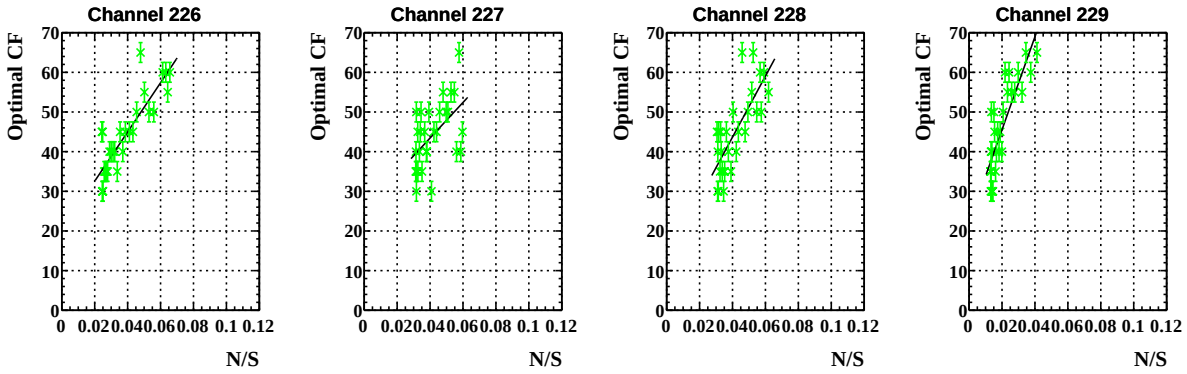

Figure 7.12: N/S dependence of the optimal CF value for some typical channels using pTC bias voltage scan data using the laser system.

Next, using the pER2019 beam data, a typical N/S factor was obtained for each channel. Combining these with the obtained linear functions, the optimal CF was calculated for each channel. The distribution of the obtained optimal CF values are shown in Fig. 7.13. The distribution is broad, indicating the effectiveness of channel-by-channel optimization. Note that this method can yield optimal values larger than 1, in which case the CF value should be set to 1.

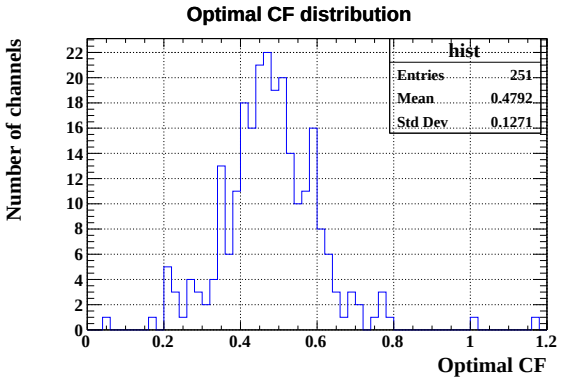

Figure 7.13: Distribution of the obtained optimal CF values. The number of entries is smaller than the 256 readout channels due to the existence of some dead channels.

7.4.3.2 Effect on pTC resolution

In order to verify the effect of this optimization scheme, the time resolutions of each pixel before and after the optimization were compared. The same beam data used to obtain the N/S factors is used. To obtain the time resolution of each pixel the 2-hit analysis method was used, in which the time resolution is obtained from the hit time difference distribution in fixed combinations of adjacent pixels.

Fig. 7.14 shows the obtained time resolution of each pixel before and after the optimization. Pixels with ID from 304 to 432 were read out in the pER2019, but the resolutions for the first 16 pixels are not shown, as they do not have the coupling pixels for the 2-hit analysis. The CF parameter before the optimization was set to 20 % for all

channels, which was a value obtained in the pER2017 using the conventional optimization scheme in steps of 10 %. The average time resolution is improved by ~ 3 %, and thus, the effectiveness of this optimization scheme is verified.

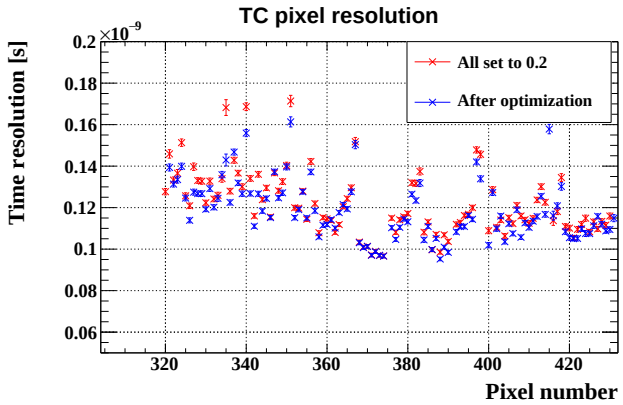

Figure 7.14: Time resolution of each pixel obtained using the 2-hit analysis method before (red) and after (blue) the optimization.

One thing to note is that the optimization scheme was found not to work for pixels with type II and type III SiPMs in Tab. 4.2. That is, the time resolutions obtained with the 2-hit analysis method was worse after the optimization than before. Therefore, the CF values for these pixels are set to the original 20 % for these pixels to obtain Fig. 7.14. The reason for this is unknown, but the only possible explanation is that some systematic difference exists between the laser and beam data which affects the new SiPMs more.

Part III

Analysis Algorithm and Performance Evaluation of pTC

Chapter 8

Offset Correction Algorithm

In this chapter is introduced a method to correct the position dependence of the time center in the offline analysis. The method and the effect of the correction on the pTC resolution is discussed using MC simulation.

8.1 Motivation

It was found that the intrinsic time offsets between SiPMs worsen the pTC resolution by $\sim 2\,\%$, and that a further $\sim 13\,\%$ degradation is expected by the non-uniform radiation damage to SiPMs which essentially enhances these time offsets. As this cannot be suppressed by cooling or any other hardware measures, this must be compensated on the software side.

The most obvious and direct way to compensate this effect is to correct the position-dependent time offsets in the offline analysis. The hit position information is available from the CDCH (or pTC) tracking, and therefore, the position dependence can be calculated. Using the obtained dependence, the offset can be subtracted depending on each reconstructed hit position.

8.2 Simulated sample

In order to study this effect, MC-simulated data is used. One motivation for using MC simulation rather than the actual data is that an arbitrary time offset can be implemented between the SiPMs. Another is that the CDCH track information is available in the MC, whereas it is not in the real data due to a limited number of readout channels.

Three datasets, each with $\sim 450,000$ signal positron events, were produced using MC simulation. In each dataset is implemented the intrinsic time offsets (60 / 75 ps), the enhanced time offsets (108 / 135 ps), and no time offsets (0 / 0 ps) between adjacent SiPMs in 4 / 5 cm pixels. The main purpose of this study was to check the feasibility of the correction, and therefore the Michel positron background is not included in the simulation.

8.3 Correction using MC values

8.3.1 Position dependence

Fig. 8.1 shows the MC hit position dependence of the time center for each channel for 4 cm pixels using the dataset with the intrinsic time offsets. The time center for each channel using MC data is defined as the Gaussian mean of

$$t^{\mathrm{ch1}}_{i_{\mathrm{hit}}} - t^{\mathrm{MC}}_{i_{\mathrm{hit}}} \tag{8.1a}$$

$$t^{\mathrm{ch2}}_{i_{\mathrm{hit}}} - t^{\mathrm{MC}}_{i_{\mathrm{hit}}} \tag{8.1b}$$

distribution respectively, where $t^{\mathrm{ch1}}_{i_{\mathrm{hit}}}$ and $t^{\mathrm{ch2}}_{i_{\mathrm{hit}}}$ are the signal detection times of the i_{hit}-th hit pixel in the two channels, and $t^{\mathrm{MC}}_{i_{\mathrm{hit}}}$ is the MC-true hit time of the i_{hit}-th hit pixel. The propagation time of the scintillation light in x direction dominates the time offset, but for edge hits close to the readout channel, clear position dependences in y direction can also be seen. Slightly enhanced but similar dependences are seen in 5 cm pixels.

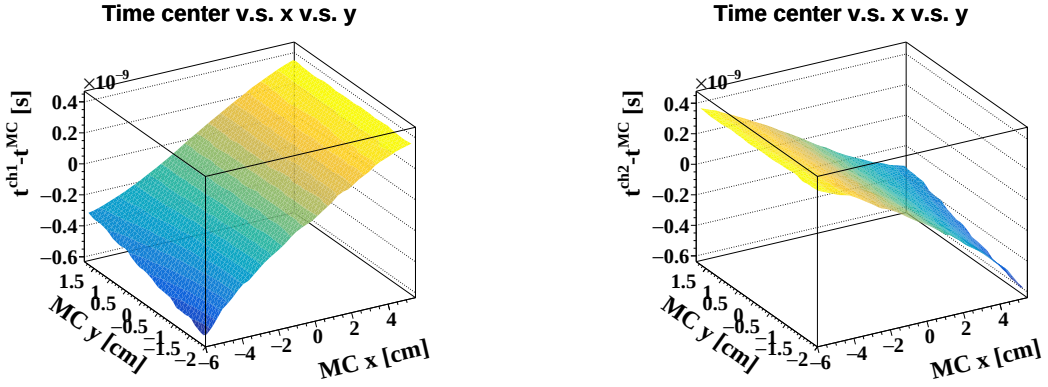

(a) Channel 1 (b) Channel 2

Figure 8.1: MC hit position dependence of the time center for 4 cm pixels with intrinsic time offsets.

Fig. 8.2 shows the same position dependence of the time center after correcting the offset in x direction using the MC-true x hit position. That is, the Gaussian means of

$$t^{\mathrm{ch1}}_{i_{\mathrm{hit}}} - t^{\mathrm{MC}}_{i_{\mathrm{hit}}} - \frac{\frac{L}{2} + x^{\mathrm{MC}}_{i_{\mathrm{hit}}}}{v_{\mathrm{eff}}} \tag{8.2a}$$

$$t^{\mathrm{ch2}}_{i_{\mathrm{hit}}} - t^{\mathrm{MC}}_{i_{\mathrm{hit}}} - \frac{\frac{L}{2} - x^{\mathrm{MC}}_{i_{\mathrm{hit}}}}{v_{\mathrm{eff}}} \tag{8.2b}$$

distributions at each MC hit position are plotted respectively, where $L(= 12\,\mathrm{cm})$ is the length of the pTC pixel, $x^{\mathrm{MC}}_{i_{\mathrm{hit}}}$ is the MC x hit position in the pixel for the i_{hit}-th hit, and v_{eff} is the effective velocity of the scintillation light. A clearer y position dependence of the time center can be seen compared to Fig. 8.1. As the time offset in x direction is taken into account in the original hit reconstruction, these are the additional time offsets that must be corrected in the offline analysis. Similar dependences are seen in 5 cm pixels.

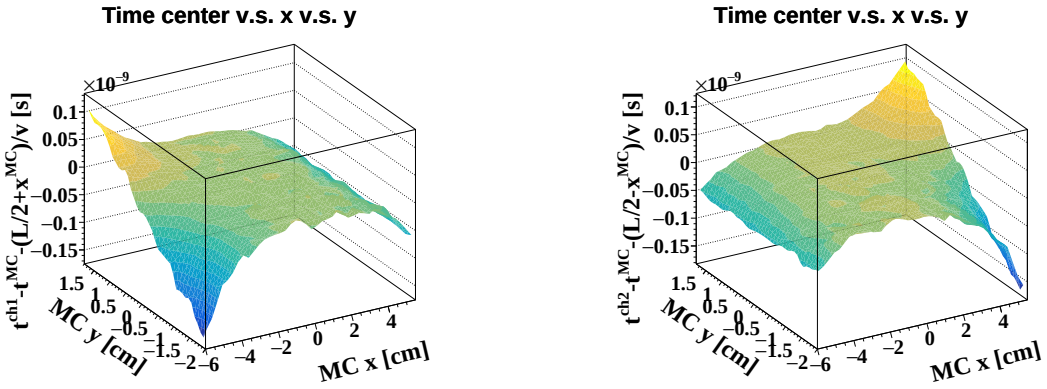

(a) Channel 1 (b) Channel 2

Figure 8.2: MC hit position dependence of the time center for 4 cm pixels with intrinsic time offsets after correcting the offset in x direction.

The same position dependence of the time center for 4 cm pixels but using the dataset with the enhanced time offsets is shown in Fig. 8.3. The time offsets are clearly enhanced.

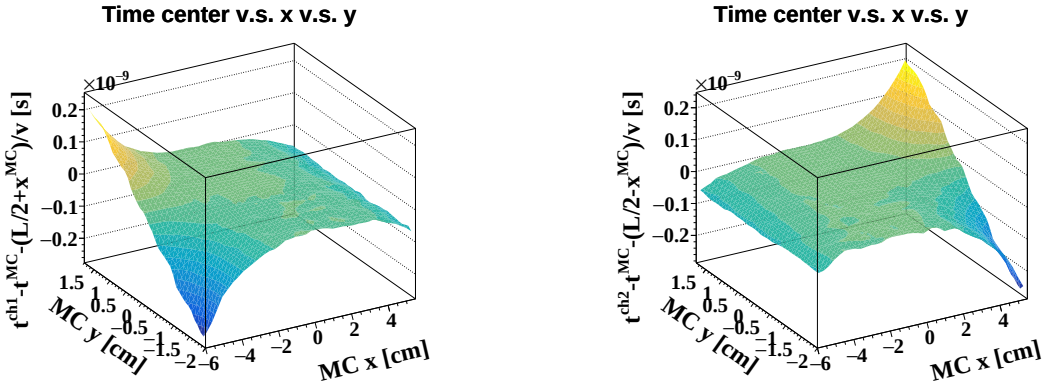

(a) Channel 1 (b) Channel 2

Figure 8.3: MC hit position dependence of the time center for 4 cm pixels with enhanced time offsets after correcting the offset in x direction.

8.3.2 Correction

The degradation of the pTC resolution in the enhanced time offset case occurs via two mechanisms:

- The bluntening of the waveform.
- The position dependence of the time center.

The former leads to larger fluctuations in the time obtained in each channel in the waveform analysis. The latter worsens each pixel hit time, as large time fluctuations occur according to the hit position of the particle.

There is no way to cancel out the former effect, as we cannot separate the signals from each SiPM. The degradation caused by the latter effect is the one we can wipe out with our correction. The maximal extent to which we can recover the resolution can be checked by performing the correction using MC truth values for the hit positions. It is also possible from this correction to distinguish the effect of the two mechanisms on the pTC resolution.

Using the position dependence obtained above, the signal detection time in each channel was corrected according to the MC hit position in a pixel. After the offset correction, the obtained time of the two channels are combined to reconstruct the hit time, which are further combined to obtain the overall positron time. Thus, the pTC resolution for events with each number of hit pixels was obtained both with and without the offline offset correction, which are shown in Fig. 8.4. Eq. 6.3 is used to obtain each resolution. The correction is clearly effective, especially in the case of the enhanced time offsets.

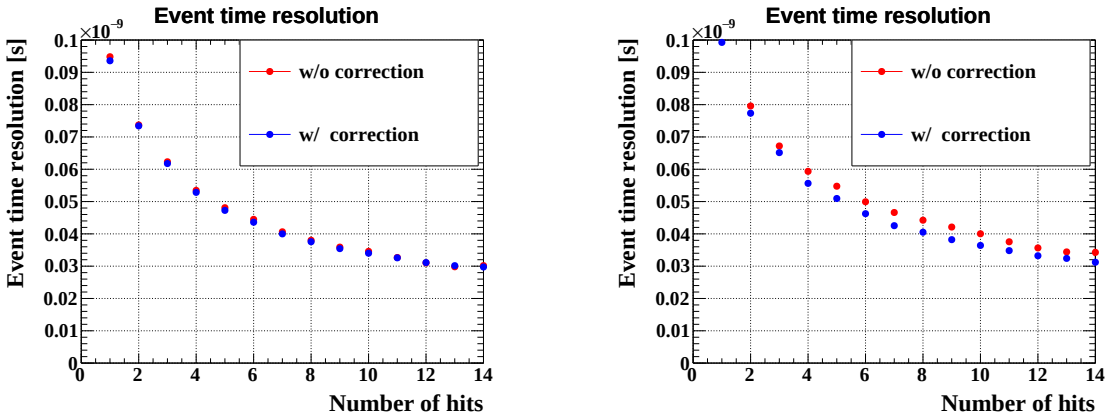

(a) Intrinsic time offset (b) Enhanced time offset

Figure 8.4: The pTC resolution for events with each number of hit pixels for different datasets. The blue and red markers correspond to with and without the offset correction using MC values respectively.

Using these resolutions, the overall pTC resolution was calculated for each dataset. The result is summarized in Tab. 8.1. The correction also works for the dataset with no time offsets, as some small position dependence exists. The degradation of the pTC resolution after the correction indicates the effect from the waveform bluntening. This is, however, relatively small compared to the overall degradation, suggesting that the degradation caused by the position dependence of the time center is indeed dominant. Looking at the bright side, however, this means that the pTC resolution can be recovered to a large extent if we have enough position resolution to effectively perform the offset correction.

Table 8.1: The effect of the offline time offset correction using MC hit positions in each dataset.

Time offset	pTC resolution	
	Without correction	With correction
No time offset	38.1 ps	37.6 ps
Intrinsic time offset	38.7 ps	38.2 ps
Enhanced time offset	44.4 ps	40.9 ps

8.4 Correction using reconstructed values

8.4.1 Position resolutions

The correction using MC values turned out to be highly effective. However, this assumes an infinite hit position resolution, and the actual extent to which we can recover the time resolution is likely to be limited by the x and y position resolutions of the reconstructed hit point.

Fig. 8.5 and Fig. 8.6 show the x and y resolution respectively obtained in the two tracking methods. The horizontal axis shows the hit index, which is the number of the hit pixel in a track counting from the first. The MC dataset with no time offsets is used, and each resolution is obtained from the standard deviation of the distribution of the hit position difference between the reconstructed and the MC truth.

The x hit position resolution in the CDCH tracking is worse for hits at higher hit indices due to multiple scattering. This is not the case in y direction, as y estimation in the pTC tracking is used as initial values for the CDCH track fit and the y estimation is better for hits at higher hit indices. In any case, averaged resolutions of ~ 5 mm and ~ 6 mm are achieved for x and y position respectively using the CDCH tracking. The pTC tracking yields slightly worse position resolutions.

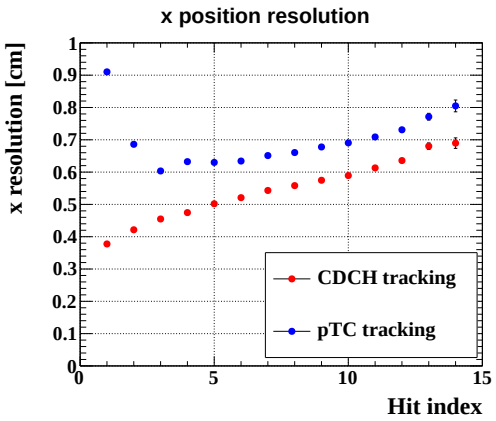

Figure 8.5: x resolution at each hit index in the CDCH tracking and the pTC tracking.

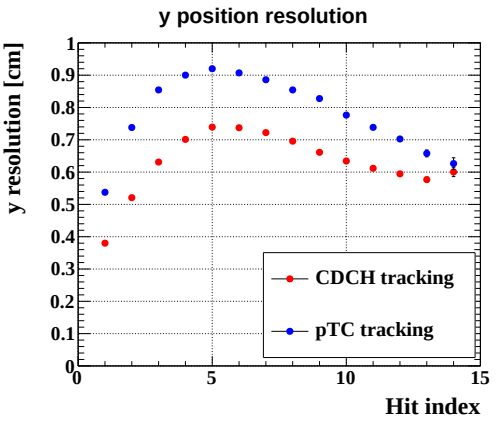

Figure 8.6: y resolution at each hit index in the CDCH tracking and the pTC tracking.

8.4.2 Position dependence

The hit position dependence of the time center using reconstructed hit positions is shown in Fig. 8.7. The time offset in x direction is corrected beforehand. In explicit forms, the Gaussian means of

$$t^{\mathrm{ch1}}_{i_{\mathrm{hit}}} - t_{\mathrm{ave}} - TOF^{\mathrm{rec}}_{1i_{\mathrm{hit}}} - \frac{\frac{L}{2} + x^{\mathrm{rec}}_{i_{\mathrm{hit}}}}{v_{\mathrm{eff}}} \tag{8.3a}$$

$$t^{\mathrm{ch2}}_{i_{\mathrm{hit}}} - t_{\mathrm{ave}} - TOF^{\mathrm{rec}}_{1i_{\mathrm{hit}}} - \frac{\frac{L}{2} - x^{\mathrm{rec}}_{i_{\mathrm{hit}}}}{v_{\mathrm{eff}}} \tag{8.3b}$$

distributions at each reconstructed hit position are plotted respectively, where $TOF^{\mathrm{rec}}_{1i_{\mathrm{hit}}}$ is the reconstructed TOF from the first to the i_{hit}-th hit pixel, $x^{\mathrm{rec}}_{i_{\mathrm{hit}}}$ is the reconstructed x hit position in the pixel for the i_{hit}-th hit, and

$$t_{\mathrm{ave}} = \frac{1}{N_{\mathrm{hit}}} \sum_{i_{\mathrm{hit}}=1}^{N_{\mathrm{hit}}} (t^{\mathrm{rec}}_{i_{\mathrm{hit}}} - t_1 - TOF^{\mathrm{rec}}_{1i_{\mathrm{hit}}}), \tag{8.4}$$

where N_{hit} is the number of hit pixels in a track, and $t^{\mathrm{rec}}_{i_{\mathrm{hit}}}$ is the reconstructed hit time of the i_{hit}-th hit pixel in a track. Similar dependences are seen in 5 cm pixels.

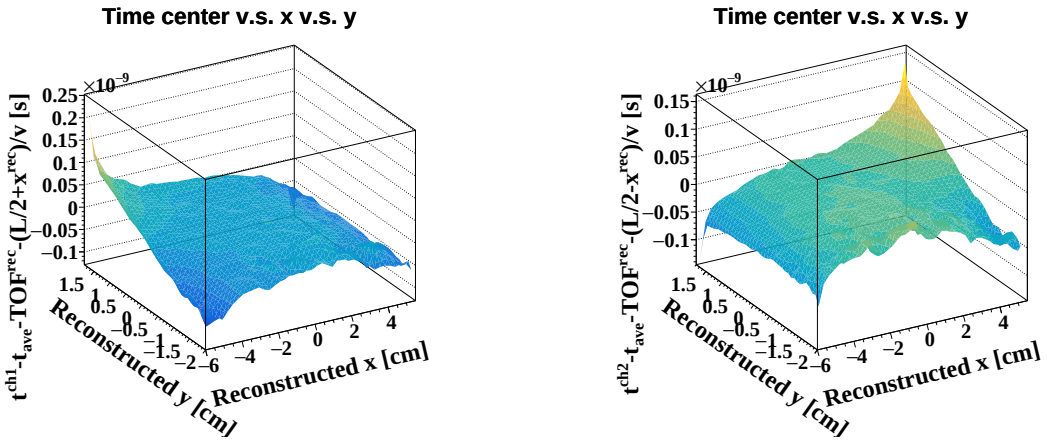

(a) Channel 1 (b) Channel 2

Figure 8.7: Hit position dependence of the time center for 4 cm pixels with intrinsic time offsets after correcting the offsets in x direction.

Due to a finite position resolution, the position dependence obtained using reconstructed values are less prominent than the one obtained using MC values. There also seems to be some position reconstruction bias, which causes the strange behavior at the corners. In any case, the correction can be performed using the observed position dependence.

8.4.3 Correction

Using the position dependence obtained with reconstructed variables, the offset correction was performed. The pTC resolution for events with each number of hit pixels

was obtained using Eq. 6.3, both for the intrinsic and the enhanced time offset case. The results are summarized in Fig. 8.8. The correction using reconstructed variables seems to be capable of recovering the pTC resolution to some extent, though not as effectively as the correction using MC values.

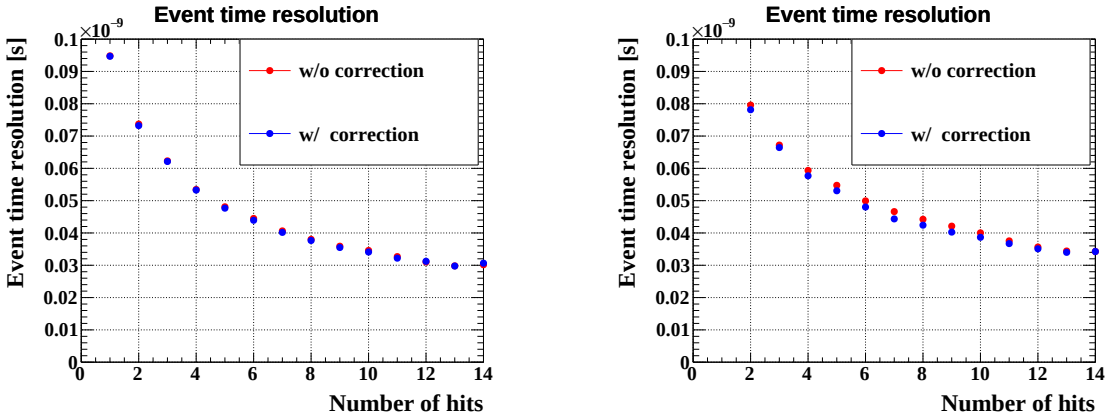

(a) Intrinsic time offset

(b) Enhanced time offset

Figure 8.8: The pTC resolution for events with each number of hit pixels for different datasets. The blue and red markers correspond to with and without the offset correction using reconstructed values respectively.

Using these resolutions, the overall pTC resolution was calculated for each dataset. The obtained resolutions were 38.3 ps and 42.8 ps for the dataset with the intrinsic and the enhanced time offsets respectively. Comparing these values with the ones obtained in Tab. 8.1 using MC hit positions, it is clear that the effect of the correction is limited by the hit position resolution in the CDCH tracking. This is consistent with the fact that the correction works less for events with larger number of hits in Fig. 8.8, as the position resolution is worse for hits at higher hit indices. In any case, the offset correction can recover the pTC resolution to some extent, and the significance of the correction increases with the integrated radiation damage.

8.4.4 Implementation

In the above study, an averaged position dependence of all pixels was used for the correction. However, this strategy is not wise when it comes to applying to the pTC data in the long run. The amount of radiation damage differs from channel to channel, and therefore, the position dependence in each pixel is also expected to differ.

Fig. 8.9 shows the global z dependence of the positron hit rate in pTC pixels. The hit rate clearly differs with z, and so the radiation damage in each channel depends strongly on the z position of the pixel. Therefore it is best to divide the pTC into several sectors according to the expected radiation damage to SiPMs, and the averaged position dependence within each sector should be used for the offset correction. The details of the sector division and other implementations will be left for future study, as it requires a detailed understanding of the radiation damage at each global point.

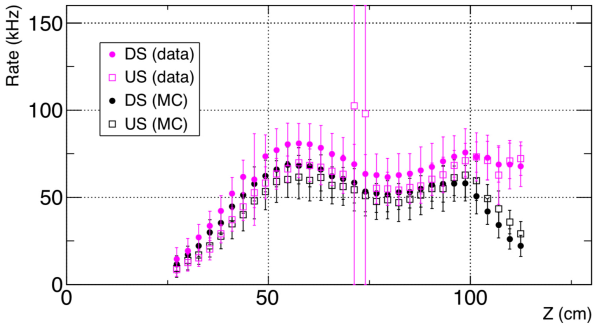

Figure 8.9: Global z dependence of the positron hit rate in pTC pixels using MC simulation and the pER2017 data [60]. Outliers at $z \sim 75\,\text{cm}$ come from noisy DAQ channels.

Chapter 9

Weighted Mean Algorithm

In this chapter, I introduce further ideas to improve the pTC resolution in the offline analysis. The general ideas and methods are discussed, and their effects are evaluated using MC simulation.

9.1 General idea

The positron time measured by the pTC is obtained in three steps. First, the channel times in pixels with hits are obtained in the waveform analysis using the CF method. Second, the time information of the two channels in each pixel are combined to reconstruct the hit time of the pixel. Lastly, the pixel hit times are again combined to reconstruct the overall positron time.

In the original pTC analysis, the time information at the same step is treated equally. For instance, the hit time is obtained as the simple mean of the CF times of the two channels, and the positron time is obtained more or less as the simple mean of all the hit times in a track corrected by each TOF. However, the physical process of the signal induction does not necessarily give equivalent information to each channel, or each hit. In fact, a better time reconstruction should be possible by inflicting appropriate weights to each time information. This is depicted in Fig. 9.1.

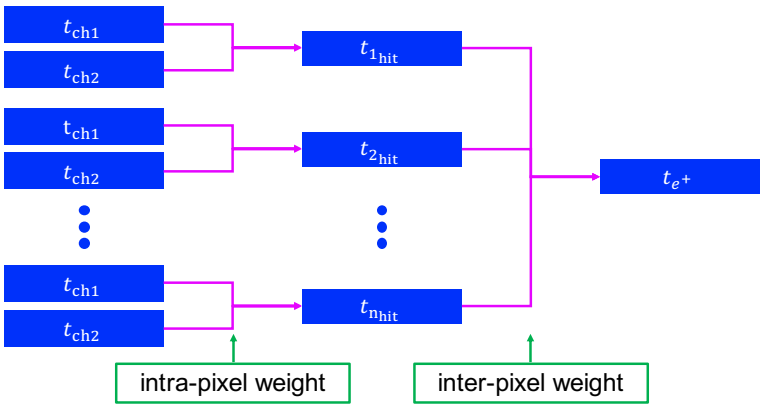

Figure 9.1: A schematic view of the pTC analysis and the weighted mean algorithm.

9.1.1 Using hit position information

One idea is to make use of the hit position information in the hit reconstruction. When the positron hit position in a pixel is off-center in x direction, the arrival time of scintillation photons should deviate less for the channel closer to the hit point than the one farther from the hit point. This causes the closer channel to have a better time resolution than the other. Therefore, the hit time should be reconstructed better by an appropriate weighted mean of the two channel times. The hit position can be obtained with reasonable resolution using the CDCH tracking. This weighted mean algorithm of the two channels is hereon called the hit position intra-pixel weight algorithm.

One thing to note is that any position-dependent time offsets should be eliminated before taking the weighted mean, or else the offset will be enhanced. This should be possible by applying the time offset correction explained in chapter 8 before the intra-pixel weight algorithm.

9.1.2 Using energy deposit information

Another idea is to make use of the energy deposit information in each pixel in the positron time reconstruction. The energy loss process of a charged particle in a matter is probabilistic, which means that the energy deposit of positrons in each pixel fluctuates hit by hit. When the energy deposit in a pixel is large, more scintillation light is produced in the pixel. Therefore, from the photon statistics point of view, the hits with more energy deposits should have better resolutions than the hits with smaller energy deposits. Thus, the positron time should be reconstructed better by an appropriate weighted mean of each hit time. The energy deposit in each pixel can be obtained from the pulse charge in the two channels (c.f. 4.4.1). This weighted mean algorithm of the hits in a track is hereon called the energy deposit inter-pixel weight algorithm.

Like in the case of the hit position intra-pixel weight algorithm, any unnecessary time offsets should be eliminated before taking the weighted mean. We already know from past studies that some time walk exists which depend on the energy deposit (i.e. the pulse height) [60]. Correcting these time walk effects should further enhance the pTC resolution.

9.2 Simulated sample

In order to study the effect of these new algorithms, again, MC simulated data is used. The datasets used for this study are the same as those used in chapter 8. The hit position intra-pixel weight algorithm is tested using the datasets with the intrinsic (60 / 75 ps) and the enhanced (108 / 135 ps) time offsets between SiPMs. On the other hand, the energy deposit inter-pixel algorithm using the energy deposit information is tested using the dataset with no time offsets, in order to neglect any unnecessary effects from the position dependence.

9.3 Intra-pixel weight algorithm

9.3.1 Position dependence

In order to confirm that the assumptions for the intra-pixel weight algorithm are correct, the x hit position dependence of the channel time resolution was checked. Fig. 9.2 shows the result for both 4 cm and 5 cm pixels with intrinsic time offsets. These dependences were obtained essentially in the same way as in 8.4.2 (c.f. Eq. (8.3a) and (8.3b)). As assumed, the time resolution for hits closer to the readout channel is generally better than the hits farther away, and the dependence is more prominent when the time offset correction explained in chapter 8 is applied. A similar position dependence is found in the enhanced time offset case.

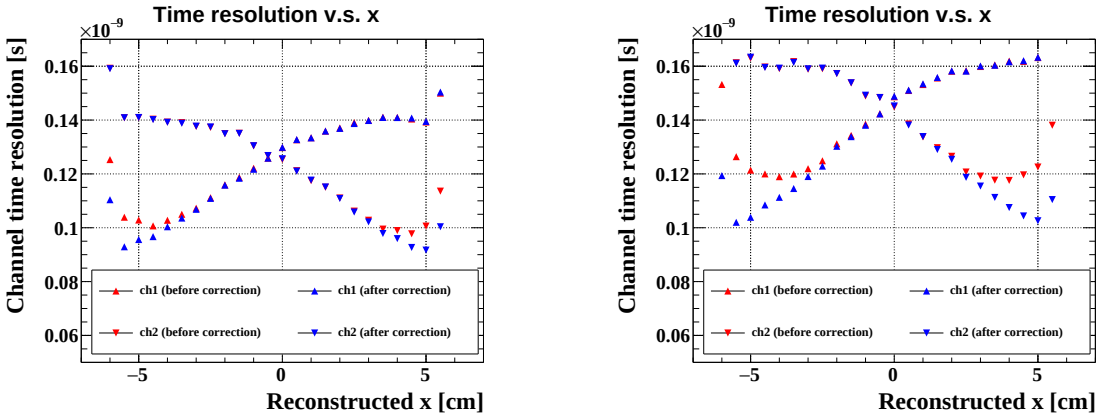

(a) 4 cm pixels (b) 5 cm pixels

Figure 9.2: x hit position dependence of the channel time resolution. The red and blue makers show the position dependence before and after the time offset correction respectively.

9.3.2 Intra-pixel weighting

The channel time resolution at each hit position in Fig. 9.2 can be used as the weights to reconstruct each hit time from the two channel times. In an explicit form, the hit time is reconstructed as follows in the intra-pixel weight algorithm:

$$t_{\mathrm{hit}} = \frac{\frac{t_{\mathrm{ch1}} - t_{\mathrm{offset}}^{\mathrm{ch1}}}{\sigma_{\mathrm{ch1}}^2} + \frac{t_{\mathrm{ch2}} - t_{\mathrm{offset}}^{\mathrm{ch2}}}{\sigma_{\mathrm{ch2}}^2}}{\frac{1}{\sigma_{\mathrm{ch1}}^2} + \frac{1}{\sigma_{\mathrm{ch2}}^2}} \tag{9.1}$$

where t_{ch1} and t_{ch2} are the signal detection times, $t_{\mathrm{offset}}^{\mathrm{ch1}}$ and $t_{\mathrm{offset}}^{\mathrm{ch2}}$ are the position-dependent time offsets, and σ_{ch1} and σ_{ch2} are the relative weights of each channel.

The effect of the intra-pixel weight algorithm is shown in Fig. 9.3. The pixel time resolution clearly improves, especially for edge hits as the effect of weighting becomes prominent. A similar improvement is found in the dataset with the enhanced time offsets. The resolution worsens only at point $x \sim -6$ cm, which is probably due to some bias in the time offset correction arising from a poor position resolution. This will be neglected, however, as this is negligible compared to the overall resolution improvement.

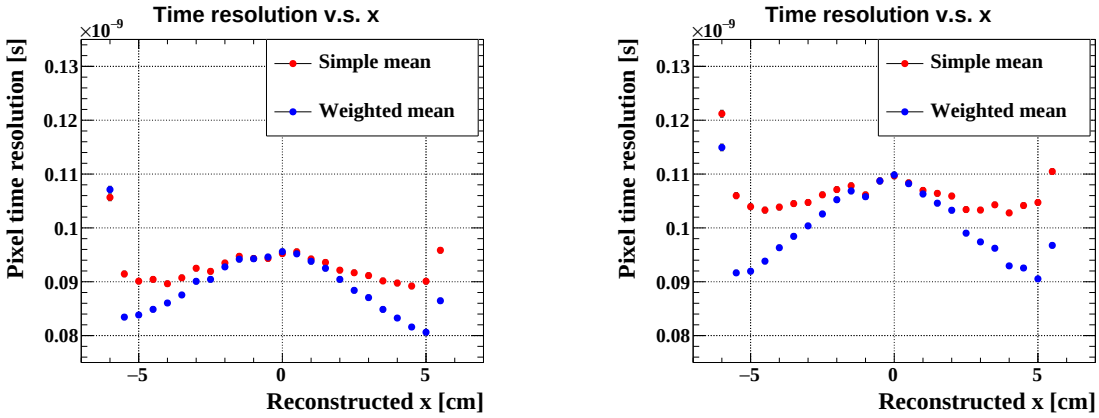

(a) 4 cm pixels (b) 5 cm pixels

Figure 9.3: A comparison of the hit time resolution using the simple-mean and the hit position intra-pixel weight algorithm at each x hit position.

The pTC resolution for each number-of-hit events using the intra-pixel weight algorithm is shown in Fig. 9.4. Each resolution was obtained using Eq. (6.3). The new algorithm is clearly effective.

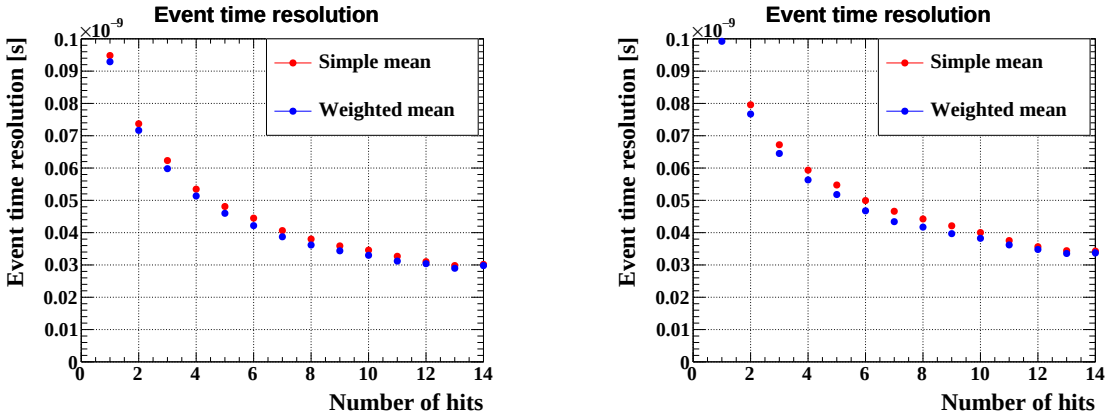

(a) Intrinsic time offset (b) Enhanced time offset

Figure 9.4: The pTC resolution for events with each number of hit pixels for different datasets. The blue and red markers correspond to the result using the simple-mean and the hit position intra-pixel weight algorithm respectively.

The overall pTC resolution using the original and the hit position intra-pixel weight algorithm are summarized in Tab. 9.1. The pTC resolution improves by $\sim 4.4\,\%$ in the dataset with the intrinsic time offsets, and by $\sim 5.1\,\%$ in the dataset with the enhanced time offsets. The algorithm works better for the latter as the position dependence is more prominent.

Table 9.1: The effect of the hit position intra-pixel weight algorithm in each dataset.

Time offset	pTC resolution	
	Simple-mean algorithm	Intra-pixel weight algorithm
Intrinsic time offset	38.7 ps	37.0 ps
Enhanced time offset	44.4 ps	42.1 ps

9.4 Inter-pixel weight algorithm

9.4.1 Energy deposit dependence

In order to confirm that the assumptions for the energy deposit inter-pixel weight algorithm are correct, the energy deposit dependence of the pixel time offset and the resolution were checked, which are shown in Fig. 9.5 and Fig. 9.6 respectively. These were obtained respectively as the Gaussian mean and standard deviation of

$$t^{\mathrm{rec}}_{i_{\mathrm{hit}}} - t_{\mathrm{ave}} - TOF^{\mathrm{rec}}_{1i_{\mathrm{hit}}} \tag{9.2}$$

distribution[1], where $t^{\mathrm{rec}}_{i_{\mathrm{hit}}}$ is the reconstructed hit time of the i_{hit}-th hit pixel in a track, t_{ave} is defined in the same was as in Eq. (6.2), and $TOF^{\mathrm{rec}}_{1i_{\mathrm{hit}}}$ is the TOF from the first to the i_{hit}-th hit pixel.

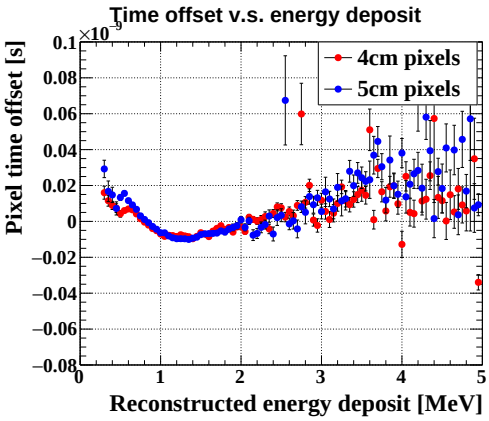

Figure 9.5: Energy deposit dependence of the pixel time offset.

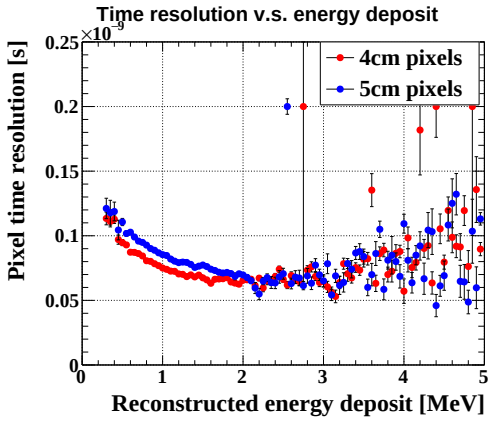

Figure 9.6: Energy deposit dependence of the pixel time resolution.

As already stated, some time walk effect depending on the energy deposit is clearly seen in Fig. 9.5. The energy deposit dependence of the pixel time resolution in Fig. 9.6 is more or less as we assumed; the resolution generally improves with increasing energy deposit. The expected dependence is slightly deformed by the pileup effect of secondary particles at high energy deposit region.

[1] In truth, the distribution was found to contain tail events arising from pile up of secondary particles. Therefore, the distribution is fitted with a double Gaussian, and the narrower distribution is used to obtain the mean and the standard deviation.

9.4.2 Inter-pixel weighting

In any case, the inter-pixel weighting can be performed using the observed energy deposit dependence. The pTC positron time is reconstructed as follows in the inter-pixel weight algorithm:

$$t_{e^+} = \frac{\sum_{i_{\mathrm{hit}}=1}^{N_{\mathrm{hit}}} \frac{t^{\mathrm{rec}}_{i_{\mathrm{hit}}} - TOF^{\mathrm{rec}}_{1i_{\mathrm{hit}}} - t^{i_{\mathrm{hit}}}_{\mathrm{offset}}}{\sigma^2_{i_{\mathrm{hit}}}}}{\sum_{i_{\mathrm{hit}}=1}^{N_{\mathrm{hit}}} \frac{1}{\sigma^2_{i_{\mathrm{hit}}}}} \tag{9.3}$$

where N_{hit} is the number of hit pixels in a track, $t^{\mathrm{hit}}_{i_{\mathrm{hit}}}$ is the reconstructed hit time of the i_{hit}-th hit pixel, $TOF^{\mathrm{rec}}_{1i_{\mathrm{hit}}}$ is the reconstructed TOF from the first to the i_{hit}-th hit pixel, $t^{i_{\mathrm{hit}}}_{\mathrm{offset}}$ is the energy-deposit-dependent time offset of the i_{hit}-th hit pixel, and $\sigma_{i_{\mathrm{hit}}}$ is the relative weight of the i_{hit}-th hit in a track.

Again, the pTC resolution for each number-of-hit events using the energy deposit inter-pixel weight algorithm was obtained using Eq. (6.3) as shown in Fig. 9.7. The algorithm is reasonably effective. The overall pTC resolution obtained from this result improves by $\sim 2.9\,\%$ from 38.1 ps to 37.0 ps using the energy deposit inter-pixel weight algorithm. Note that these values are different from the ones in 9.3 as no time offsets are implemented between SiPMs in the used MC dataset.

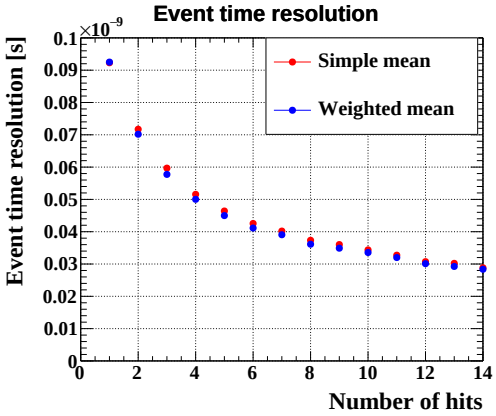

Figure 9.7: The pTC resolution for events with each number of hit pixels. The blue and red markers correspond to the result using the simple-mean and the energy deposit inter-pixel weight algorithm respectively.

9.4.3 Inter-pixel weighting using position information

The original idea of the inter-pixel weight algorithm was to exploit the energy deposit information. However, it can also be performed by using the hit position information. This algorithm is hereon called the hit position inter-pixel weight algorithm.

Fig. 9.8 and Fig. 9.9 show the position dependence of the pixel time offset and the resolution respectively after the intra-pixel weight algorithm for 4 cm pixels with the intrinsic time offsets. These dependences were obtained essentially in the same way as in 9.4.1 (c.f. Eq. (9.2)). Although the hit position dependence of the pixel time offset been removed by the hit position intra-pixel weight algorithm, some position dependence of

the pixel time resolution is found. The resolution seems to be better for edge hits in x direction. This position dependence can be further used when combining the hit times to obtain the overall positron time. Similar dependences were found in 5 cm pixels and in both types of pixels in the dataset with the enhanced time offsets.

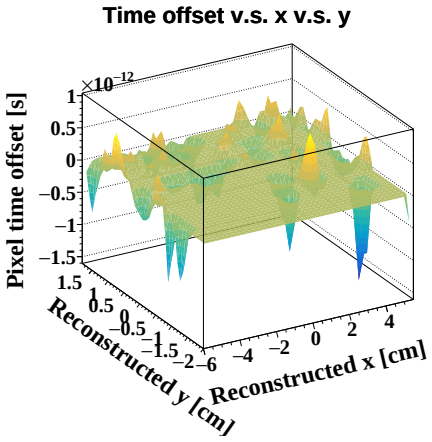

Figure 9.8: Hit position dependence of the pixel time offset after the intra-pixel weight algorithm for 4 cm pixels with intrinsic time offsets.

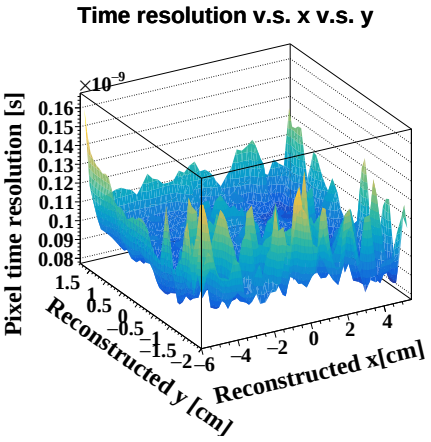

Figure 9.9: Hit position dependence of the pixel time resolution after the intra-pixel weight algorithm for 4 cm pixels with intrinsic time offsets.

The overall pTC resolution after the hit position inter-pixel weighting was obtained in the same way as previously described. The resolution is further enhanced to 36.9 ps in the case of intrinsic time offsets, and to 41.7 ps in the case of enhanced time offsets (c.f. Tab. 9.1). Together with the intra-pixel weight algorithm, the pTC resolution improves by $\sim 4.6\,\%$ and $\sim 5.9\,\%$ in each case.

Chapter 10

Evaluation of pTC Performance

In this last chapter, an evaluation of the pTC performance is performed using the pER2017 data. An estimate of the deterioration of the pTC resolution in the three-year physics run is made, and the final resolution considering the effects of the various methods introduced in this thesis is also given.

10.1 Evaluation method

The methods to evaluate the pTC resolution using MC simulation and the real data are different and are introduced here. The MC evaluation method is the one already adopted in the past chapters.

10.1.1 MC simulation

The pTC resolution using MC simulation can be evaluated rather easily. First, the time resolution for each number-of-hit events is obtained. The time resolution for an N_{hit}-hit event is obtained from the standard deviation of the

$$\begin{aligned} t_{e^+}(N_{\mathrm{hit}}) &= \frac{1}{N_{\mathrm{hit}}} \sum_{i_{\mathrm{hit}}=1}^{N_{\mathrm{hit}}} \left((t_{i_{\mathrm{hit}}}^{\mathrm{rec}} - t_{i_{\mathrm{hit}}}^{\mathrm{MC}}) - (TOF_{1i_{\mathrm{hit}}}^{\mathrm{rec}} - TOF_{1i_{\mathrm{hit}}}^{\mathrm{MC}}) \right) \\ &= \frac{1}{N_{\mathrm{hit}}} \sum_{i_{\mathrm{hit}}}^{N_{\mathrm{hit}}} (t_{i_{\mathrm{hit}}}^{\mathrm{rec}} - TOF_{1i_{\mathrm{hit}}}^{\mathrm{rec}} - t_1^{\mathrm{MC}}) \end{aligned} \tag{10.1}$$

distribution, where $t_{i_{\mathrm{hit}}}^{\mathrm{rec}}$ and $t_{i_{\mathrm{hit}}}^{\mathrm{MC}}$ are the reconstructed and MC-true hit time respectively of the i_{hit}-th hit pixel, and $TOF_{1i_{\mathrm{hit}}}^{\mathrm{rec}}$ and $TOF_{1i_{\mathrm{hit}}}^{\mathrm{MC}}$ are the reconstructed and the MC-true TOF from the first to the i_{hit}-th hit pixel. Thus, a plot as shown in Fig. 10.1 can be obtained.

This is then fitted with

$$\sigma_{t_{e^+}}(N_{\mathrm{hit}}) = \sqrt{\frac{\sigma_1^2}{N_{\mathrm{hit}}} + \sigma_2^2} \tag{10.2}$$

where σ_1 comes from the single-pixel resolution, the inter-pixel calibration precision, the electronics jitter, etc., and the other effects that do not scale with $1/\sqrt{N_{\mathrm{hit}}}$ are incorporated in σ_2 (c.f. Eq. (4.12)). The resolution for each number-of-hit events is calculated

from the fitted curve. The overall pTC resolution is obtained by the weighted sum of these values with the probability of each number of hits. Fig. 10.2 shows the probability distribution of the number of pTC hits using the latest positron analysis algorithm. This distribution is used to evaluate the pTC resolution in this thesis.

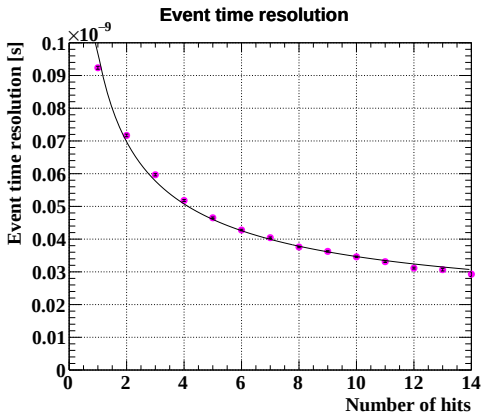

Figure 10.1: The pTC resolution for events with each number of hit pixels using MC data fitted with the function in Eq. (10.2). The MC data without time offsets between SiPMs is used.

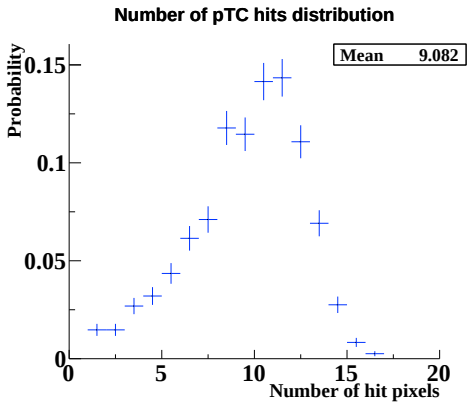

Figure 10.2: Probability distribution of the number of pTC hit pixels after various selection criteria in the positron analysis. This is obtained using MC data.

10.1.2 Real data

Using MC simulation, the pTC resolution was evaluated simply by comparing the reconstructed hit time and TOF with the MC-true ones. However, this method cannot be applied to the real data. In order to evaluate the pTC resolution in the real data, we use a method called the "even-odd analysis".

The idea is to use one pixel hit time as a reference of another pixel hit time, as we have no absolute reference time in the real data. The pTC hits in a track are grouped alternately into "odd" and "even" hits by the order of the pixels traversed by the positron. The pTC resolution for $N_{\rm odd}$ odd hits and $N_{\rm even}$ even hits ($N_{\rm odd} = N_{\rm even}$) can then be obtained as the standard deviation of the

$$\begin{aligned} t_{\rm odd-even}(N_{\rm hit}) &= \frac{1}{2}\big(t_{\rm odd}(N_{\rm odd}) - t_{\rm even}(N_{\rm even})\big) \\ &= \frac{1}{2}\Big(\frac{1}{N_{\rm odd}}\sum_{i_{\rm hit}}^{N_{\rm odd}}(t_{2i_{\rm hit}-1} - TOF_{1(2i_{\rm hit}-1)}) - \frac{1}{N_{\rm even}}\sum_{i_{\rm hit}}^{N_{\rm even}}(t_{2i_{\rm hit}} - TOF_{1(2i_{\rm hit})})\Big) \\ &= \frac{1}{N_{\rm hit}}\Big(\sum_{i_{\rm hit}}^{N_{\rm odd}}(t_{2i_{\rm hit}-1} - TOF_{1(2i_{\rm hit}-1)}) - \sum_{i_{\rm hit}}^{N_{\rm even}}(t_{2i_{\rm hit}} - TOF_{1(2i_{\rm hit})})\Big) \end{aligned} \tag{10.3}$$

distribution where $N_{\rm hit} = N_{\rm odd} + N_{\rm even}$, $t_{i_{\rm hit}}$ is the reconstructed hit time of the $i_{\rm hit}$-th hit pixel, and TOF_{ij} is the TOF from the i-th to the j-th hit pixel. The TOF can be estimated from the CDCH tracking.

This can then be fitted with the function in Eq. (10.2), to obtain the time resolution for each number-of-hit events. To obtain the overall pTC resolution, the same number-of-hit distribution as in Fig. 10.2 is used.

10.2 Evaluation of pTC resolution using data

10.2.1 Data

The pER2017 data was used to evaluate the pTC resolution. In the pER2017, the number of readout channels of 512 was maximum so far, and both the DS and US sectors were read out in turn (c.f. Tab. 4.4). $\sim 1,000,000$ events were taken with each sector, which is more than enough to evaluate the pTC performance. One thing to note is that the CDCH was not installed in the pER2017, and therefore, the CDCH track information is not available. The evaluation is carried out using the pTC track information.

10.2.2 Evaluation

The even-odd analysis was applied to the pER2017 data using the pTC tracking, and the pTC resolution for each number-of-hit events is shown in Fig. 10.3. Fitting the plot with Eq. (10.2) yielded the values of $\sigma_1 \simeq 100.8\,\text{ps}$ and $\sigma_2 = \simeq 0\,\text{ps}$. Using the fitted curve, the overall pTC resolution of $\sim 36.0\,\text{ps}$ was computed.

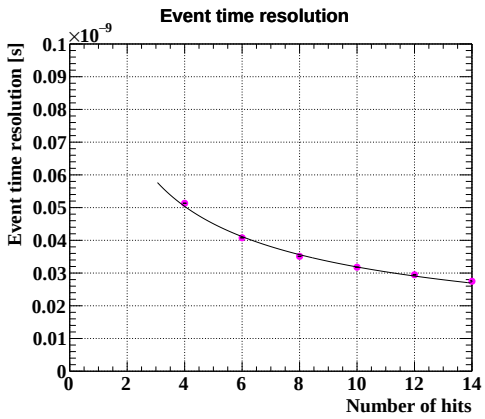

Figure 10.3: The pTC resolution for events with each number of hit pixels using the pER2017 data fitted with the function in Eq. (10.2).

The pTC resolution evaluation using the pER2017 data had already been performed in the past to be $\sim 38.5\,\text{ps}$ [60]. However the pTC tracking algorithm had not been developed then, and therefore, the time resolution was obtained using fixed combinations of pixel hits in the pTC clusters. Using the pTC tracking, we now have less bias in the positron track selection, better estimation of the TOFs, and consequently, a better estimation of the pTC resolution. Note that the positron analysis algorithm has also been updated since the previous work to enhance the positron efficiency.

10.3 Application of new algorithms to data

The new algorithms introduced in chapter 9 were applied to the pER2017 data. The effect of each algorithm when applied to the data is shown below.

10.3.1 Energy deposit inter-pixel weight algorithm

The energy deposit inter-pixel weight algorithm was applied to the pER2017 data. In order to apply the algorithm to the even-odd analysis, the inter-pixel weighting was performed within even hits and odd hits. That is,

$$\begin{cases} t_{\mathrm{odd}}(N_{\mathrm{odd}}) = \dfrac{\sum_{i_{\mathrm{hit}}}^{N_{\mathrm{odd}}} \frac{t_{i_{\mathrm{hit}}} - TOF_{1i_{\mathrm{hit}}} - t_{\mathrm{offset}}^{i_{\mathrm{hit}}}}{\sigma^2_{i_{\mathrm{hit}}}}}{\sum_{i_{\mathrm{hit}}}^{N_{\mathrm{even}}} \frac{1}{\sigma^2_{i_{\mathrm{hit}}}}} & \text{(10.4a)} \\ t_{\mathrm{even}}(N_{\mathrm{even}}) = \dfrac{\sum_{i_{\mathrm{hit}}}^{N_{\mathrm{even}}} \frac{t_{i_{\mathrm{hit}}} - TOF_{1i_{\mathrm{hit}}} - t_{\mathrm{offset}}^{\mathrm{offset}}}{\sigma^2_{i_{\mathrm{hit}}}}}{\sum_{i_{\mathrm{hit}}}^{N_{\mathrm{even}}} \frac{1}{\sigma^2_{i_{\mathrm{hit}}}}} & \text{(10.4b)} \end{cases}$$

in Eq. (10.3) are used.

Fig. 10.4 and Fig. 10.5 show the energy deposit dependence of the pixel time offset and the resolution. These dependences were obtained in the same was as in chapter 9 (c.f. Eq. (9.2)). Although, the energy deposit dependence of the pixel time resolution is similar to the one obtained using MC simulation, the dependence of the time offset is clearly different. One possible cause for this difference is the existence of background Michel positrons, but the exact reason is unknown. The effect of the energy deposit inter-pixel weight algorithm using these values is shown in Fig. 10.6. The overall pTC resolution improves from $\sim 36.0\,\mathrm{ps}$ to $\sim 34.6\,\mathrm{ps}$ with the new algorithm.

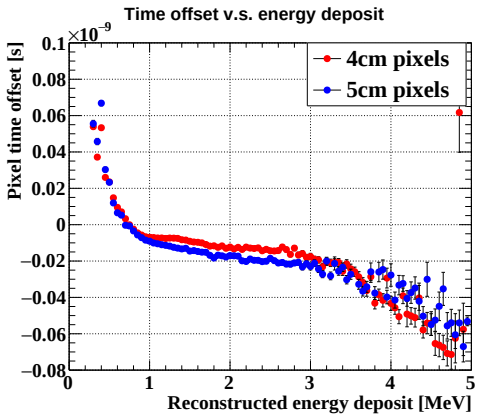

Figure 10.4: Energy deposit dependence of the pixel time offset.

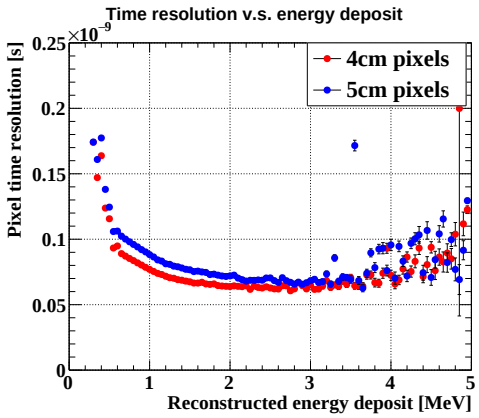

Figure 10.5: Energy deposit dependence of the pixel time resolution.

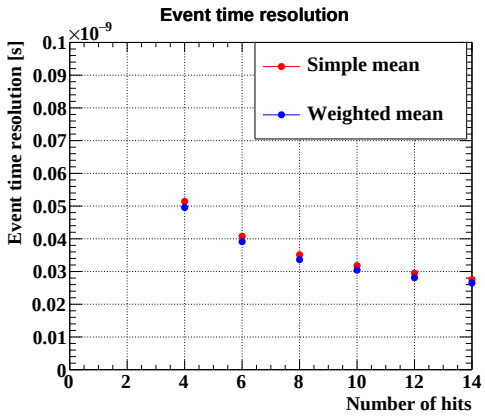

Figure 10.6: The pTC resolution for events with each number of hit pixels. The blue and red markers correspond to the result using the simple-mean and the energy deposit inter-pixel weight algorithm respectively.

10.3.2 Hit position intra-pixel weight algorithm

The hit position intra-pixel weight algorithm together with the time offset correction was applied to data. Fig. 10.7 and Fig. 10.8 show the hit position dependence of the channel time offset and the resolution respectively for 4 cm pixels. These dependences were obtained in the same way is in chapter 9 (c.f. Eq. (8.3a) and Eq. (8.3b)). The dependences are somewhat blurred by the lower position resolution of the pTC tracking, but the time offset in y direction and higher resolutions at hit points closer to the readout channel are seen. Similar dependences are seen in 5 cm pixels.

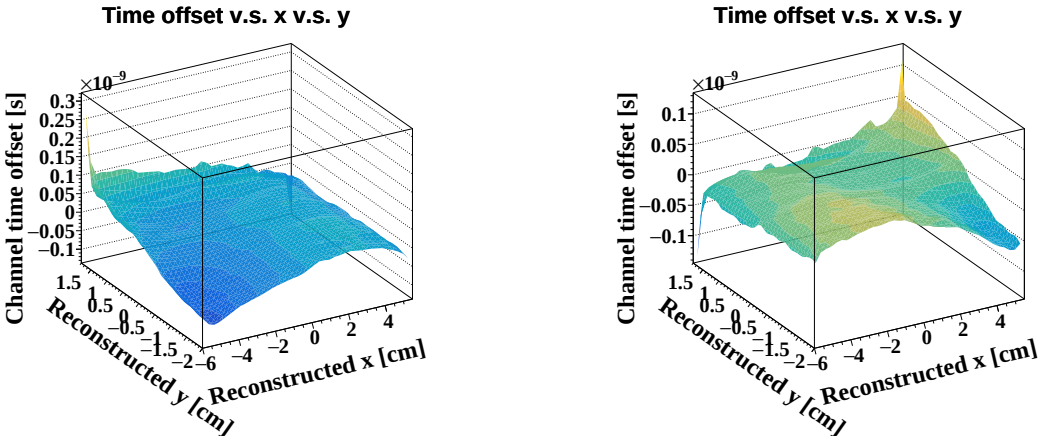

(a) Channel 1 (b) Channel 2

Figure 10.7: Hit position dependence of the channel time offset for 4 cm pixels after correcting the offsets in x direction. The pTC tracking is used to obtain the hit position.

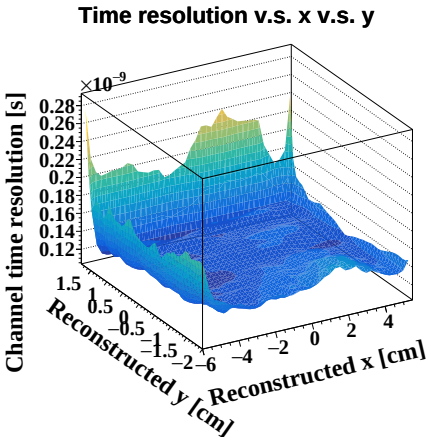

(a) Channel 1

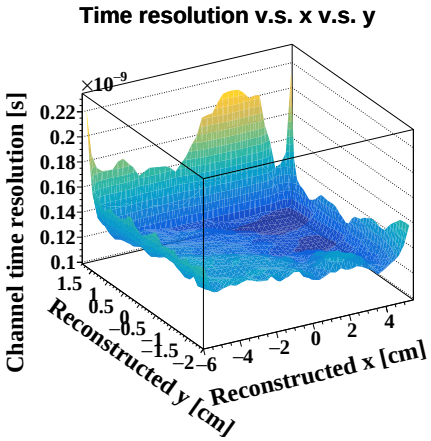

(b) Channel 2

Figure 10.8: Hit position dependence of the channel time resolution for 4 cm pixels. The pTC tracking is used to obtain the hit position.

The intra-pixel weighting was performed in the same way as in chapter 9 (c.f. Eq. (9.1)), and its effect was evaluated. The overall pTC resolution improves from 36.0 ps to 35.6 ps with the new algorithm.

10.3.3 Hit position inter-pixel weight algorithm

The hit position inter-pixel weight algorithm was applied to data in addition to the intra-pixel weight algorithm. Fig. 10.9 and Fig. 10.10 show the hit position dependence of the pixel time offset and the resolution. Again, the position dependence is somewhat blurred by the low position resolution.

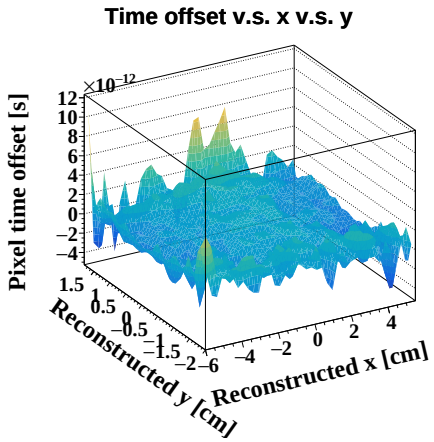

Figure 10.9: Hit position dependence of the pixel time offset.

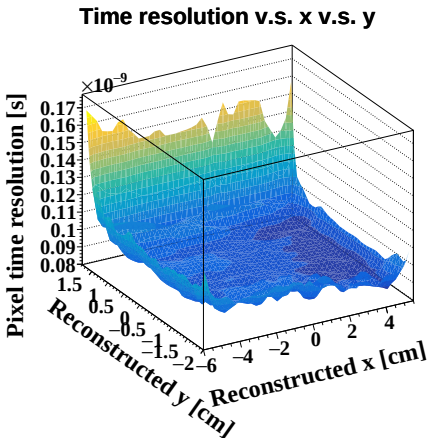

Figure 10.10: Hit position dependence of the pixel time resolution.

The effect of the hit position inter-pixel weight algorithm in addition to the intra-pixel weight algorithm is shown in Fig. 10.11. The overall pTC resolution further improves to 35.4 ps by applying the two algorithms. The application of the algorithm to the even-odd analysis was performed using Eq. (10.4a) and (10.4b).

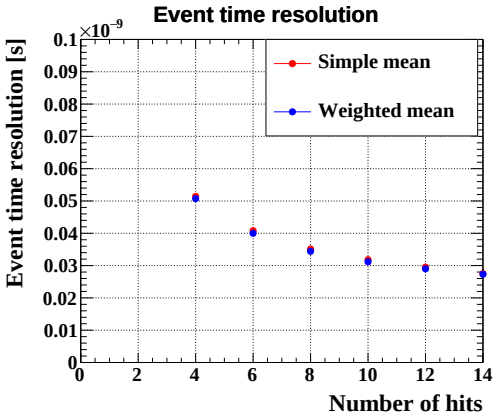

Figure 10.11: The pTC resolution for events with each number of hit pixels. Red and blue markers show the result using the simple mean and both the hit position intra- and inter-pixel weight algorithm respectively.

10.4 pTC resolution evaluation

10.4.1 Problem with the even-odd analysis

The effect of the new algorithms on the pTC resolution when applied to the pER2017 data is summarized in Tab. 10.1. On the other hand, the effect of the algorithms in MC simulation is summarized in Tab. 10.2. Comparing the two results, the energy deposit inter-pixel weight algorithm yields comparable results in the two cases, while a significant difference can be seen in the effect of the new algorithms using the hit position information. This is partly caused by a lower hit position resolution in the pTC tracking compared to the CDCH tracking. However, it is also due to the difference in the evaluation method.

Table 10.1: The effects of the new algorithms on the pTC resolution using the pER2017 data.

Algorithm	pTC resolution	Resolution improvement
Simple mean	$\sim 36.0\,\mathrm{ps}$	
Energy deposit inter-pixel weight	$\sim 34.6\,\mathrm{ps}$	$\sim 4.6\,\%$
Hit position intra-pixel weight	$\sim 35.6\,\mathrm{ps}$	$\sim 1.1\,\%$
Hit position intra- and inter-pixel weight	$\sim 35.4\,\mathrm{ps}$	$\sim 1.8\,\%$

Table 10.2: The effects of the new algorithms on the pTC resolution using MC data with intrinsic time offsets between SiPMs.

Algorithm	pTC resolution	Resolution improvement
Simple mean	$\sim 38.7\,\mathrm{ps}$	
Energy deposit inter-pixel weight	$\sim 37.4\,\mathrm{ps}$	$\sim 3.2\,\%$
Hit position intra-pixel weight	$\sim 37.0\,\mathrm{ps}$	$\sim 4.4\,\%$
Hit position intra- and inter-pixel weight	$\sim 36.9\,\mathrm{ps}$	$\sim 4.6\,\%$

As described in 10.2.2, the evaluation method of the pTC resolution is different for MC simulation and the real data. Taking into consideration the newly-found hit position dependence of the time center, the two methods can potentially yield different resolutions. Although the time fluctuation depending on the hit position is correctly taken into account in the MC evaluation, it is partly canceled out in the even-odd analysis between even hits and odd hits. That is why the new algorithms using the hit position information seem to be less effective when applied to the real data.

This interpretation can be verified by performing the even-odd analysis to MC data. Tab. 10.3 shows a comparison of the pTC resolutions obtained using the two methods for different datasets. The two methods clearly yield different results, meaning that the even-odd analysis cannot compute the true pTC resolution. It is also obvious from the large discrepancy in the dataset with the enhanced time offsets that the even-odd analysis is partly insensitive to the position-dependent time offsets.

Table 10.3: A comparison of the pTC resolution in the two evaluation methods using MC data.

Time offset	MC evaluation	Even-odd analysis
No time offset	$\sim 38.1\,\mathrm{ps}$	$\sim 34.8\,\mathrm{ps}$
Intrinsic time offset	$\sim 38.7\,\mathrm{ps}$	$\sim 35.9\,\mathrm{ps}$
Enhanced time offset	$\sim 44.4\,\mathrm{ps}$	$\sim 39.2\,\mathrm{ps}$

10.4.2 Evaluation of pTC resolution

As the pTC resolution obtained using the even-odd analysis is not true, the resolution value obtained using the even-odd analysis must somehow be converted to what can be assumed to be the correct one. This can be performed using the difference of the inconsistent resolution values obtained using the two methods in MC data. In a similar way, an estimation of the pTC resolution with the availability of the CDCH track can be made by comparing the resolutions using the two tracking methods in MC data.

A comparison of the two evaluation methods and the two tracking methods are shown in Tab. 10.4 using the MC dataset with the intrinsic time offsets. The already-obtained pTC resolution of 36.0 ps corresponds to the bottom right value in Tab. 10.4. Therefore, the true pTC resolution with the availability of the CDCH tracking can be estimated to

be

$$36.0\,\mathrm{ps} \oplus \left((39.0\,\mathrm{ps} \ominus 36.6\,\mathrm{ps}) \times \frac{36.0\,\mathrm{ps}}{36.6\,\mathrm{ps}}\right) \simeq 38.4\,\mathrm{ps} \tag{10.5}$$

assuming that the MC CDCH precisely embodies the real detector. The factor 36.0 ps/36.6 ps is used to scale the MC resolution to fit the data. The required pTC performance of ≤ 46 ps resolution is achieved.

Table 10.4: A comparison of the pTC resolution in the two evaluation methods and the two trackings using MC data with intrinsic time offsets.

	MC evaluation	Even-odd analysis
CDCH tracking	38.7 ps	35.9 ps
pTC tracking	39.6 ps	36.6 ps

10.4.3 Estimation of pTC resolution degradation

From the viewpoint of the long-term operation of the detector, the effects of radiation damage to SiPMs must be taken into account in the pTC resolution evaluation in the long term. One effect is the resolution degradation caused by the worsening of the S/N due to the dark noise increase, which is already known to be suppressed to $\sim 5\,\%$ with 10 °C operation. Another is the resolution degradation caused by the enhanced position dependence of the time center. The effect of the latter can also be estimated by comparing the MC datasets with the intrinsic and the enhanced time offsets.

Tab. 10.5 shows a comparison of the two evaluation methods and the two tracking methods using the MC dataset with the enhanced time offsets. The effect of the enhanced position dependence of the time center can be estimated by comparing Tab. 10.4 and Tab. 10.5. Thus, the pTC resolution at the end of the three-year physics data-taking can be estimated to be

$$\left\{36.0\,\mathrm{ps} \oplus \left((44.4\,\mathrm{ps} \ominus 36.6\,\mathrm{ps}) \times \frac{36.0\,\mathrm{ps}}{36.6\,\mathrm{ps}}\right)\right\} \times 1.05 \simeq 45.9\,\mathrm{ps} \tag{10.6}$$

which is at the limit of the required performance level.

Table 10.5: A comparison of the pTC resolution in the two evaluation methods and the two trackings using MC data with enhanced time offsets.

	MC evaluation	Even-odd analysis
CDCH tracking	~ 44.4 ps	~ 39.2 ps
pTC tracking	~ 45.1 ps	~ 40.0 ps

However, the pTC resolution can be recovered to some extent by applying the optimization schemes and the new algorithms introduced in this thesis. The effect of the bias voltage optimization will be neglected here since its effect has not yet been verified using the detector. The effect of the CF optimization will be assumed to be $\sim 3\,\%$ as verified in 7.4.3. The effect of the new algorithms combined are evaluated below.

Applying all the weighted mean algorithms to the pER2017, the pTC resolution improves from 36.0 ps to 34.3 ps in the even-odd analysis. To estimate the true expected pTC resolution using the CDCH tracking and with the enhanced time offset, this value must be converted taking into account the difference of the tracking, the evaluation and the time offsets using MC data.

Summarized in Tab. 10.6 are the pTC resolutions obtained in different analysis and evaluation conditions using MC data. In the last row, the resolution using the pER2017 data is also shown. From this table, the additional conversion factor is found to be $(40.8\,\text{ps} \ominus 34.7\,\text{ps}) \times 34.3\,\text{ps}/34.7\,\text{ps}$ taking into account the new algorithm.

Table 10.6: A summary of the pTC resolution and the effect of the new algorithms using both MC data and the real data. The new algorithm here refers to the combination of all the weighted mean algorithms.

Data	Time offset	Evaluation	Tracking	pTC resolution	
				Original algorithm	New algorithm
MC	Intrinsic	MC	CDCH	38.7 ps	35.5 ps
MC	Intrinsic	MC	pTC	39.6 ps	37.4 ps
MC	Intrinsic	Even-odd	CDCH	35.9 ps	33.7 ps
MC	Intrinsic	Even-odd	pTC	36.6 ps	34.7 ps
MC	Enhanced	MC	CDCH	44.4 ps	40.8 ps
MC	Enhanced	MC	pTC	45.1 ps	42.6 ps
MC	Enhanced	Even-odd	CDCH	39.2 ps	36.5 ps
MC	Enhanced	Even-odd	pTC	40.0 ps	37.7 ps
Real	Intrinsic	Even-odd	pTC	36.0 ps	34.3 ps

In conclusion, the expected pTC resolution using the CDCH tracking can be estimated as follows:

$$\left\{34.3\,\text{ps} \oplus \left((40.8\,\text{ps} \ominus 34.7\,\text{ps}) \times \frac{34.3\,\text{ps}}{34.7\,\text{ps}}\right)\right\} \times 1.05 \times 0.97 \simeq 41.1\,\text{ps} \tag{10.7}$$

where 1.05 is the factor from the dark noise increase, 0.97 is the factor from the CF optimization, and $(40.8\,\text{ps} \ominus 34.7\,\text{ps}) \times 34.3\,\text{ps}/34.7\,\text{ps}$ is the factor from the enhanced position dependence of the time center, also taking into consideration the bias in the even-odd analysis. The required pTC resolution of $\leq$ 46 ps is expected to be easily achieved also in the long run.

One optimistic view is that the position dependence of the time center vanishes by increasing the CF threshold in the analysis (see Fig. 6.17). This is not effective in the case of the pER2017 data, as a lower CF value is preferred at the waveform analysis level. However, with the accumulation of the radiation damage to SiPMs, a higher CF value is preferred both from the waveform analysis and the position dependence point of view. Therefore, pulling up the CF threshold in the long term, may potentially slow down the degradation of the pTC resolution. This is discussed in more detail in Appendix B. The CF parameter for the above MC studies was fixed to 0.2 in order to compare with the pER2017 analysis.

It should also be noted that the evaluations and estimations made in this chapter are fairly rough incorporating many uncertainties. The pTC resolution obtained above uses the MC simulation to extrapolate the effect of the radiation damage to SiPMs, but some effects that are inherent in the real detector are not taken into account in the MC simulation. For instance, the radiation damage level in all pTC channels are assumed to be exactly the same in the MC setup, which is clearly not the case. For another, the effect of the gain variation among series-connected SiPMs stated in 6.4.2 is neglected in the MC simulation.

Part IV

Summary and Prospect

Chapter 11

Summary and Prospect

11.1 Summary of this thesis

This study was performed for the purpose of

- Developing a stable long-term operation system and
- Improving the analysis method

of the MEG II pTC in order to bring out its maximum performance.

11.1.1 Long-term operation of the pTC

18 new pixels were constructed from the long-term operation point of view, and their basic performance was evaluated. The SiPMs used for the new pixels are slightly different from the old ones, which resulted in relatively high resolutions of the new pixels. For their better performance, some of the old pixels were replaced with the new ones, and they were operated successfully in the pER2019. The replaced old pixels are kept as spares.

The effect of radiation damage to SiPMs, especially a gradient damage to series-connected SiPMs, were studied in detail. In this study, an intrinsic time offset between SiPMs arsing from a finite signal propagation speed was found, which causes hit-position dependent time fluctuations. It was also found that gradient radiation damage to SiPMs can cause an overvoltage variation among series-connected SiPMs, which can potentially enhance the position dependence of the time center. Its effect on the pTC performance was evaluated using MC simulation, and an estimate of $\sim 13\,\%$ degradation of the pTC resolution was made.

In order to make up for the drop in pTC resolution, a scheme was developed to optimize both the bias voltage applied to SiPMs, and the constant fraction parameter used in the waveform analysis. The optimal values of these parameters shift with the increase of the dark noise, and therefore optimizations at each time point is necessary to exploit the maximal pTC performance. The newly-developed scheme optimizes these values solely from the observed S/N, and dedicated DAQs are not required. The effect of the CF optimization was verified to improve the pTC resolution by $\sim 3\,\%$.

11.1.2 Analysis method of the pTC

As another attempt to improve the pTC resolution, a study was conducted to correct the position-dependent time offsets in the offline analysis. By correcting the time offsets using the CDCH track information, the pTC resolution could be recovered to some extent. This approach was found to show higher effects when the time offsets between SiPMs were enhanced by the gradient radiation damage.

Some completely new algorithms to enhance the pTC resolution were also developed. Compared to the original algorithm which treats different channel times or hit times equivalently, the new algorithms inflict appropriate weights on each time information by utilizing the energy deposit and the hit position information of the positron in a pixel. The new algorithms were tested using MC simulation, and was found to recover the pTC resolution by $\sim 8\,\%$.

The new algorithms were applied to the real data, and a moderate improvement in the pTC resolution was found. However, it was newly found that the standard evaluation method of the pTC resolution (the even-odd analysis) does not yield the true resolution, especially when considering the position-dependent time offsets. Therefore, a data-based evaluation method, but also making use of the MC results, was developed, and the pTC resolution was evaluated to be 38.4 ps. Considering the effects from radiation damage to SiPMs, this value was estimated to degrade to 45.9 ps in the three-year physics data taking. However, applying all the attempts to recover the resolution introduced in this thesis, the degradation is expected to be suppressed to 41.1 ps, and the required pTC performance is expected to be achieved also in the long term.

11.2 Future prospects and plans

11.2.1 Positron time resolution

The originally-expected $t_{e^+\gamma}$ resolution at the vertex point is expected to be achieved even with the assumption of a conservative t_γ resolution. However, if the t_γ resolution is better than this value and comparable to the t_{e^+} resolution, then enhancing the pTC resolution still further allows a deeper search of the $\mu \to e\gamma$, as the number of accidental background events increase linearly with $\sigma_{t_{e^+\gamma}}$ (c.f. Eq. (3.8)).

As stated in 8.4.3, the resolution is strictly limited by the hit position resolution in the CDCH tracking, resulting in an inefficient position-dependent time offset correction. A better position resolution should enhance the effect of the time offset correction, as well as the weighted mean algorithms using the hit position information.

We already know that some hit position bias exists in the CDCH positron tracking. Fig. 11.1 and Fig. 11.2 show the overall xy hit position distributions in 4 cm pixels, using MC-true and reconstructed position values respectively. The CDCH tracking clearly has some position bias in y direction, which is likely to suppress the effect of the time offset correction. This position bias has not been investigated in detail yet, but it is assumed to derive from a bias in the y estimation in the pTC tracking, used as initial values for the CDCH track fit. Removing this bias somehow is expected to improve the pTC resolution.

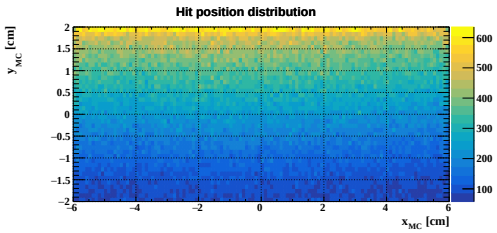

Figure 11.1: Hit position distribution in 4 cm pixels in MC data obtained using MC-true hit positions.

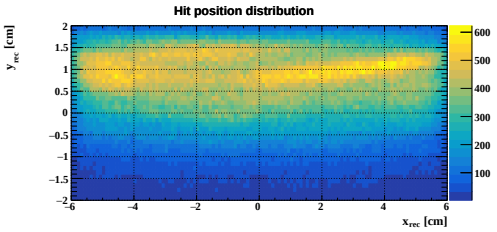

Figure 11.2: Hit position distribution in 4 cm pixels in MC data obtained using reconstructed hit positions with the CDCH tracking.

One idea to improve the position resolution of hit points, is to somehow combine the CDCH and the pTC tracking algorithms. Although the CDCH tracking shows a better performance in general, they have comparable hit position resolutions (see Fig. 8.5 and Fig. 8.6). If these tracking methods have independent sources of bias, then a better position resolution should be obtained by some weighted combination of the two methods. Therefore, understanding the exact characteristics of each tracking method, and developing a way to combine them may be a worthwhile study for the future.

11.2.2 Positron efficiency

This thesis focused on the time resolution of the pTC. However, another important parameter on the positron side which directly affects the MEG II sensitivity is the positron efficiency. The target positron efficiency is 70 %, but the best achieved in MC simulation so far is ~ 63 %. Now that the basic operation and calibration systems for the pTC has been developed and their performance verified, efforts must be put into developing the software tools to achieve the target positron efficiency.

One way to achieve this is to develop an efficient positron matching algorithm between the pTC and the CDCH using MC data. All the pTC analysis algorithms up to tracking (see Fig. 4.8) has already been refined, and their performance has been confirmed using the real data. The next step is to study an effective way to combine the CDCH and the pTC tracks at MC level. By utilizing the pTC track information, a better rejection of the fake hits in the CDCH should be possible.

Another possible way is to improve the CDCH analysis based on the real data. The first beam-data taking using the CDCH was performed in the pER2018, but the CDCH data analysis has not been progressed much yet. Therefore, it is of the upmost importance to check whether the expected performances for the CDCH are achieved in the real data. If not, further investigations to understand the detector performance is essential to progress with the positron analysis.

11.2.3 Evaluation of pTC resolution

One problem confronted in this thesis was that we had no viable data-based evaluation method of the pTC resolution. The even-odd analysis failed to correctly reflect the effect of the position-dependent time fluctuations, and even without the time offsets between SiPMs, the even-odd analysis did not yield the true pTC resolution (c.f. Tab. 10.3).

Therefore, the MC results had to be used in this thesis to convert the obtained resolution to the what seems to be the true resolution. However, this strategy should only work when the MC embodies the real physical processes precisely enough, and is not expected to work in the long run considering the effect from radiation damage to SiPMs.

It is possible to evaluate the final $t_{e^+\gamma}$ resolution using RMD events whose photon and positron are detected by the LXe calorimeter and the positron spectrometer respectively. However, it is, of course, better to have individual evaluation method for each detector to confirm that we understand each detector performance well enough. One possible way to evaluate the pTC resolution is the "double-cluster method". A signal positron can create more the one pTC clusters, and the idea is to use the positron time obtained in one cluster as a reference on the positron time obtained in another cluster. This method should, in principle, also be insensitive to the position-dependent time fluctuations, but having multiple evaluation methods could be useful, for instance, to understand any systematics in each method.

Assuming that a completely data-based evaluation is not possible, the MC results must be used for the evaluation, but to do so, one must confirm that the resolutions obtained using the MC data are truly correct. For instance, as already mentioned, the gain variation among series-connected SiPMs was neglected in this study. These neglected effects must be confirmed to have no significant impact on the pTC resolution and further study is necessary.

Appendix

A Radiation dose calculation

The radiation damage to SiPMs in the case of MEG II pTC is dominated by the bulk damage caused by the collision of $\sim 50\,\mathrm{MeV}$ positrons. This bulk damage increases the bulk leakage current in SiPMs, which is observed as an increase of the dark current. Therefore, it is common to quantify the damage level using the dark current increase.

The bulk damage caused by the irradiation of hadrons is known to be proportional to the displacement damage cross section and is equivalent to the classical calculation of the NIEL [61]. Thus, the NIEL scaling is widely used to standardize damage levels caused by different particles with different energies, and it is common to normalize the damage level with respect to 1 MeV neutrons.

However, we know that the NIEL scaling is violated in the case of electron irradiation [61]. In attempts to standardize the damage level from electron irradiation, modified calculations of the NIEL have been proposed, and an "effective NIEL calculation" using molecular dynamics simulation [62] is known to demonstrate good linearity between the calculated damage and the current-based damage for high-energy electrons [63]. In this thesis, we adopt the classical NIEL calculation for the damage from neutron irradiation, and an effective NIEL calculation for the damage from electron (or positron) irradiation.

For instance, current increase in SiPM arrays was observed in past pERs, which by a simple extrapolation indicates an average current level increase of $\sim 100\,\mu\mathrm{A}$ in the three-year physics run. The SiPMs in the highest hit-rate region are expected to be exposed to $1 \times 10^{11}\,/\mathrm{cm}^2$ $\sim 50\,\mathrm{MeV}$ positrons with the absorbed dose of $\sim 25\,\mathrm{Gy}$ in three years. Using the effective NIEL calculation, the total flux is estimated to be equivalent to $\sim 5 \times 10^9\,/\mathrm{cm}^2$ 1 MeV neutrons. A similar calculation is performed for the electron-irradiated samples for the lab test. For the neutron-irradiated samples, the classical NIEL calculation is used.

B Effect of CF parameter on position dependence of time center

As mentioned in 6.5.3, the position dependence of the time center changes with the CF parameter, and it generally vanishes by pulling up the CF threshold. Fig. B.1 shows the position dependence of the time center in channel 1 for edge hits ($x_{\mathrm{hit}} < -5\,\mathrm{cm}$) in MC data with the intrinsic time offsets, analyzed with different CF parameters in the analysis. The position dependence is slightly lessened in the case of a higher CF threshold. This effects appears more prominently in the case of the enhanced time offsets.

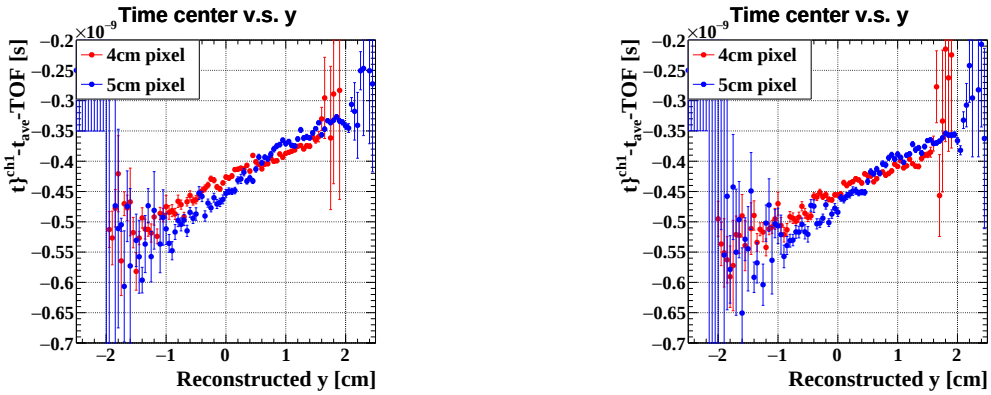

(a) 20 % threshold (b) 50 % threshold

Figure B.1: y hit position dependence of the time center for edge hits ($x_{\mathrm{hit}} < -5\,\mathrm{cm}$) in channel 1 using MC data with the intrinsic time offsets using different CF parameters in the analysis. The pTC tracking is used to obtain the hit position.

This means that a higher CF threshold should yield a better pTC resolution from the viewpoint of the position dependence of the time center. However, as already mentioned in 7.4.1, another optimal CF value exists from the waveform analysis point viewpoint, which depends on the noise level. When the noise level is small, the former optimal value should be larger than the latter, and an overall optimal value should lie somewhere between the two.

Tab. B.1 shows the pTC resolution obtained using different CF parameters in the waveform analysis using MC data with the intrinsic time offsets implemented. As we assumed, the optimal value lies somewhere around $\sim$ 30–40 %, which is relatively higher than the default 20 % preferred in the waveform analysis level.

Table B.1: The pTC resolutions obtained using different CF parameters in the waveform analysis for the MC dataset with the intrinsic time offsets.

Time offset	CF threshold	pTC resolution
Intrinsic	20 %	38.7 ps
	30 %	37.1 ps
	40 %	37.4 ps
	50 %	41.3 ps

In principle, the best pTC resolution should be obtained by optimizing the CF parameter considering both effects, but such an optimization is highly complicated in the long run. Therefore, we decided to optimize the CF parameter in the former stage of the analysis, namely after the hit reconstruction, as was performed in chapter 7, and correct the remaining position dependence of the time center at the end of the offline analysis.

Acknowledgements

First, I would like to mention that many of the studies introduced in this thesis were achieved with the help of the members of the MEG II pTC group. The irradiation of SiPMs in chapter 7 was performed by Masashi Usami and Paolo Cattaneo, and the lab data of the irradiated samples was partly taken by Masashi Usami. The pTC laser data was obtained with the help of Mitsutaka Nakao who developed the laser system in the first place. The greatest contribution comes from Dr. Yusuke Uchiyama, who taught me everything to do the with the pTC, including the pixel assembly procedure in chapter 5, and always gave me insightful advice when I was badly stuck with my work.

Second, I would like to thank my academic supervisor Prof. Wataru Otani and Prof. Toshinori Mori for giving me the opportunity to work with such brilliant colleagues in the MEG II collaboration. It is thanks to them that I could dedicate my two years to the research in physics.

Thirdly and lastly, I would like to thank all the members of the MEG II collaboration for their generous help and work to progress the experiment. In particular, my Japanese colleagues were not only helpful for the fruitful discussions on my study, but also a great comfort for me during the days in Switzerland, namely Dr. Toshiyuki Iwamoto, Dr. Yusuke Uchiyama, Dr. Kei Ieki, Shinji Ogawa, Mitsutaka Nakao, Masashi Usami, Satoru Kobayashi, Rina Onda, Kazuki Toyoda, Atsushi Oya, Kohei Shimada, Taku Yonemoto and Kensuke Yamamoto. I am heartfully grateful to all of them.

Bibliography

[1] M. Tanabashi et al. Review of Particle Physics. *Phys. Rev.*, D98(3):030001, 2018. doi:10.1103/PhysRevD.98.030001.

[2] Stephen P. Martin. A Supersymmetry Primer. *Advanced Series on Directions in High Energy Physics*, page 1–98, Jul 1998. ISSN 1793-1339. doi:10.1142/9789812839657_0001.

[3] E. P. Hincks and B. Pontecorvo. Search for Gamma-Radiation in the 2.2-Microsecond Meson Decay Process. *Phys. Rev.*, 73:257–258, Feb 1948. doi:10.1103/PhysRev.73.257.

[4] Francesco Renga. Experimental searches for muon decays beyond the Standard Model. *Reviews in Physics*, 4:100029, 2019. ISSN 2405-4283. doi:https://doi.org/10.1016/j.revip.2019.100029.

[5] A. M. Baldini et al. Search for the lepton flavour violating decay $\mu^+ \to e^+\gamma$ with the full dataset of the MEG experiment. *Eur. Phys. J.*, C76(8):434, 2016. doi:10.1140/epjc/s10052-016-4271-x.

[6] U. Bellgardt et al. Search for the Decay $\mu^+ \to e^+e^+e^-$. *Nucl. Phys.*, B299:1–6, 1988. doi:10.1016/0550-3213(88)90462-2.

[7] Wilhelm H. Bertl et al. A Search for muon to electron conversion in muonic gold. *Eur. Phys. J.*, C47:337–346, 2006. doi:10.1140/epjc/s2006-02582-x.

[8] William J. Marciano, Toshinori Mori, and J. Michael Roney. Charged Lepton Flavor Violation Experiments. *Annual Review of Nuclear and Particle Science*, 58(1):315–341, 2008. doi:10.1146/annurev.nucl.58.110707.171126.

[9] Ivan Esteban, M. C. Gonzalez-Garcia, Michele Maltoni, Ivan Martinez-Soler, and Thomas Schwetz. Updated fit to three neutrino mixing: exploring the accelerator-reactor complementarity. *Journal of High Energy Physics*, 2017(1), Jan 2017. ISSN 1029-8479. doi:10.1007/jhep01(2017)087.

[10] Yoshitaka Kuno and Yasuhiro Okada. Muon decay and physics beyond the standard model. *Reviews of Modern Physics*, 73(1):151–202, Jan 2001. ISSN 1539-0756. doi:10.1103/revmodphys.73.151.

[11] Stefan Antusch, Ernesto Arganda, Maria Herrero, and Ana Teixeira. Impact of θ 13 on lepton flavour violating processes within SUSY seesaw. *Journal of High*

Energy Physics - J HIGH ENERGY PHYS, 2006:090–090, 11 2006. doi:10.1088/1126-6708/2006/11/090.

[12] Riccardo Barbieri, Lawrence Hall, and Alessandro Strumia. Violations of lepton flavour and CP in supersymmetric unified theories. *Nuclear Physics B*, 445(2-3): 219–251, Jul 1995. ISSN 0550-3213. doi:10.1016/0550-3213(95)00208-a.

[13] Lorenzo Calibbi, Michele Frigerio, Stephane Lavignac, and Andrea Romanino. Flavour violation in supersymmetric SO(10) unification with a type II seesaw mechanism. *JHEP*, 12:057, 2009. doi:10.1088/1126-6708/2009/12/057.

[14] Andrzej Buras, Björn Duling, Thorsten Feldmann, Tillmann Heidsieck, and Christoph Promberger. Lepton Flavour Violation in the Presence of a Fourth Generation of Quarks and Leptons. *Journal of High Energy Physics*, 2010, 06 2010. doi:10.1007/JHEP09(2010)104.

[15] Kaustubh Agashe, Andrew E. Blechman, and Frank Petriello. Probing the Randall-Sundrum geometric origin of flavor with lepton flavor violation. *Physical Review D*, 74(5), Sep 2006. ISSN 1550-2368. doi:10.1103/physrevd.74.053011.

[16] Lorenzo Calibbi and Giovanni Signorelli. Charged Lepton Flavour Violation: An Experimental and Theoretical Introduction. *Riv. Nuovo Cim.*, 41(2):71–174, 2018. doi:10.1393/ncr/i2018-10144-0.

[17] J. Adam, X. Bai, A. M. Baldini, E. Baracchini, C. Bemporad, G. Boca, P. W. Cattaneo, G. Cavoto, F. Cei, C. Cerri, M. Corbo, N. Curalli, A. De Bari, M. De Gerone, L. Del Frate, S. Doke, S. Dussoni, J. Egger, K. Fratini, Y. Fujii, L. Galli, S. Galeotti, G. Gallucci, F. Gatti, B. Golden, M. Grassi, A. Graziosi, D. N. Grigoriev, T. Haruyama, M. Hildebrandt, Y. Hisamatsu, F. Ignatov, T. Iwamoto, D. Kaneko, K. Kasami, P.-R. Kettle, B. I. Khazin, O. Kiselev, A. Korenchenko, N. Kravchuk, G. Lim, A. Maki, S. Mihara, W. Molzon, T. Mori, F. Morsani, D. Mzavia, R. Nard¥ ‘o, H. Natori, D. Nicol¥‘o, H. Nishiguchi, Y. Nishimura, W. Ootani, K. Ozone, M. Panareo, A. Papa, R. Pazzi, G. Piredda, A. Popov, F. Raffaelli, F. Renga, E. Ripiccini, S. Ritt, M. Rossella, R. Sawada, M. Schneebeli, F. Sergiampietri, G. Signorelli, S. Suzuki, F. Tenchini, C. Topchyan, Y. Uchiyama, R. Valle, C. Voena, F. Xiao, S. Yamada, S. Yamamoto, S. Yamashita, Yu. V. Yudin, and D. Zanello. The MEG detector for $\mu^+ \to e^+\gamma$ decay search. *The European Physical Journal C*, 73(4):2365, Apr 2013. ISSN 1434-6052. doi:10.1140/epjc/s10052-013-2365-2.

[18] W Ootani, W Odashima, S Kimura, T Kobayashi, Y Makida, T Mitsuhashi, S Mizumaki, Roger J M Y Ruber, and A Yamamoto. Development of a thin-wall superconducting magnet for the positron spectrometer in the MEG experiment. *IEEE Trans. Appl. Supercond.*, 14(2):568–571. 4 p, 2004. doi:10.1109/TASC.2004.829721.

[19] Malte Hildebrandt. The low-mass drift chamber system of the MEG experiment. *IEEE Nuclear Science Symposium Conference Record*, 10 2011. doi:10.1109/NSSMIC.2011.6154677.

[20] MEG Drift Chamber. URL `https://meg.web.psi.ch/subprojects/dc/dc.html`.

[21] M. De Gerone, S. Dussoni, K. Fratini, F. Gatti, R. Valle, G. Boca, P. W. Cattaneo, R. Nardo, M. Rossella, L. Galli, and et al. Development and Commissioning of the Timing Counter for the MEG Experiment. *IEEE Transactions on Nuclear Science*, 59(2):379–388, Apr 2012. ISSN 1558-1578. doi:10.1109/tns.2012.2187311.

[22] Saint-Gobain Ceramics and Plastics Inc. BC-400, BC-404, BC-408, BC-412, BC-416 Premium Plastic Scintillators, . URL https://www.crystals.saint-gobain.com/sites/imdf.crystals.com/files/documents/bc400-404-408-412-416-data-sheet.pdf.

[23] Photomultiplier Tubes and Related Products.

[24] Hamamatsu Photonics. Si APD S8664 series, . URL https://www.hamamatsu.com/jp/ja/product/type/S8664-55/index.html.

[25] Satoshi Mihara. MEG liquid xenon detector. *Journal of Physics: Conference Series*, 308:012009, jul 2011. doi:10.1088/1742-6596/308/1/012009.

[26] Stefan Ritt, Roberto Dinapoli, and Ueli Hartmann. Application of the DRS chip for fast waveform digitizing. *Nuclear Instruments and Methods in Physics Research Section A: Accelerators, Spectrometers, Detectors and Associated Equipment*, 623(1): 486 – 488, 2010. ISSN 0168-9002. doi:https://doi.org/10.1016/j.nima.2010.03.045. 1st International Conference on Technology and Instrumentation in Particle Physics.

[27] A. M. Baldini, E. Baracchini, C. Bemporad, F. Berg, M. Biasotti, G. Boca, P. W. Cattaneo, G. Cavoto, F. Cei, M. Chiappini, G. Chiarello, C. Chiri, G. Cocciolo, A. Corvaglia, A. de Bari, M. De Gerone, A. D'Onofrio, M. Francesconi, Y. Fujii, L. Galli, F. Gatti, F. Grancagnolo, M. Grassi, D. N. Grigoriev, M. Hildebrandt, Z. Hodge, K. Ieki, F. Ignatov, R. Iwai, T. Iwamoto, D. Kaneko, K. Kasami, P.-R. Kettle, B. I. Khazin, N. Khomutov, A. Korenchenko, N. Kravchuk, T. Libeiro, M. Maki, N. Matsuzawa, S. Mihara, M. Milgie, W. Molzon, Toshinori Mori, F. Morsani, A. Mtchedilishvili, M. Nakao, S. Nakaura, D. Nicol¥'o, H. Nishiguchi, M. Nishimura, S. Ogawa, W. Ootani, M. Panareo, A. Papa, A. Pepino, G. Piredda, A. Popov, F. Raffaelli, F. Renga, E. Ripiccini, S. Ritt, M. Rossella, G. Rutar, R. Sawada, G. Signorelli, M. Simonetta, G. F. Tassielli, Y. Uchiyama, M. Usami, M. Venturini, C. Voena, K. Yoshida, Yu. V. Yudin, and Y. Zhang. The design of the MEG II experiment. *The European Physical Journal C*, 78(5):380, May 2018. ISSN 1434-6052. doi:10.1140/epjc/s10052-018-5845-6.

[28] Davide Reggiani, Mike Seidel, and Christopher Allen. Transverse Phase-space Beam Tomography at PSI and SNS Proton Accelerators. *Conf. Proc.*, C100523:MOPE065, 2010.

[29] Anna Kolano, Andreas Adelmann, Roger Barlow, and Christian Baumgarten. Intensity limits of the PSI Injector II cyclotron. *Nuclear Instruments and Methods in Physics Research Section A: Accelerators, Spectrometers, Detectors and Associated Equipment*, 885, 07 2017. doi:10.1016/j.nima.2017.12.045.

[30] The PSI proton accelerator. URL https://www.psi.ch/en/media/the-psi-proton-accelerator.

[31] A.E. Pifer, T. Bowen, and K.R. Kendall. A high stopping density μ^+ beam. *Nuclear Instruments and Methods*, 135(1):39 – 46, 1976. ISSN 0029-554X. doi:https://doi.org/10.1016/0029-554X(76)90823-5.

[32] G. Chiarello. The full stereo drift chamber for the MEG II experiment. *Journal of Instrumentation*, 12(03):C03062–C03062, mar 2017. doi:10.1088/1748-0221/12/03/c03062.

[33] M. De Gerone, F. Gatti, W. Ootani, Y. Uchiyama, M. Nishimura, S. Shirabe, P. W. Cattaneo, and M. Rossella. Design and test of an extremely high resolution Timing Counterfor the MEG II experiment: preliminary results. *JINST*, 9:C02035, 2014. doi:10.1088/1748-0221/9/02/C02035.

[34] Shinji Ogawa. Liquid xenon calorimeter for MEG II experiment with VUV-sensitive MPPCs. *Nuclear Instruments and Methods in Physics Research Section A: Accelerators, Spectrometers, Detectors and Associated Equipment*, 845:528 – 532, 2017. ISSN 0168-9002. doi:https://doi.org/10.1016/j.nima.2016.06.085. Proceedings of the Vienna Conference on Instrumentation 2016.

[35] K. Ieki, T. Iwamoto, D. Kaneko, S. Kobayashi, N. Matsuzawa, T. Mori, S. Ogawa, R. Onda, W. Ootani, R. Sawada, and et al. Large-area MPPC with enhanced VUV sensitivity for liquid xenon scintillation detector. *Nuclear Instruments and Methods in Physics Research Section A: Accelerators, Spectrometers, Detectors and Associated Equipment*, 925:148–155, May 2019. ISSN 0168-9002. doi:10.1016/j.nima.2019.02.010.

[36] Saint-Gobain Ceramics and Plastics Inc. BC-418, BC-420, BC-422 Premium Plastic Scintillators, . URL https://www.crystals.saint-gobain.com/sites/imdf.crystals.com/files/documents/bc418-420-422-data-sheet.pdf.

[37] Hamamatsu Photonics. MPPC S13360-3050PE, . URL http://www.hamamatsu.com/jp/en/S13360-3050PE.html.

[38] Hamamatsu Photonics. MPPC S12572-025, . URL https://www.hamamatsu.com/resources/pdf/ssd/s12572-025_etc_kapd1043e.pdf.

[39] Atsushi Oya. Development of ultra-low material RPC for further sensitivity improvement of MEG II experiment. Master thesis. 2020.

[40] Keisuke Ogawa. 炭素スパッタを用いた積層型 Fast Timing RPC の開発. Master thesis. 2018.

[41] Marco Francesconi et al. The WaveDAQ integrated Trigger and Data Acquisition System for the MEG II experiment. 2018.

[42] Marco Francesconi. The MEG II Trigger and Data Acquisition System. Master thesis. 2017.

[43] Radiall USA Inc. RF and Microwave cable assemblies, . URL https://www.radiall.com/media/files/RFCableAssemblies%20D1C004XEe.pdf.

[44] Inc. DuPont de Nemours. DUPONT™ TEDLAR® Polyvinyl Fluoride (PVF) Films. URL https://www.dupont.com/content/dam/dupont/products-and-services/membranes-and-films/pvf-films/documents/DEC_Tedlar_GeneralProperties.pdf.

[45] Satoru Uozumi Masashi Yokoyama. Multi Pixel Photon Counter の研究開発. 高エネルギーニュース *26-3*, 216, 2007.

[46] AdvanSiD. NUV SiPMs. URL http://advansid.com/attachment/get/up_53_1432731710.pdf.

[47] Miki Nishimura et al. Pixelated Positron Timing Counter with SiPM-readout Scintillator for MEG II experiment. *PoS*, PhotoDet2015:011, 2016. doi:10.22323/1.252.0011.

[48] Usami Masashi. Development and application of track reconstruction method with MEG II positron timing counter. The Physical Society of Japan (JPS) 2019 Autumn Meeting. URL https://kds.kek.jp/indico/event/32275/contributions/122019/attachments/95016/113174/17pT12-02.pdf.

[49] Mitsutaka Nakao. Commissioning of positron timing counter for MEG II Experiment in 2017: Calibration. The Physical Society of Japan (JPS) 2018 Annual Meeting, . URL https://kds.kek.jp/indico/event/27235/contributions/91614/attachments/73204/86751/25aL401-03.pdf.

[50] Hamamatsu Photonics. Picosecond light pulser PLP-10, . URL http://www.hamamatsu.com.cn/UserFiles/DownFile/Product/SOCS0003E13_PLP-10.pdf.

[51] Mitsutaka Nakao. MEG II positron timing counter -construction, calibration and performance evaluation by using high itensity muon beam, . Master thesis. 2017.

[52] Mitsutaka Nakao. MEG II Timing Counter pre-engineering run 2017: Calibration. Developments of Researches in Lepton Flavor Physics with Muons, 2018. URL https://indico.psi.ch/event/6267/contributions/13227/attachments/11381/14635/nakao0405.pdf.

[53] Chen Xu, Robert Klanner, Erika Garutti, and Wolf-Lukas Hellweg. Influence of X-ray irradiation on the properties of the Hamamatsu silicon photomultiplier S10362-11-050C. *Nuclear Instruments and Methods in Physics Research Section A: Accelerators, Spectrometers, Detectors and Associated Equipment*, 762:149 – 161, 2014. ISSN 0168-9002. doi:https://doi.org/10.1016/j.nima.2014.05.112.

[54] Masashi Usami. Research on radiation tolerance and long-term stable operation of MEG II positron timing counter. Master thesis. 2018.

[55] LabTech. Water Chillers Cooling Solutions. URL https://www.labtechsrl.com/images/labtech/download/waterchillers/Water%20Chiller.pdf.

[56] Maxim Integrated. 1-Wire Digital Thermometer with Sequence Detect and PIO. URL https://datasheets.maximintegrated.com/en/ds/DS28EA00.pdf.

[57] Honeywell International Inc. HIH-4000 Series Humidity Sensors, . URL https://sensing.honeywell.com/honeywell-sensing-hih4000-series-product-sheet-009017-5-en.pdf.

[58] Keithley Instruments Inc. Model 6487 Picoammeter/Voltage Source, . URL https://jp.tek.com/low-level-sensitive-and-specialty-instruments/series-6400-picoammeters-manual/model-6487-picoammeter.

[59] Hamamatsu Photonics. MPPC (multi-pixel photon Chamber), . URL http://www.hamamatsu.com.cn/UserFiles/DownFile/Product/20130812160713344.pdf.

[60] Miki Nishimura. *Positron Timing Measurement to Search for Lepton Flavor Violating Decay in MEG II*. PhD thesis, The University of Tokyo, School of Science, Department of Physics. PhD thesis. 2018.

[61] Jihad Srour, Cheryl Marshall, and Paul Marshall. Review of displacement damage effects in silicon devices. *Nuclear Science, IEEE Transactions on*, 50:653 – 670, 07 2003. doi:10.1109/TNS.2003.813197.

[62] C. Inguimbert, P. Arnolda, T. Nuns, and G. Rolland. "Effective NIEL" in Silicon: Calculation Using Molecular Dynamics Simulation Results. *IEEE Transactions on Nuclear Science*, 57(4):1915–1923, Aug 2010. ISSN 1558-1578. doi:10.1109/TNS.2010.2049581.

[63] Roxana Radu, Ioana Pintilie, Leona Nistor, E. Fretwurst, Gunnar Lindstroem, and Leonid Makarenko. Investigation of point and extended defects in electron irradiated silicon—Dependence on the particle energy. *Journal of Applied Physics*, 117:164503, 04 2015. doi:10.1063/1.4918924.